Nanoscale Characterization of Biopolymers using Atomic Force Microscopy and Plasmon-Enhanced Raman Spectroscopy

Dissertation

zur Erlangung des akademischen Grades

Doktor rerum naturalium

(Dr. rer. nat.)

vorgelegt dem Rat der Chemisch-Geowissenschaftlichen Fakultät der

Friedrich-Schiller-Universität Jena

von

Erwan Yudiar Darussalam, M.Sc

geboren am 01.10.1992 in Cianjur, Indonesia

1st Supervisor
Prof. Dr. Volker Deckert
Friedrich-Schiller-Universität Jena
Leibniz Institute for Photonic Technologies (IPHT)

2nd Supervisor
Prof. Dr. Ralf. Ehricht
Friedrich-Schiller-Universität Jena
Leibniz Institute for Photonic Technologies (IPHT)

Tag der Verteidigung: 23rd August 2023

Contents

List of Figures…………………………………………………………………... 6

List of Tables………………………………………………………………… 8

Motivation………………………………………………………………….... 9

Chapter 1 Introduction ………………………………………………………. 11
- 1.1 Proteins and peptides………………………………………………… 12
- 1.2 Viruses……………………………………………………………….. 15
- 1.3 Scanning Probe Microscopy………………………………………… 17
- 1.4 Raman Spectroscopy……………………………………………….... 19
- 1.5 Surface-Enhanced Raman Spectroscopy…………………………….. 21
- 1.6 Tip-Enhanced Raman Spectroscopy……………………………...... 22

Chapter 2 Results

Identification of Single Amino Acids towards Direct Protein Sequencing with Tip-Enhanced Raman Spectroscopy…………………………………………… 27
- 2.1 Introduction………………………………………………………….. 28
- 2.2 Experiments………………………………………………………….. 30
  - 2.2.1 Sample Preparation…………………………………………….. 30
  - 2.2.2 AFM Topography Measurements……………………………… 30
  - 2.2.3 TERS Measurements………………………………………….... 31
- 2.3 Results and Discussion………………………………………………. 32
  - 2.3.1 AFM topography of samples incubated at 37°C…..……………. 32
  - 2.3.2 AFM topography of samples incubated at 70°C...………………. 34
  - 2.3.3 1st TERS experiment with 5nm step size………………………. 37
  - 2.3.4 High-resolution TERS experiments with 0.5 nm step size……… 40
- 2.4 Chapter 2 Conclusion……………………………………………….... 45

Chapter 3 Results

The Disintegration of Insulin Amyloid Fibrils Monitored using Atomic Force Microscopy and Surface-Enhanced Raman Spectroscopy……………………... 46
- 3.1 Introduction………………………………………………………….. 47
- 3.2 Experiments…………………………………………………………. 50
  - 3.2.1 Sample Preparation…………………………………………….. 50
  - 3.2.2 AFM Topography Measurements……………………………… 50
  - 3.2.3 SERS Measurements…………………………………………… 51
- 3.3 Results and Discussion……………………………………………… 51
  - 3.3.1 AFM Topography Measurements in the Dried State………….. 51
  - 3.3.2 AFM Topography Measurements in a Liquid Environment…... 54
  - 3.3.3 SERS Measurements (pH 2.5, 4, 7) …………………………... 56
- 3.4 Chapter 3 Conclusion……………………………………………….. 60

Chapter 4 Results

SARS-CoV-2 Characterization by Correlative Atomic Force - Fluorescence Microscopy and TERS…………………………………………………….…. 61

4.1 Introduction…………………………………………………….. 62

4.2 Experiments……………………………………………………… 67

4.2.1 Sample Preparation……………………………………….. 67

a. Virus Propagation and Characterization ……………………... 67

b. SARS-CoV-2 Inactivation……………………………………. 67

4.2.2 AFM Topography Measurements……………………………… 68

4.2.3 AFM-Fluorescence Correlation Measurements………………... 68

4.2.4 TERS Measurements……………………………………... 69

4.3 Results and Discussion…………………………………………… 70

4.3.1 AFM Topography Measurements……………………………… 70

4.3.2 AFM-Fluorescence Microscopy Correlation Study……………. 73

4.3.3 TERS Measurements of SARS-CoV-2………………………… 78

4.4 Chapter 4 Conclusion……………………………………………….. 86

Chapter 5 General Thesis Conclusion……………………………………… 87

Zusammenfassung…………………………………………………………. 89

References……………………………………………………………….. 91

Acknowledgements………………………………………………………… 104

Selbständigkeitserklärung…………………………………………………… 105

List of Figures

Chapter 1 Introduction

1. Protein level structure………………………………………………… 13
2. Structure of amino acid glycine (Gly) ………………………………... 14
3. Twenty-one natural amino acids……………………………………… 14
4. Scheme of virus structures……………………………………………. 15
5. Sketched AFM setup………………………………………………….. 18
6. Energy diagram of Raman spectroscopy……………………………… 20
7. Schematic diagram of localized surface plasmon resonance (LSPR)…… 21
8. Schematic diagram of the AFM-TERS setup…………………………. 25

Chapter 2 Results

Identification of Single Amino Acids towards Direct Protein Sequencing with Tip-Enhanced Raman Spectroscopy

1. Sample preparation scheme…………………………………………… 30
2. TERS setup for characterizing the KFAK peptide-4Bpy adduct……….. 31
3. TERS measurement scheme…………………………………………... 32
4. AFM topography of the KFAK peptide-4Bpy adduct at 37°C………….. 33
5. AFM topography of pure 4Bpy and KFAK-peptide at 37°C……………. 34
6. AFM topography of the KFAK peptide-4Bpy adduct at 70°C…….......... 35
7. AFM topography of the pure KFAK-peptide at 70°C…………………... 36
8. AFM topography of pure 4Bpy at 70°C……………………………… 36
9. Selected TERS and standard Raman spectra of a KFAK peptide-4Bpy adduct………………………………………………………………. 39
10. Selected TERS spectra of KFAK peptide-4BY adduct at successive measurement points separated by 0.5 nm……………………………… 41

Chapter 3 Results

The Disintegration of Insulin Amyloid Fibrils Monitored using Atomic Force Microscopy and Surface-Enhanced Raman Spectroscopy

1. Mechanism of amyloid fibrillation………….………………………… 47
2. Sample preparation scheme…………………………………………… 50
3. AFM topography of dried insulin aggregates…………………………. 52
4. AFM topography of dried insulin aggregates on 3 different areas……… 53
5. In situ monitoring of the disintegration of a mature insulin fibril at pH 4 with an AFM in liquid. ……………………………………………….. 54
6. AFM topography of the disintegration of a mature insulin fibril in a liquid environment at pH 4. …………………………………………….. 55
7. AFM tip convolution scheme…………………………………………. 56
8. Standard Raman spectrum of insulin fibrils grown in pH 2.5 and SERS spectra of dried insulin aggregates at pH 2.5, 4, and 7………………….. 57
9. Molecular vibration mode of amide I…………………………………..... 58

Chapter 4 Results

SARS-CoV-2 Characterization by Correlative Atomic Force-Fluorescence Microscopy and TERS

1. COVID-19 confirmed and death cases data statistics………………….. 62
2. Schematic of SARS-CoV-2 structure…………………………………… 63
3. Electron microscope image of SARS-CoV-2…………………………… 65
4. Scheme of the AFM-fluorescence correlation measurements………….. 69
5. Illustration of the movement of the tip along the TERS grid…….......... 70
6. AFM topography of SARS-CoV-2 from differently inactivated samples 71
7. AFM topography of pure PFA………………………………………….. 72
8. Image of a special glass substrate with grid numbers and letters……….. 74
9. Illustration of AFM-fluorescence correlation measurements…………… 74
10. AFM-fluorescence microscopy correlation experiments (PFA)……….. 75
11. AFM-fluorescence microscopy correlation experiments (UV-C)………. 75
12. AFM-fluorescence microscopy correlation experiments (PFA-UVC)…. 76
13. False negative AFM-fluorescence microscopy correlation experiments.. 77
14. False positive AFM-fluorescence microscopy correlation experiments... 77
15. TERS spectra acquired on SARS-CoV-2 (1)…………………………… 78
16. Schematic representation of the SARS-CoV-2 spike protein………….. 80
17. TERS spectra acquired on SARS-CoV-2 (2)…………………………… 82

List of Tables

Chapter 2 Results

Identification of Single Amino Acids towards Direct Protein Sequencing with Tip-Enhanced Raman Spectroscopy

Table 1 Detected bands in the TERS spectra of the KFAK peptide-4BY adduct and tentative assignment……………………………….... 44

Chapter 4 Results

SARS-CoV-2 Characterization by Correlative Atomic Force Microscopy-Fluorescence and TERS

Table 1 Wavenumber, vibrational origin, type of biopolymer, and literature references from all TERS results……………………………….. 85

Motivation

Proteins are large, complex macromolecules that are found in every cell and cell component and play a variety of roles that are essential to the functioning of the body. They can be found in a wide range of sizes and shapes, and even a single cell can contain thousands of distinct protein variants. They consist of long chains of amino acids, which are organic compounds made up of carbon, hydrogen, oxygen, nitrogen, and sometimes sulfur [1]. Furthermore, there are four levels of protein structures which can be classified as follows: primary, secondary, tertiary, and quaternary structure. Understanding the structure of proteins is often necessary to understand their biological processes. With this information, scientists can draw conclusions about the effects of structural changes on protein function for example [2].

Several analytical techniques are commonly used to characterize the different structures of proteins. To examine the three-dimensional structure of a protein, for example, X-ray crystallography, nuclear magnetic resonance (NMR), and Electron Microscopy (EM) are established techniques [3]. Nevertheless, these methods have their own drawbacks. For instance, one of the main limitations of X-ray crystallography for protein structure analysis is that it requires the protein to be crystallized, which can be a challenging and time-consuming process and not all proteins are able to form crystals. In addition, it also needs a large amount of material to optimize the crystallization condition. Furthermore, X-ray crystallography is only able to provide information about the structure of the protein in the crystalline state, which may not always be the same as its structure in the solution [4, 5]. Although NMR overcomes the limitation of X-ray crystallography by permitting direct observation of folded or unfolded protein structure, dynamics, and protein-protein interactions under physiological conditions, which does not require crystallization, nonetheless, it has its own limitations [6]. Up to the present, one of the primary limitations of NMR for protein structure analysis is that it could only provide information about smaller proteins, which are less than 30 kDa. This is because the signal-to-noise ratio in NMR spectra decreases as the size of the protein increases, making it difficult to obtain structural information with high resolution for larger proteins [7].

Electron Microscopy, on the other hand, is used to compensate for the limitations of X-ray and NMR techniques by providing super high-resolution images of the three-dimensional structure of proteins without requiring a sample crystallization [4]. However, one limitation is that the samples must be located in a vacuum environment, which can cause them to behave differently than they would be in their natural state. Consequently, the specimen must be imaged in a solid state and this can make it difficult to study materials, such as biological samples, that are sensitive to vacuum conditions [8].

AFM is another imaging technique that can be used to characterize the nanoscale surface properties of materials. AFM's ability to produce images up to atomic-level resolution is one of its most significant advantages. Another benefit of AFM is its adaptability. It can be used to examine a wide variety of materials, such as metals, semiconductors, polymers, and biological samples, and it can be used in a variety of environments, including air, liquid, and vacuum [9, 10]. To obtain detailed chemical information (molecular structure) from the sample, however, another analytical technique, such as vibrational spectroscopy, needs to be incorporated (e.g., Raman spectroscopy).

Raman spectroscopy is a powerful analytical technique that identifies and studies the vibrational modes of molecules. The technique is based on the Raman effect, which was first observed by Indian physicist Sir Chandrasekhara Venkata Raman in 1928 [11]. It can provide insights into the molecular structure and properties of the studied material. It was developed to extract chemical information from a sample without the need for labeling or extensive sample preparation (e.g., fluorescence microscopy) [12]. Nonetheless, this Raman effect is a rare event, and proteins in the cell are present at extremely low concentrations, which contributes to the weak Raman signal. Therefore, in order to improve the method's sensitivity and resolution, scientists employ an approach based on the surface plasmon resonance effect, which increases the local electric field of the incident light (on the molecules near the surface of the metal nanoparticles) [13]. When combined with the AFM technique, both high-resolution images and detailed chemical information can be retrieved, making this technique a highly effective method for characterizing protein structures.

In this thesis, three levels of protein structures were characterized using AFM and plasmon-enhanced Raman spectroscopy and the results are presented in three following chapters:

1. Characterization of the primary structure of proteins by identifying single amino acids as a step toward direct protein sequencing with TERS
2. Characterization of the secondary structure of proteins by studying the disintegration of insulin amyloid fibrils monitored by AFM and SERS
3. Characterization of the protein structure in a complex environment by investigating SARS-CoV-2 with AFM-fluorescence microscopy and TERS

CHAPTER 1
INTRODUCTION

1.1 Proteins and Peptides

Proteins and peptides are the most prevalent biological molecules, and they are present in every cell and cell component and play important roles in the structure and function of living cells. Nevertheless, proteins and peptides are not the same, and there are a number of essential distinctions that can be drawn between the two. Proteins are complex three-dimensional biomolecules composed of long chains of amino acids (hundreds to thousands) connected through covalent peptide bonds [14, 15]. They are involved in virtually all cellular processes and perform an almost infinite variety of functions. Proteins contribute, for example: (a) as intracellular and extracellular structural components (cell membrane); (b) as agents of molecular assembly; (c) ion channels and pumps; (d) biological catalysts; (e); mediators of contractility and motility (f) molecular transporters; (g) mediators of immunity; and (h) intracellular and intercellular signaling network components [16]. Proteins can also play crucial roles in the viral infection of the host cell, (e.g., SARS-CoV-2 infection via S glycoprotein) [17]. Peptides, on the other hand, are much smaller molecules that are constructed from a combination of two or more amino acids that are also connected via peptide bonds. In comparison to proteins, they typically have a simpler conformation and a shorter length, and they are frequently responsible for performing particular biological functions. Insulin, for instance, is a peptide that consists of 51 amino acids and is produced in order to keep blood glucose at normal levels [18, 19].

Figure 1 shows the four different levels of protein structures, namely primary, secondary, tertiary, and quaternary structures. The quaternary structure of a protein describes how multiple polypeptide chains assemble to form a single functional molecule. This structure is made up of different subunits, and each of those subunits has its own primary structure as well as secondary and tertiary structures. Hydrogen bonds and van der Waals forces, which act between nonpolar side chains, are responsible for keeping the subunits together [2]. The tertiary structure of a protein on the other hand is the arrangement of the polypeptide chain in three dimensions. It is also stabilized by hydrophilic hydrogen and ionic bond interactions on the outside, and hydrophobic interactions between nonpolar amino acid side chains on the inside [1]. Additionally, covalent disulfide bonds also contribute to the structural stability of proteins [20].

Furthermore, the secondary structure is the arrangement of adjacent amino acid residues in a polypeptide chain in a regular, repeating pattern (i.e., in α-helix and β-sheets structures) and in more flexible, disordered conformation (i.e., random coil structure). Hydrogen bonds are formed between amide hydrogen atoms and carbonyl oxygen atoms in the peptide backbone and stabilize the structure [21]. In general, the sequence of a protein plays a role in determining which amino acid residues will form α-helix and which will form β-sheets, to the extent that secondary structure prediction can be performed with a reasonable degree of accuracy [22]. Lastly, the primary structure refers to the protein sequence, which is the order of the amino acids in a protein.

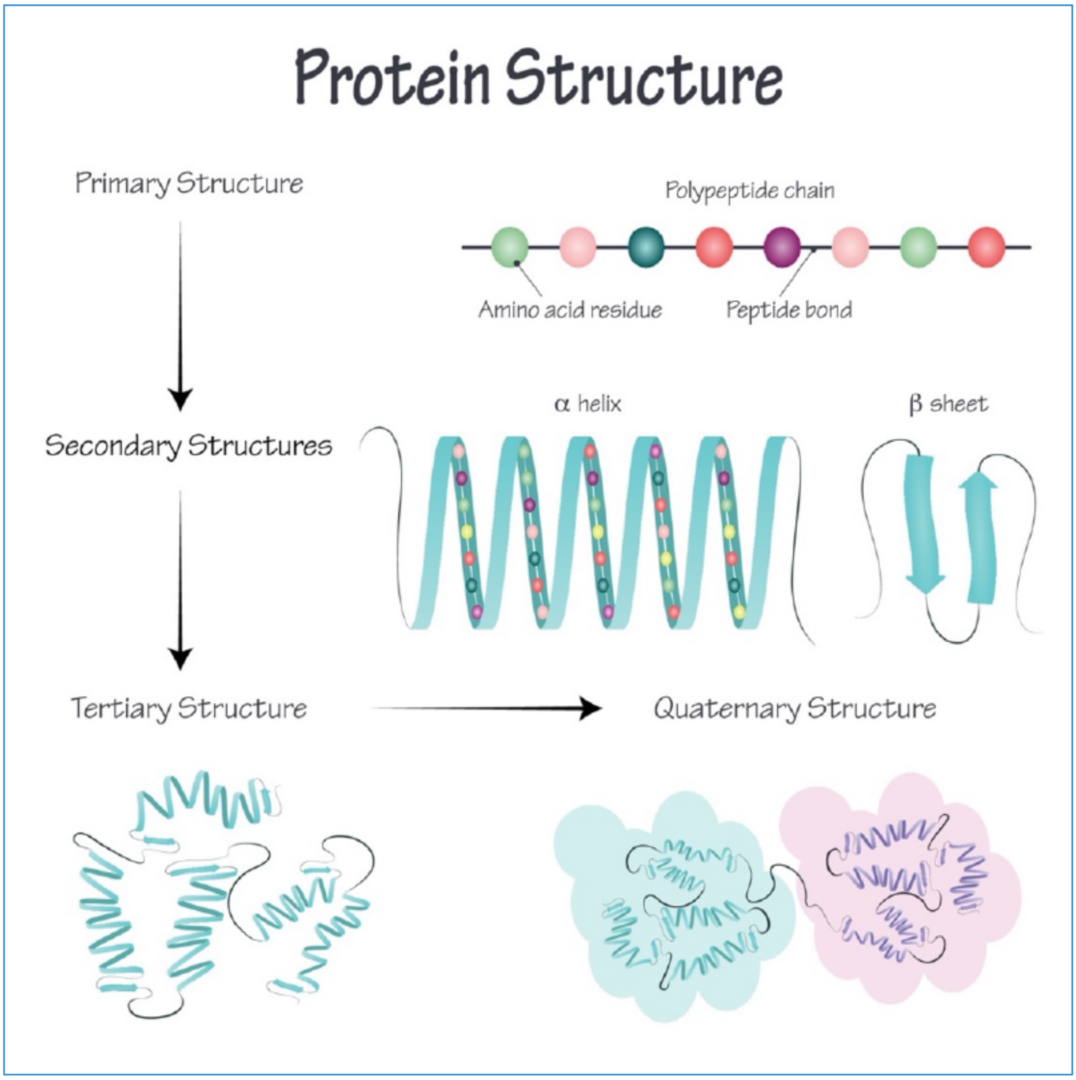
Protein Structure
Primary Structure
Polypeptide chain
Amino acid residue
Peptide bond
Secondary Structures
α helix
β sheet
Tertiary Structure
Quaternary Structure

Figure 1. Schematic illustration of the various protein level structures, adapted with permission from J Ashes, https://www.vecteezy.com/vector-art/7818644-vector-illustration-of-protein-structure.

Proteins are composed of a combination of twenty different monomers, the amino acids [14], which contain an amino group (-NH_2), a carboxyl group (-COOH), a hydrogen atom (-H), and a side chain (-R "residue") [23]. Each amino acid has a distinct side chain, which allows them to be classified into 20 different types. For example, Glycine (Gly) is the simplest amino acid, where R (side chain) is a hydrogen atom (see Figure 2). Figure 3 illustrates the remaining twenty amino acids and one additional amino acid that is Selenocysteine which is still a matter of debate.

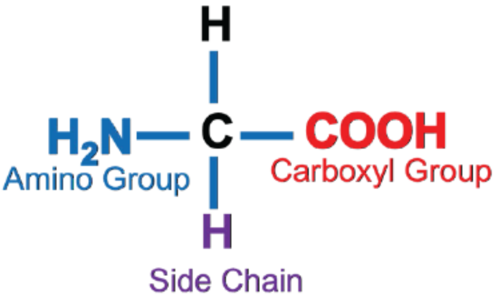
H
H₂N
C
COOH
Amino Group
Carboxyl Group
H
Side Chain

Figure 2. Structure of the amino acid glycine (Gly)

The primary structure of the peptide can be formed through the translation of the genetic message carried by mRNA in the ribosome, a process known as protein synthesis. In addition to their role as substrates in the process of protein synthesis, amino acids are also participants in a wide variety of metabolic pathways [16]. By knowing the sequence, it is possible, for instance, to predict the protein's function, as well as to identify and categorize the protein (e.g., antibodies, contractile proteins, enzymes, hormonal proteins, structural proteins, storage proteins, and transport proteins) [24].

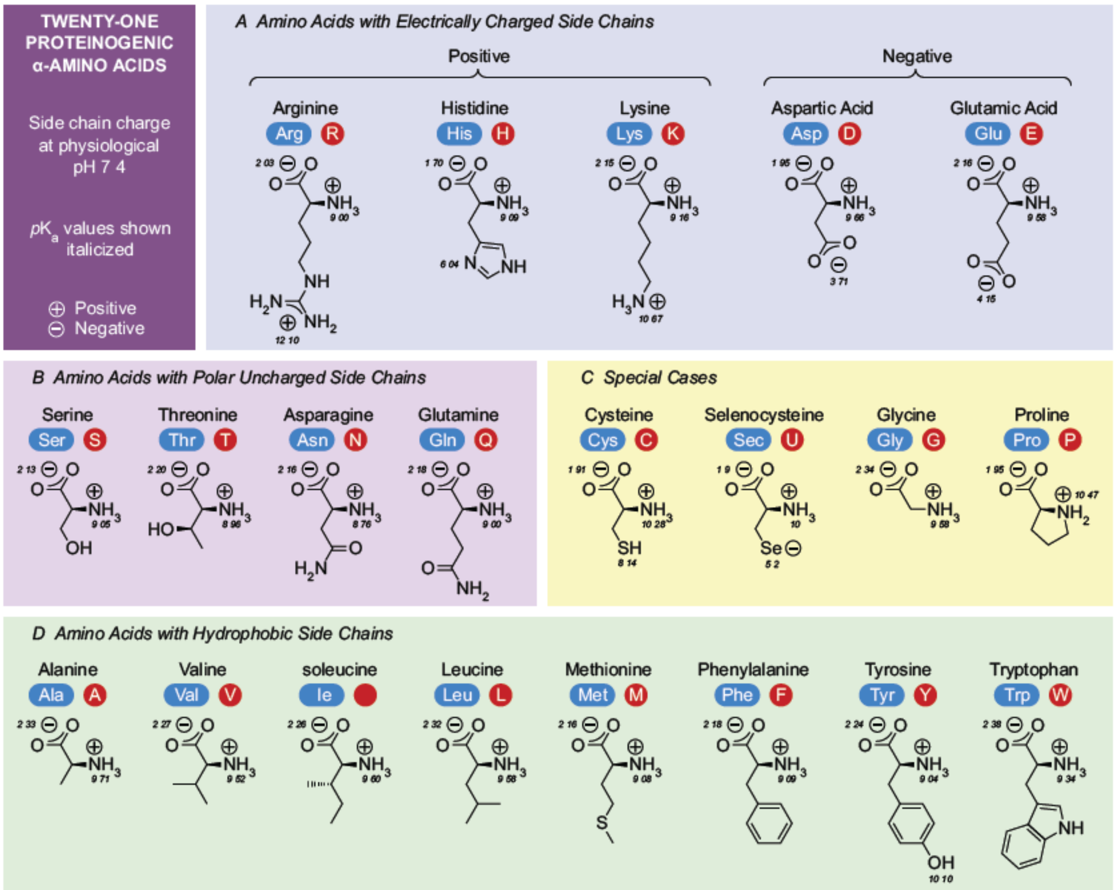
TWENTY-ONE PROTEINOGENIC α-AMINO ACIDS
Side chain charge at physiological pH 7 4
pKa values shown italicized
⊕ Positive
⊖ Negative
A Amino Acids with Electrically Charged Side Chains
Positive
Negative
Arginine Arg R
Histidine His H
Lysine Lys K
Aspartic Acid Asp D
Glutamic Acid Glu E
B Amino Acids with Polar Uncharged Side Chains
Serine Ser S
Threonine Thr T
Asparagine Asn N
Glutamine Gln Q
C Special Cases
Cysteine Cys C
Selenocysteine Sec U
Glycine Gly G
Proline Pro P
D Amino Acids with Hydrophobic Side Chains
Alanine Ala A
Valine Val V
soleucine Ie
Leucine Leu L
Methionine Met M
Phenylalanine Phe F
Tyrosine Tyr Y
Tryptophan Trp W

Figure 3. Twenty-one natural amino acids, adapted from Tungsten Einsteinium [25], licensed under (Creative Commons Attribution-Share Alike 4.0 International)

1.2 Viruses

A further application of protein sequencing is the comparison and classification of closely related viruses [26]. A virus is a microscopic infectious agent that can only reproduce within a cell that it has infected; as such, viruses are considered to be obligate parasites of the cells that they infect. Viral infections can jump from one cell to another via infectious virus particles known as virions [27]. These virions contain genomes consisting of RNA or DNA encapsulated in a protein coat. The term virus, however, will be used in this thesis to avoid confusion. Viruses were first discovered in 1883 [15, 28]. The common structure of a virus is illustrated schematically in Figure 4A. The core component of a virus is its genome, which is composed of double-stranded DNA, single-stranded DNA, double-stranded RNA, or single-stranded RNA, depending on the type of virus. The genome is surrounded by a capsid, which is a protein shell. The capsid can have a rod-like shape, a polyhedral shape, or a shape that is more complicated depending on the type of virus. The structure of a capsid is composed of a large number of protein subunits referred to as capsomeres [15, 29]. Finally, the envelopes of viruses, which are derived from the membranes of the host cell and comprise phospholipids and membrane proteins from the host cell, are present. They also contain virally derived proteins and glycoproteins [30, 31]. Figure 4B shows an example of the structure of an RNA virus, which is the human immunodeficiency virus (HIV). Nevertheless, there are also viruses that do not have lipid bilayer envelopes, also known as non-enveloped viruses (e.g., DNA viruses-adenovirus (AdV), human papillomavirus (HPV), and polyomavirus (PyV). These viruses show different strategies for entering and leaving cells [32, 33].

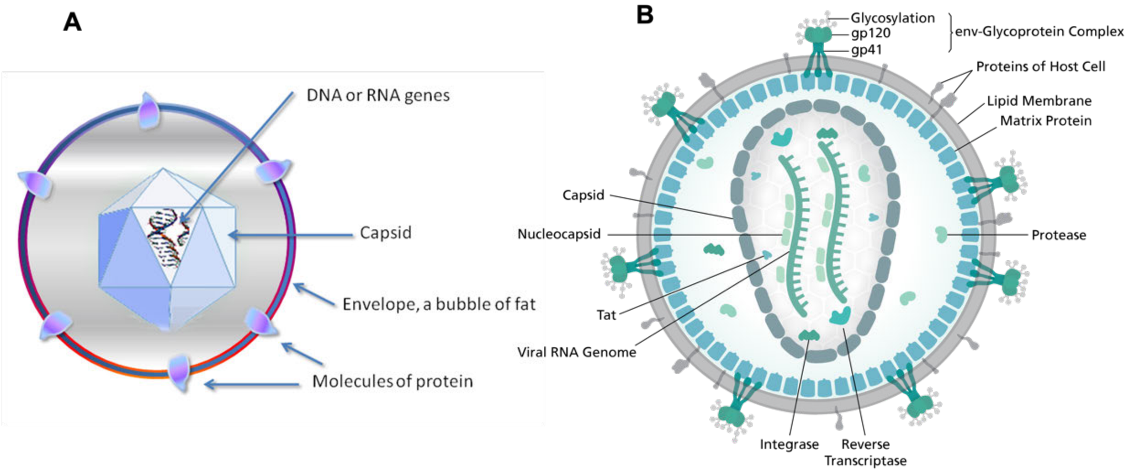
A
DNA or RNA genes
Capsid
Envelope, a bubble of fat
Molecules of protein
B
Glycosylation
gp120
gp41
env-Glycoprotein Complex
Proteins of Host Cell
Lipid Membrane
Matrix Protein
Capsid
Nucleocapsid
Protease
Tat
Viral RNA Genome
Integrase
Reverse Transcriptase

Figure 4. Scheme of virus structures. (**A**) Simplified structure, adapted from Graham Colm [34], licensed under (Creative Commons Attribution-Share Alike 3.0 Unported). (**B**) Structure of an HIV, adapted from Thomas Splettstoesser [35], licensed under the (Creative Commons Attribution-Share Alike 4.0 International).

The diameter of the smallest viruses is only 20 nm smaller than that of ribosomes, that is Adeno-Associated Virus (AAV) [36]. The diameter of the virus that is currently known to be the largest measures 1,500 nm (1.5 μm) which is Pithovirus sibericum [37]. Despite the horrendous statistics associated with human and agricultural epidemics, it is crucial to recognize that viruses can also be advantageous. For instance, viruses play an important role in maintaining ecological homeostasis, they also keep our immune responses active and vigilant, etc. [15, 27].

The investigation of the morphological structure of proteins and viruses is essential for a variety of reasons. To begin, it is necessary to have an understanding of the structure of proteins in order to comprehend their functions. Proteins have distinct structures that enable them to perform particular functions within the body [14]. Second, understanding how viruses infect cells and cause disease requires an understanding of their morphology. In addition, it also facilitates in the detection and classification of viruses [38]. Moreover, information regarding protein and viral structure can also be utilized for therapeutic targets. Many drugs, for instance, inhibit or activate specific proteins. By gaining an understanding of the structure of these proteins, more effective drugs can be designed to target them [39]. The majority of these biological samples are too small to be resolved with a standard light microscope. This is because the Abbe diffraction limit, also known as the Abbe resolution limit, which explains the smallest object size that can be resolved by a microscope. It is determined by the wavelength of the light used to observe the object and the numerical aperture of the objective lens of the microscope [40, 41]. Consequently, high-resolution techniques are required in order to characterize the structures of these proteins and viruses.

Electron microscopy (EM), for instance, is a high-resolution technique that collects electrons that scatter, reflect, or transmit from the sample. Transmission electron microscopes (TEM) and scanning electron microscopes (SEM) are two common electron microscopy instruments. Electron microscopes have significantly higher resolution than conventional optical microscopes, with an electron microscope, a resolution of sub-40-50 pm has been attained [42, 43]. Biological sciences make extensive use of electron microscopy to image the surfaces of samples ranging from protein structure, macromolecule cells, to tissue [44, 45]. Throughout the SARS-CoV-2 outbreak, for instance, electron microscopy has played a crucial role in related research. Using TEM, the structure of the coronavirus with its spike proteins was visualized in exquisite detail [46]. In addition, the 3D structure of the spike protein of SARS-CoV-2 in the prefusion state was resolved with a resolution of 3.5 angstroms using a cryogenic electron microscope [47]. However, an electron microscope cannot be used to characterize living samples, which limits the range of its applications in biosamples. A further issue is the low signal-to-noise ratio, which produces poor image contrast. This is due to the low atomic mass of the elements that make up biological objects (proteins, nucleic acids, carbohydrates, lipids). When electron doses exceed a certain threshold, covalent bonds are irreversibly broken, resulting in the destruction of the very details [48]. Therefore, other imaging techniques that are of interest, such as scanning probe microscopy (SPM), which not only produces high-resolution images but can also be used in a variety of environments, including air, liquid, and vacuum, must be implemented to address the issues. It has the capability to operate in a non-destructive manner [49].

1.3 Scanning Probe Microscopy

Scanning probe microscopy refers to a class of techniques that measures the topography and properties of sample surfaces on an atomic scale. The size, material and geometry of the scanning probe (tip) is an important parameter that determines the spatial resolution that an SPM instrument can achieve. SPM generally is a non-invasive and label-free surface and interface characterization technique [49-51]. The first SPM to be invented was scanning tunneling microscopy (STM) in 1981 by Binnig *et al.*, [52], which enabled the imaging of a (semi) conducting surface with atomic resolution [53]. In scanning tunneling microscopy (STM), a metal tip that is atomically sharp is used to detect small currents from the surface of a conductive object. This procedure is based on the quantum mechanical effect known as tunneling [49]. Shortly after the development of STM, Binnig *et al.,* succeeded in exploiting tip-sample interactions based on atomic forces rather than tunneling current, which led to the invention of the atomic force microscopy (AFM) [54].

- **Atomic Force Microscopy (AFM)**

Since its first application, atomic force microscopy (AFM) has become an extremely important tool in the study of nanoscale science and technology. AFM is a microscopic technique that exploits attractive and repulsive interaction forces between the probe and the sample to image the surface topography. For measuring forces or potential energy, a small probe mounted on a cantilever is used. The cantilever acts as both a force sensor and a force actuator. Included among the forces are van der Waals forces, electrostatic forces, capillary forces, and repulsive forces [55]. A simplified illustration of how an AFM operates can be found in Figure 5. For example, by applying a constant force to the cantilever, it is (gently) pushed on the sample. When the cantilever is scanned over the sample surface, the different tip-sample interactions cause changes in the bending of the cantilever. These changes are detected with a fourquadrant photodiode, which collects the deflected light of a laser beam focused on the cantilever and converted it into an electrical signal. The detection of these changes allows the imaging of the topography and the determination of the height of the specimen under investigation. The cantilever's deflection determines the amount of force that the probe is subjected to; the larger the deflection, the greater the force. These electrical signals are recorded and then converted into images. In this manner, information regarding the topography and mechanics of the samples can be obtained [56, 57].

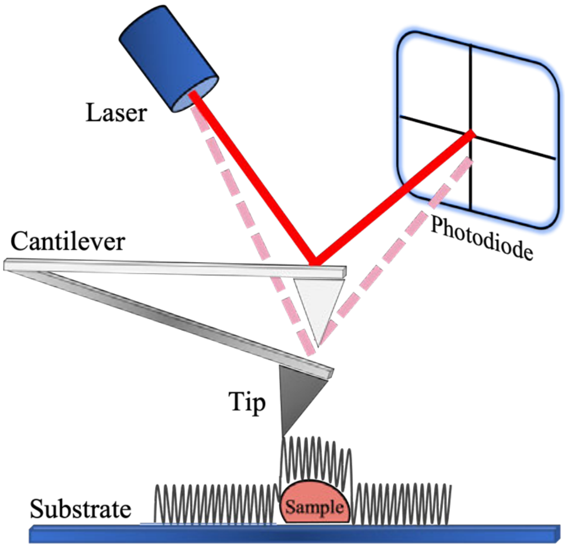

Figure 5. Sketched AFM setup working in intermittent contact mode (not to scale). A laser beam is focused on the cantilever where the tip is mounted. The bending of the cantilever responds differently depending on the tip-sample interactions that are being measured. A photodiode with four quadrants is used to recognize these changes.

Based on the specific operation, the imaging modes of AFM can be divided into contact mode, intermittent contact mode, and non-contact mode, with the first two being the most common ones. In the earliest applications of AFM, contact mode was predominantly used to produce images with high resolution. This mode requires that the AFM tip remains in constant contact with the sample surface throughout the scanning process. However, the applied normal force may also lead to a significant lateral force being applied to the sample. As a direct consequence, this can lead to problems with sample damage, or even removal from the substrate, in the case of soft and easily deformed samples or weakly adsorbed samples (e.g., biological samples) [58, 59]. Especially when measured at room temperature, a capillary layer of water forms between the tip and the surface. This has the effect of "pulling" the AFM tip onto the surface, often applying a greater force than the force initially applied (via the set point). And thus, it is easy to unintentionally apply a significant force to the samples [59].

The intermittent contact mode (IC-AFM) was introduced as a solution to address this problem. The cantilever used in the IC-AFM is driven to oscillate vertically near its resonant frequency, and the tip of the cantilever is in contact with the sample surface for a short time during each tap/oscillation. Furthermore, the interaction force between the tip and sample is controlled by the amplitude of the tapping, which can be adjusted to minimize the force applied to the surface and reduce the risk of sample deformation or damage [59, 60]. In order to obtain topographic information about the sample, the change in amplitude is always used as the input parameter of the feedback loop. The feedback loop operates by measuring and comparing the cantilever's amplitude to a reference amplitude. If the cantilever is not at the desired amplitude, the feedback loop sends an electrical signal to the piezoelectric, which adjusts the cantilever height to the correct position to keep a consistent amplitude. This process is repeated multiple times, enabling the AFM to maintain a stable position and measure forces with high sensitivity and resolution. A change in the phase of the cantilever oscillation also takes place while the scanning procedure is being carried out, and this reflects different material properties [61].

For imaging biological specimens, especially proteins and viruses, AFM has advantages over conventional microscopes and other imaging methods. Due to the fact that AFM imaging does not require staining, labeling, or coating of samples, direct imaging of these structures with relatively limited sample preparation is possible. For instance, using atomic force microscopy (AFM), it is possible to not only obtain high-resolution three-dimensional images of protein surfaces, but it can also observe the conformational changes of proteins influenced by external conditions. This can provide valuable insight into the structure and function of proteins at the molecular level. Additionally, it can be used to examine the dynamic structure of proteins in liquid environments [62]. In contrast, one of AFM's disadvantages is that it cannot be used to retrieve direct, detailed chemical information. An additional technique, such as vibrational spectroscopy, must be employed for this purpose.

1.4 Raman Spectroscopy

Multiple phenomena can be observed when electromagnetic radiation interacts with matter. Since matter is capable of absorbing, emitting, transmitting, and scattering light, these effects can be exploited, for example, to characterize the molecular structure of organic, inorganic, and biological samples. A valuable tool in the field of vibrational spectroscopy is Raman spectroscopy. Two scattering processes are distinguishable: inelastic Raman and elastic (Rayleigh) scattering [11, 63, 64]. During a scattering process, the vibration of a molecule is excited by a photon from the ground state to a virtual state. If the energies of scattered and incident light are equivalent, this phenomenon is known as Rayleigh or elastic scattering (see Figure 6). If the energies of scattered and incident light differ, the phenomenon is known as inelastic scattering or Raman scattering [11], which can be divided into two categories: Stokes scattering (where the energy of scattered light is less than that of incident light) and Anti-stokes scattering (energy of scattered light is higher than incidence light) [65]. The technique to detect these scattering processes is called Raman spectroscopy. Since the transitions are connected to molecular vibration, it falls under the category of vibrational spectroscopy. A simplified representation of both of these phenomena is shown in Figure 6. The vast majority of the scattered light is scattered elastically, while only one photon out of every 10^6-10^{10} is scattered inelastically [66]. Therefore, the detected Raman signal is extremely weak and can only be used for bulk samples.

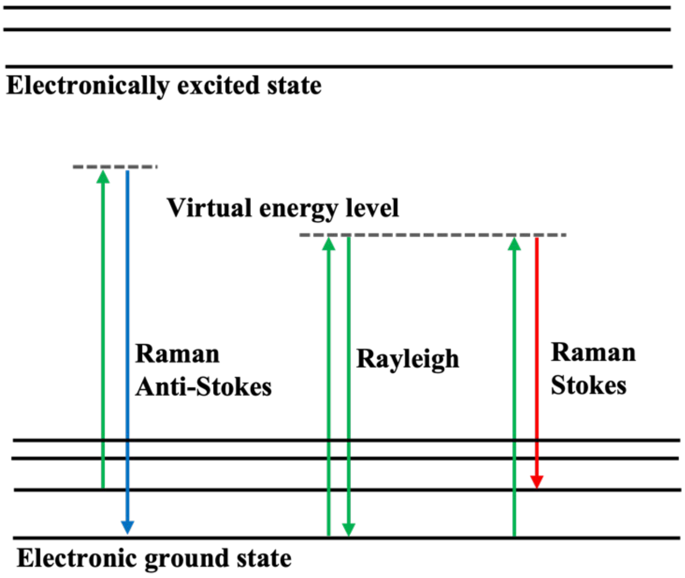

Figure 6. Energy diagram of Raman spectroscopy. Raman stokes with scattering energy less than that of the incidence light (green and red arrows), Raman anti-stokes with scattering energy larger than that of the incidence light (green and blue arrows), and Rayleigh scattering with scattered energy equal to that of the incident light (green arrows).

There is a correlation between the variations in energies and the vibration of chemical bonds. As spectral bands can always be assigned to particular molecule vibration modes, a Raman spectrum is frequently regarded as a fingerprint of the molecule [67]. Raman spectroscopy has many advantages over other methods, such as techniques that require sample labelling or extensive sample preparation, due to its high level of specificity as well as its wide range of applications [68, 69]. However, to be able to employ Raman spectroscopy for high-resolution applications, there are a couple of challenges that need to be addressed. These challenges include low sensitivity and diffraction-limited spatial resolution.

1.5 Surface-Enhanced Raman Spectroscopy (SERS)

SERS was developed to increase the Raman detection sensitivity by several orders of magnitude in the 1970s [70-72]. It is a phenomenon that results from the combination of the light-metal interaction (also known as the plasmonic process) and the interaction between light and molecules (Raman spectroscopy). When an incident light hits the interface between metal and dielectric, the electromagnetic wave causes the delocalization conduction electrons in the metal nanostructures to begin collectively oscillating. Surface plasmon resonances (SPR) are excited when the frequency of the incident light coincides with the intrinsic oscillation frequency of free electrons in the metal. The resonance frequency depends on a variety of parameters, including the size and shape of the particles, the dielectric environment, the electron density of the particles, etc. [73]. Figure 7 illustrates the diagram of a localized surface plasmon resonance (LSPR).

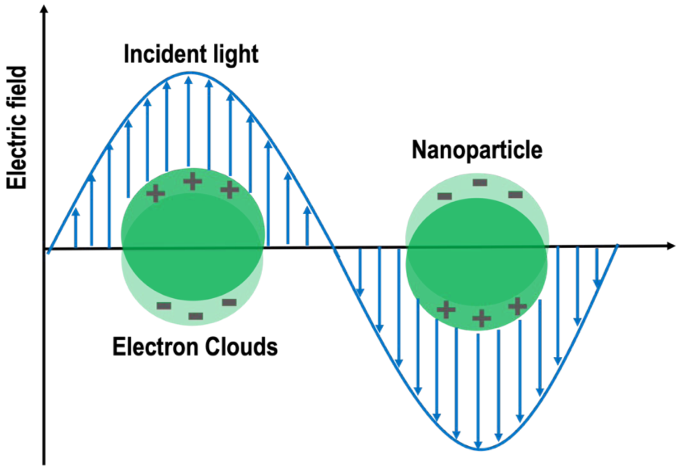

Figure 7. Schematic diagram of localized surface plasmon resonance (LSPR). Lightwave (blue curve), nanoparticles (green sphere). A resonance condition is met when the incident electromagnetic field matches that of the oscillating electrons on the nanoparticle's surface [74].

Plasmonic nanoparticles (PNP) are nanoparticles that exhibit strong SPR in the visible to the near-infrared region and can generate a strong LSPR. These nanoparticles are typically composed of Ag (silver), Au (gold), or Cu (copper). For the bioanalytical application of SERS, two of the most often utilized materials are gold and silver. Because of their high level of biocompatibility, gold nanostructures are frequently used in intracellular or in vivo research because they are effective for excitation at wavelengths longer than 600 nm. Ag nanomaterials are useful for excitation at wavelengths between 400-600 nm because of the plasmon resonance in this wavelength region. Ag is rarely used for in vivo analysis due to its high toxicity to living systems, but it is effective for ultrasensitive in vitro detection, [73, 75, 76]. In protein analysis, SERS can provide detailed structural information of proteins under physiological conditions, unrestricted by protein molecular mass or solubility. In most cases, researchers use two different approaches when conducting SERS-based research on proteins. The first seeks to directly probe intrinsic protein structural information, and the second obtain SERS or Raman labels in order to indirectly quantify or qualify proteins [77].

The light that initially entered the system will either be resonantly absorbed or scattered as a result of LSPR. Consequently, the incident light energy is able to be effectively coupled into the metal nanoparticles, which results in an enhancement of between two and five orders of magnitude in the local electromagnetic field intensity at the nanoparticle surface. This is the key to the generated electromagnetic enhancement in SERS [78]. The Raman intensities of molecules that are located in the near field region of SERS substrates can be dramatically enhanced with the assistance of LSPR, and the resulting enhancement can be up to 10^{11} times higher [79]. Moreover, another enhancement known as chemical enhancement can also contribute to the overall observed band intensity increase. This refers to a change of polarizability that takes place when a molecule interacts with the surface of a metal [66]. This can lead to a change in the selection rules and vibrational modes that are inactive in standard Raman spectroscopy become active. As a result, the band positions can shift so that the SERS spectra can differ significantly from the Raman spectrum [80].

Despite the fact that SERS is capable of increasing the detection sensitivity of Raman scattering which can detect concentrations as low as 10 pmol with the assistance of chemometric analysis, and all the way down to a single molecule [80], it is still limited by the Abbe diffraction due to the fact that it is a lens-based optical microscope technique. As a result, it is not possible to obtain high-resolution images, which limits its applicability. To address this issue, tip-enhanced Raman spectroscopy (TERS) was developed. This technique combines high-resolution imaging from SPM (AFM and STM) with plasmonic nanoparticles similar to SERS in order to obtain both topography and chemical information from samples (e.g., proteins and viruses) in a single experiment [81].

1.6 Tip-Enhanced Raman Spectroscopy (TERS)

TERS is a high-precision Raman spectroscopy detection method that typically uses a metal tip of a scanning probe microscope for sample topography imaging and Raman scattering [76, 82]. Zenobi, Kawata, Anderson, and Pettinger independently reported TERS results for the first time in 2000, demonstrating the viability of TERS [83-86]. An enhancement of the vibrational modes of the molecules under investigation is achieved by a single nanoparticle at the tip apex. In the experiments, either etched metal wires are used for STM-TERS or a nanoparticle-coated AFM probe for AFM-TERS. The excited plasmon resonance of the single nanoparticle at the tip apex is the result of the plasmon coupling of all adjacent nanoparticles that are illuminated. This effect, in turn, is determined by the material, size, and geometry of the nanoparticles [87]. The previously mentioned matching of the laser wavelength and surface plasmon resonance unquestionably has an impact on the choice of material for the tip of the TERS. According to the results of the TERS study, gold tips are utilized for excitations ranging from 620 to 785 nm, whereas silver tips are utilized for experiments carried out in the range of 488 to 568 nm [76, 88].

There are typically two types of TERS setups, known as AFM- and STM-TERS. A highly intense evanescent field should ideally be generated at the apex of the probe at a single individual nanoparticle that interacts with the molecules of the sample. Controlling the distance between the tip and the sample is another extremely important parameter in the TERS experiments. For sensitive surface scanning as well as optimal and stable Raman signal enhancement, the tip-sample distance must be precisely controlled via a feedback loop. It is important to note that spectra are only collected from molecules that are directly localized beneath the tip apex. Since the Raman signal enhancing field is confined to a few nanometers around the apex, and a spatial resolution in the (sub)nanometer region – independent of the ambient conditions – can be reached optimally in STM- and AFM-TERS [89-93].

The AFM-TERS features a feedback mechanism that is controlled by force. By contrast, STM-TERS is based on the bias current and voltage, which are the regulating parameters that ensure constant electron tunneling and maintain the tip-sample distance via a feedback loop. Moreover, the generation of tunnel current requires a substrate made of a conductor or semiconductor. Therefore, STM is suitable for studying samples with high conductivity, or it requires conductive substrates with a thin sample that allows the tunneling of the electron whereas AFM has no conductivity requirements. In addition, STM-TERS substrates are mostly opaque, so that the incident light must illuminate the metal tip from the top or from the side [76, 88].

A standard TERS experiment typically starts with the positioning of the tip in the laser focus. This step can be carried out with either a tip scanner [94], a laser scanner [95], or an objective scanner [96], depending on the system. After the tip has been fixed in the laser spot, the sample is moved, while the tip position remains unchanged in the laser focus throughout the experiment. In the next step, a topography overview image of the sample surface is scanned. Then, the region of interest for TERS spectra acquisition is defined, and the spectra are either recorded at predefined points or collected pixelwise simultaneously to a further topography scan. In most cases, a laser power in the range of μ-mW is sufficient for obtaining spectra with an acquisition time of 0.1–30s [76, 97].

An SPM can be assembled with a Raman system in a variety of configurations, including bottom illumination, side illumination, and top illumination [76]. Back-reflection geometry (bottom illumination) offers a high collection efficiency, especially when employing oil immersion objectives with a high numerical aperture N.A. (1.4–1.6). This geometry is the most effective optical configuration for TERS to date even though they can only be used with transparent samples, such as glass slides or mica sheets [81]. In contrast, side-illumination and top-illumination optics are necessary when investigating opaque samples. In configurations with side illumination, longer working distance objectives with a smaller numerical aperture are necessary. Moreover, due to the angle between the sample and excitation beam, the focused spot in a side-illumination geometry becomes elliptical and larger, necessitating a higher laser power for equivalent outcomes [97]. For top-illumination, shadowing effects from the tip must be taken into account, and normally, cantilevers with a protruding tip are used to eliminate shadowing. In addition, compared to a side-illumination configuration, a top-illumination geometry has a smaller far-field contribution and is easier to integrate into a conventional microscope system [98]. In the present thesis, a bottom illumination AFM-TERS configuration was used (see Figure 8). A 60x oil immersion objective with a high numerical aperture (NA 1.45) was utilized to illuminate the TERS tips with a 532 nm laser beam and the collection of the scattered light followed the same optical path. The coating of the AFM with silver nanoparticles was achieved by evaporation.

There are selection rules in Raman spectroscopy. These rules are a set of criteria that determine whether a particular vibrational transition in a molecule is active meaning it will produce a Raman scattering signal, or Raman inactive, meaning it will not produce a signal. The primary selection rule for Raman spectroscopy is that the transition must result in a change in the polarizability of the molecule [99-101]. In SERS and TERS, the selection rules determine which Raman scattering signals will be observed and which will be suppressed, resulting in acquired spectra that vary and deviate from conventional Raman (i.e., distinct band positions and intensity) [76, 81]. These rules depend on a number of factors, including the polarization of the excitation light, the polarization of the scattered light, the orientation of the molecule with respect to the tip (TERS) and metal nanoparticle surface (SERS), and the polarizability of the studied molecule [102, 103]. For instance, the most intense bands in TERS are typically associated with chemical groups whose vibrational modes are aligned parallel to the TERS tip main axis. In contrast, weak bands are frequently observed for chemical groups whose vibrational modes are oriented in the plane perpendicular to the tip axis [104].

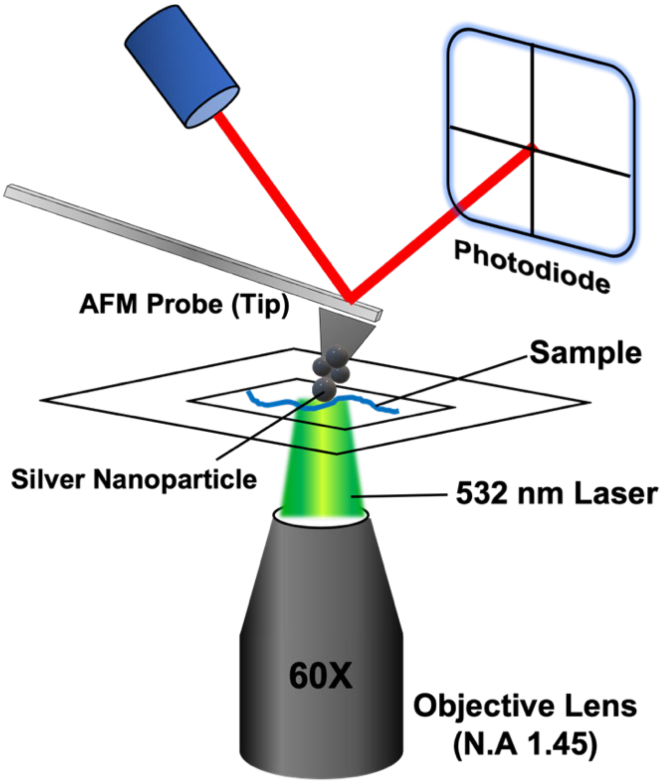

Figure 8. A schematic diagram of the AFM-TERS setup with bottom illumination equipped with a cantilever probe, a photodiode for the detection of the deflected AFM laser, a Raman laser, and a transparent sample. A high numerical aperture (1.45) objective lens is used to focus and collect the light. A 532 nm wavelength is used to excite the silver nanoparticles attached to the AFM probe.

This phenomenon can also be observed in the dissertation's findings, which will be explained in detail in Chapter 2 specifically. In addition to this, when the tip continually touches the sample, as is done in experiments using the contact mode of the AFM-TERS. A process like this can result in pressure-induced changes to the orientation of the molecules being probed, which can cause spectral fluctuations [76]. The spectral fluctuation and decreased intensity can also be observed when intermittent contact mode is used in the TERS experiment, which is directly related to the distance between the tip and sample [105, 106].

In terms of spatial resolution, the first TERS experiment with the sub-nanometer resolution was conducted on protein analysis by Deckert–Gaudig *et. al.*, [90]. By examining the molecular structure of fibril surfaces immobilized on ultra-flat gold crystals, they have reported a lateral resolution of below 1 nm. Using a very small step size of 0.5 nm between each point, significant differences were observed in both the spectral intensities and band positions. Another TERS experiment with the subnanometer resolution was carried out on porphyrins using STM-TERS under low-temperature, high-vacuum conditions. The surface configuration and inner structure of a single molecule were both resolved as a result of this experiment [92]. In addition, STM-TERS experiments on carbon nanotubes (CNTs) with a resolution ranging from 1.7 nm [89] down to 0.7 nm can be carried out at a low temperature and under ultrahigh vacuum conditions [107]. Furthermore, in biological applications employing TERS, Zhe *et al.* reported the potency of label-free DNA and RNA sequencing using TERS, with a spatial resolution of less than 1 nm. This was accomplished by acquiring TERS spectra along a phage single-stranded DNA [108] and a clustered regularly interspaced short palindromic repeats (CRISPR)-associated protein 9 (Cas9) single-stranded RNA [109].

Similarly, TERS has been extensively utilized to characterize protein structures. For instance, TERS has been used to investigate both the amino acid composition and protein secondary structures of insulin amyloid fibrils. This allowed mapping of the fibrils' hydrophobic and mixed hydrophilic/hydrophobic domains. The secondary structure of a protein was characterized by evaluating amide I and amide III bands [110]. Moreover, it has also been used to map the conformational difference between different aggregates at each stage of the Aβ fibril maturation process in a liquid medium [111]. Additionally, tip-enhanced Raman spectroscopy (TERS) could also be utilized to elucidate the protein secondary structure as well as the amino acid composition of the virus surface (Bacteriophage MS2) [112].

In this work, AFM and plasmon-enhanced Raman spectroscopy (SERS and TERS) were used to characterize the various levels of protein structures. In the first study, AFM and TERS were used to analyze the primary structure of proteins by identifying different amino acids to develop a TERS-based method for direct protein sequencing. In the second study, AFM and SERS were used to characterize the secondary structure of the proteins by analyzing the change in the secondary structure of insulin amyloid fibrils. In the last study, AFM and TERS were employed to identify and investigate the protein structure besides other biopolymers such as lipid and nucleic acids in SARS-CoV-2. In all experiments, AFM was used to image, the topography of the samples and select the regions of interest. The chemical information from these areas was obtained with TERS and SERS, respectively.

CHAPTER 2
RESULTS

Identification of Single Amino Acids towards Direct Protein Sequencing with Tip-Enhanced Raman Spectroscopy

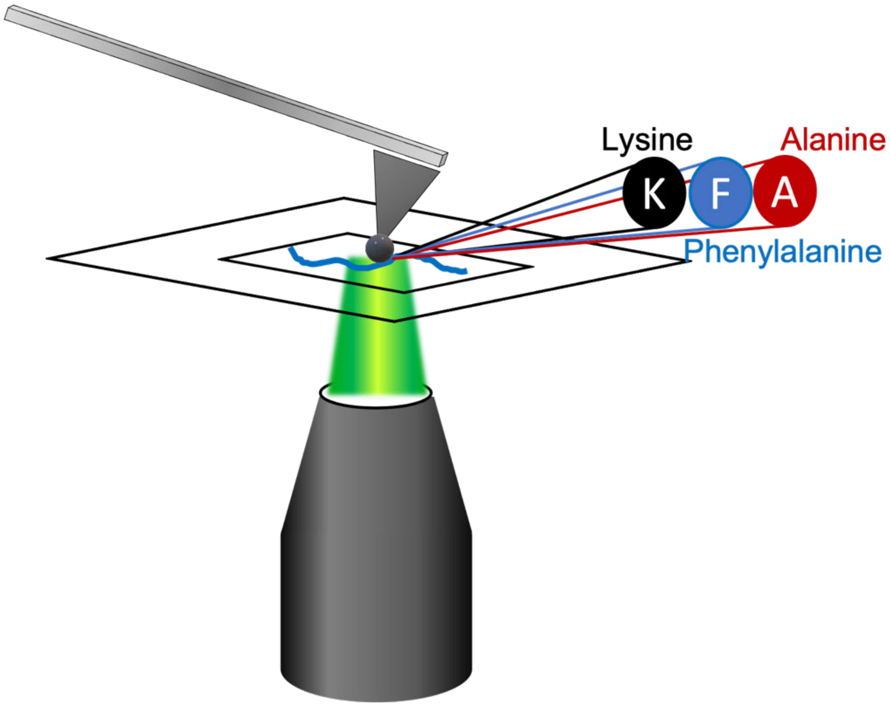
Lysine
Alanine
K
F
A
Phenylalanine

2.1 Introduction

Proteins are one of nature's most important macromolecules. Many functions within the cell are carried out with the help of various types of protein molecules. Protein structures are similar despite their different functions. Because of their importance, it is critical to identify details about their structures, synthesis, functions, and regulations. The first step in determining a protein's structure is to determine its amino acid composition [1, 113]. Protein sequencing is a method that can be used to determine the sequence of amino acids within a protein, as well as its order and conformation. Understanding both the structure and the function of proteins is necessary in order to have the capacity to comprehend the biological process. Protein sequencing can be used for a variety of purposes, such as determining the protein family to which a certain protein belongs and the evolutionary history of that protein. Second, an analysis of the protein's target sequence to provide an accurate estimate as to where in the cell it will be found. Third, the prediction of the gene sequence encoding the specific protein. Lastly, discovering the structure and function of a protein using a combination of computational and experimental techniques [114].

There are currently two primary methods available for sequencing and identifying proteins that do not involve affinity reagents such as antibodies: The Edman degradation [115] as well as the mass spectrometry [116]. Edman degradation was the first method that was used to determine the sequence of amino acids in a peptide that had been purified. This technique, created by Peer Edman, involves chemical modification of the N-terminal amino acid, cleavage of this amino acid from the peptide, and identification of the cleaved marked amino acid through the use of high-performance liquid chromatography [117]. Due to the requirement for highly pure peptides, massively parallel sequencing of this type was not feasible until very recently. In many instances, it also proved unable to assign a suitably lengthy peptide sequence (>50 amino acids), and the procedure failed totally if the protein's amino terminus was acetylated or otherwise blocked from the Edman reaction, which requires a free amino terminus.

In spite of this, one potential solution to the problem is a technique known as fluorosequencing, which combines Edman chemistry, single-molecule microscopy, and a stable synthetic fluorophore. This technique enables the sequencing of millions of different peptide molecules in parallel, as well as their identification and digital quantification on a zeptomole scale [118]. However, the technology is not without difficulties, as the reagents used in Edman degradation chemistry increase the rate of fluorescent dye destruction, limiting the read length. In addition, inefficient labeling can also contribute to errors, making direct protein sequencing impractical.

Mass spectrometry (MS), which ionizes biomolecules and measures their mass by following their specific trajectories in a vacuum system, displaced Edman degradation in the 1990s because it is much more sensitive and can fragment the peptides in seconds rather than hours or days. Furthermore, MS does not require homogeneous purification of proteins or peptides and has no trouble identifying blocked or otherwise modified proteins [116, 119]. On the other hand, not all peptides can be ionized and transmitted through the mass spectrometer effectively, before detection, they must undergo enzymatic digestion and/or fragmentation. In addition, charge state distributions may overlap over a particular mass or in the case of mixes, which can make it difficult to identify individual species. Furthermore, accurate detection using MS often requires the use of expensive equipment in addition to a high number of samples (e.g., a million copies or an attomole of a protein) [120]. In contrast to PCR (polymerase chain reaction) for DNA, there is currently no high-throughput technology for creating multiple copies of a single protein, which limits the detectable concentration of a particular protein [121]. Another promising approach is the use of nanopore technologies.

Nanopore sensing has advanced dramatically since its first demonstration as a single-biomolecule sensor, eventually achieving the goal of a single-molecule DNA sequencing [122]. However, when it comes to using the method for protein sequencing, it is met with many well-known challenges related to the complexity of proteins. Some of these challenges include the heterogeneity of the protein as well as the relatively large number of amino acid side chain residues. The fact that proteins are made up of combinations of 20 distinct amino acids as compared to the 4 nucleobases that are found in nucleic acid makes it much more difficult to assign the ionic current signals to the amino acid sequence. More problems are associated with post-translational modifications and more difficult control of unfolded protein transport through the nanopore. In addition, proteins are not uniformly charged, unlike DNA, which has one phosphate in the polymer backbone for each base. This makes the direction of polypeptide movement more unpredictable, which, of course, would make it difficult to sequence proteins [117, 123, 124].

The primary objective of the study is to collect data and information regarding the potential applications of TERS as a new approach to direct protein sequencing. There are two obstacles that are generally encountered while trying to sequence proteins using TERS. In order to begin the sequencing process efficiently, the protein or peptide must be 1-dimensional, in other words, the tertiary and secondary structure must be dissolved leaving a linear chain of amino acids (primary structure). Another issue is whether TERS can distinguish amino acids with a similar structure as well as their order in the peptide chain. As a result, in this research, I attempted to overcome the first challenge by combining a peptide with a known sequence with an organic molecule to create a stretched/unfolded peptide structure, which is characterized with an AFM prior to the TERS experiments.

2.2 Experiments

2.2.1 Sample Preparation

A synthetic peptide H_2N-KKKFAFAFAFAKKK-COOH (KFAK) (purity ≥ 95%, Peptide Elephants) (K: lysine, F: phenylalanine, A: alanine) and 4,4-Bipyridyl molecule (4Bpy) (99%, Sigma-Aldrich) were used in the experiments. The peptide and organic molecule were dissolved in pH 7 aqueous solution with a concentration of 100 µM, with a ratio of peptide to 4Bpy 1:1. The adduct was incubated at 37°C for 7 to 14 days and at 70°C for 24 hours. An illustration of the sample preparation scheme is provided in Figure 1. After aliquot samples were taken from each incubation period, the samples were directly stored at -21°C. A pre-cleaned glass slide, which was previously treated with $HNO_3/H2O_2$ (3:1) for 2.5 h and dried under argon was used as substrate. The sample was characterized by AFM and TERS.

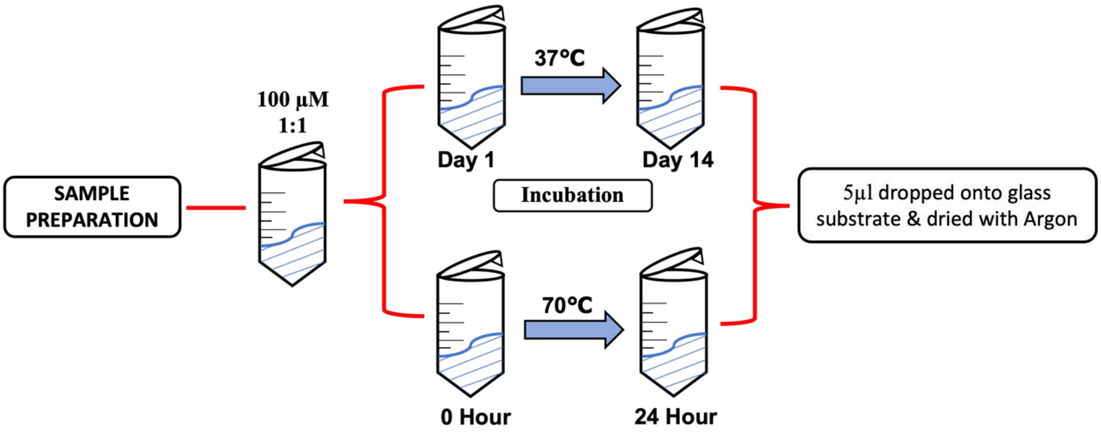

Figure 1. Sample preparation scheme. KFAK peptide-4Bpy adduct with a concentration of 100 µM. Two different incubation strategies were used, one at 37°C up to 14 days and the other at 70°C for 24 hours.

2.2.2 AFM Topography Measurements

AFM measurements were performed with a JPK NanoWizard I (Bruker-JPK BioAFM, Germany) in intermittent contact mode. Tap 190Al-G cantilevers (Budget Sensors, Bulgaria) were used. A 5 µL drop of the sample adduct was added onto a pre-cleaned glass slide and dried with argon. The sample was then rinsed by applying a 5 µL drop of distilled water, followed by suction, and dried again with argon. 1-10 µm images were scanned with a 256 x 256 pixels resolution. Measurements were performed daily for seven days plus on days 10 and 14 for samples incubated at 37°C, and every 2h, 4h, 6h, 8h, and 24h for samples incubated at 70°C. Topography images were offset corrected by applying a line-by-line polynomial fit procedure or a plane correction (JPK imaging processing software, Bruker-JPK, Germany).

2.2.3 TERS Measurements

TERS measurements were performed using a transmission setup with back-scattering geometry. The TERS setup included a Raman spectroscope connected to an AFM (Nano Wizard III, JPK Instrument AG). The glass slide containing the adsorbed KFAK peptide-4Bpy adduct was mounted on the sample holder and illuminated from below. The excitation laser was focused on the sample and the AFM tip using an oil immersion objective with a magnification of 60x (Olympus, NA 1.45) (Figure 2).

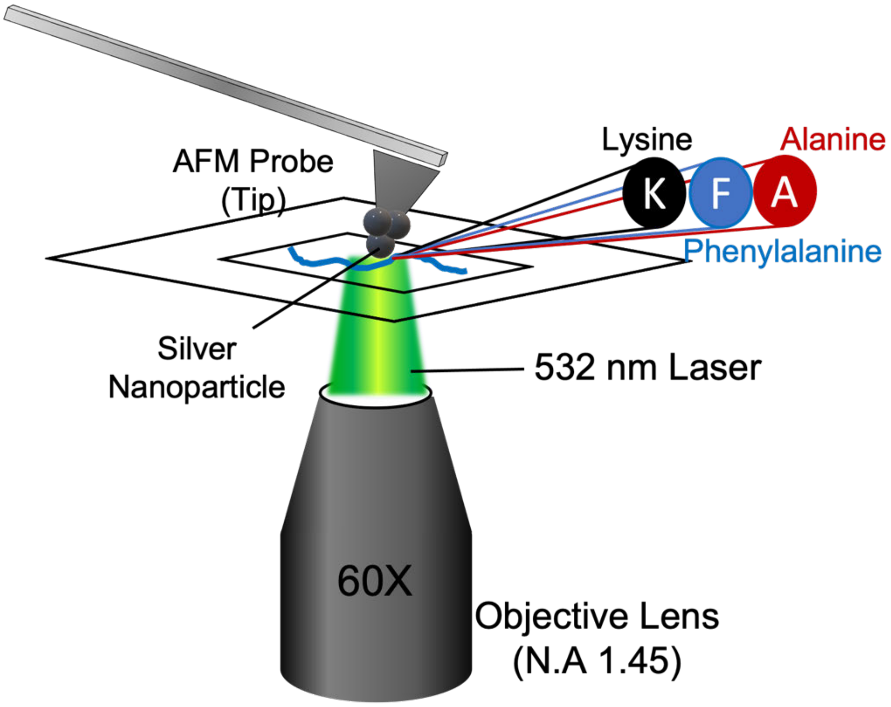

Figure 2. TERS setup for characterizing the KFAK peptide-4Bpy adduct. A high numerical aperture (1.45) objective lens is used to focus and collect the light. 532 nm wavelength is used to excite the sample and the silver nanoparticle attached to the AFM probe.

Traditional AFM probes (TAP190 Al-G, average resonance: 160 kHz), suitable for intermittent mode, were coated with ~25 nm silver stored in an argon atmosphere until used as TERS tips. The silver is thermally evaporated in a vacuum [86, 125]. The evaporation process generally produces tips covered with silver island films, whereas sputtering yields smoother films [76]. As excitation, a laser with a wavelength of 532 nm and a power of 550 μW on the sample was used and was coupled to the inverse microscope (Olympus). A closed-loop XY piezo scanning stage was used to scan the samples. Following a scan of the peptide surface, up to 100 distinct points with 0.5nm-

5nm step size were designated (Figure 3). The tip and sample were then irradiated with the laser, and a TERS spectrum was recorded with an acquisition time of 1s for each point on the line. For better visualization, all raw spectra were imported into Igor-Pro 7.08 32-bit (WaveMetrics Inc. USA) and arranged with a y-offset. There was no further data processing.

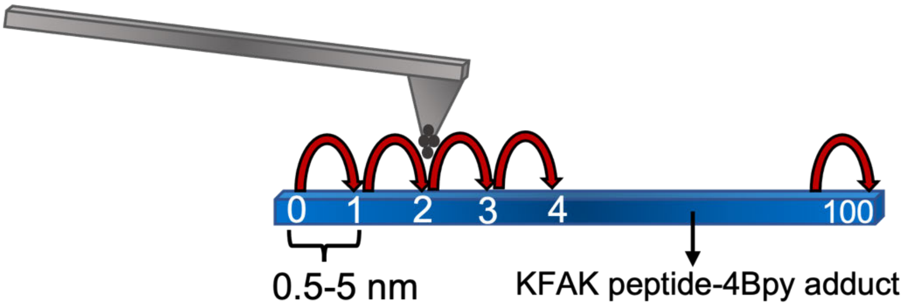

Figure 3. TERS measurement scheme of KFAK peptide-4Bpy adduct. On the structure of nanofibrils, up to 100-point measurements were determined. Two different step sizes were used (0.5 and 5 nm).

2.3 Results and Discussion

2.3.1 AFM topography of samples incubated at 37°C

Initially, an experiment based on the study by Liu *et. al.*, [126] was performed where 2D nanopatches composed of an adduct of an amphiphilic-like peptide (H_2N-KKKFAFAFAFAFAKKK-COOH) and 4Bpy were produced in a 1:1 ratio at a concentration of 100 µM. After up to seven days of incubation at 37°C, the formation of these nanopatches structures was expected. However, the current findings demonstrate that the results from the literature were not reproducible. Instead of nanopatches, nanofibrils were obtained. Figure 4 illustrates the AFM topography of the nanofibrils from day 1-7, and also additional at day 10, and 14. Figure 4 (D1-D3) shows the AFM topography from days 1-3 of incubation, which illustrates that the majority of the adducts still contain structures with a globular shape with an average height between 5-18 nm. From day 4-7, some nanofibrils with an average height between 2 and 8 nm can be observed, as illustrated in Figure 4 (D4-D7). The incubation then continues for up to 14 days. On day 10, as shown in Figure 4 (D10), a nano patch-like structure with a height of 4 nm was also observed. Nonetheless, it was not discovered everywhere on the sample; some regions still contained only nanofibrils and globular structures. After incubation for 14 days, the majority of the structures were either stacked nanofibrils (2-5 nm) or globular particles (5-15 nm), which is illustrated in Figure 4 (D14).

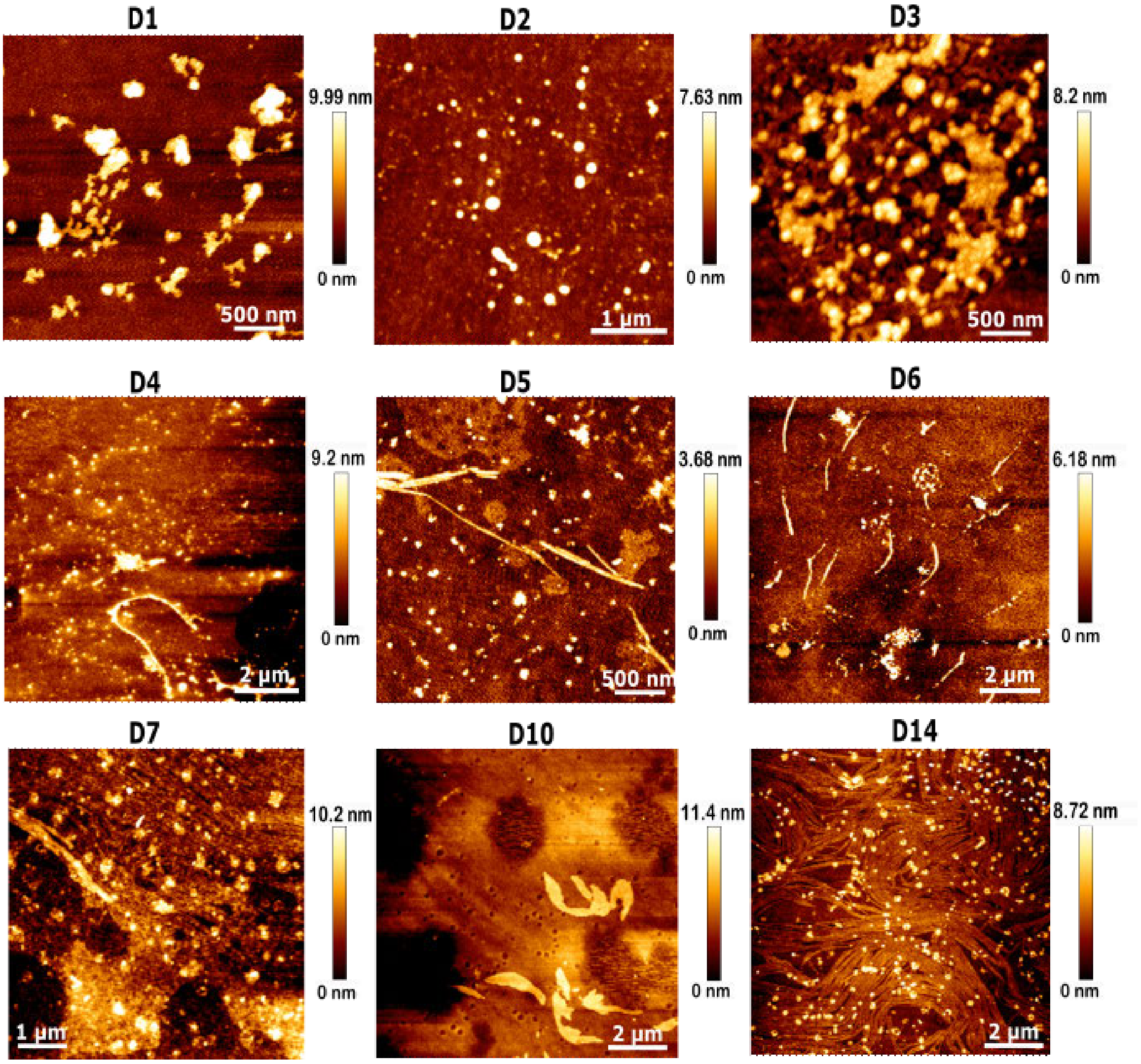
D1
9.99 nm
0 nm
500 nm
D2
7.63 nm
0 nm
1 µm
D3
8.2 nm
0 nm
500 nm
D4
9.2 nm
0 nm
2 µm
D5
3.68 nm
0 nm
500 nm
D6
6.18 nm
0 nm
2 µm
D7
10.2 nm
0 nm
1 µm
D10
11.4 nm
0 nm
2 µm
D14
8.72 nm
0 nm
2 µm

Figure 4. AFM topography of the KFAK peptide-4Bpy adduct incubated at 37°C showing the nanofibril development from day 1 to day 7, days 10 (appearance of nano patch), and days 14 (nanofibril).

As was previously stated, the results differed from that of Liu *et. al.,* [126]. In their research, the growth of a nanopatches rather than nanofibrils were observed. It can only be speculated why the results differed. It could be due to the lack of experimental details in the publication, which prevented accurate adherence to the protocol. Using STM, the authors illustrated that the peptide in the KFAK-4Bpy adduct adopts a stretched/unfolded structure. Nevertheless, since the objective was to open or unfold the globular structure of the peptide, the nanofibrils are also suspected to have an open arrangement as indicated by the difference in morphology (fibrils-like) as well as in topography height, which is flatter than the globular structure.

The next step was to verify, whether the nanofibrils grew only due to the presence of 4Bpy. Thus, a reference experiment was performed where the pure peptide (KFAK) and pure (4Bpy) solutions were incubated separately under the same conditions. The results in Figure 5 demonstrate that no nanofibrils formed on either day of the incubation period (day 1-7). The vast majority of the structures exhibit spherical to elliptical shapes with a height between 7-12 nm for 4Bpy and for KFAK-peptide between 10-70 nm, respectively. This observation led to the conclusion that the grown fibrils in Figure 4 must contain both components in terms of an adduct. According to the literature, the 4Bpy molecule acts as a non-covalent linker by forming hydrogen bonds to the N-terminus or C-terminus of the peptide. It was suggested that the 4Bpy molecule interacts with the peptide's termini rather than with the side chain residues [126]. Therefore, since the ratio employed is 1:1, it is also possible to stipulate that the structure of the KFAK peptide-4Bpy adduct is alternating (e.g., KFAK-4Bpy-KFAK-4Bpy-KFAK-4Bpy).

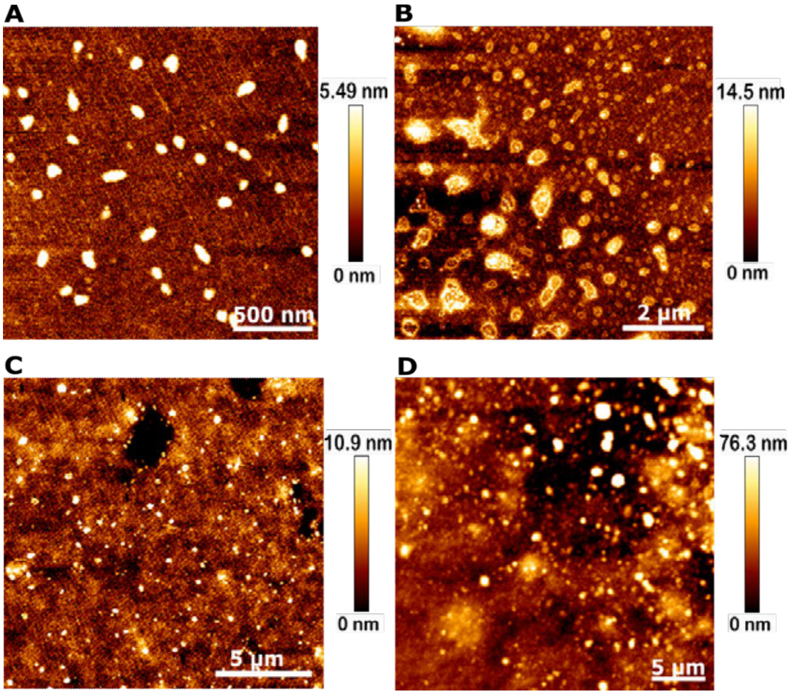

Figure 5. AFM topography of pure 4Bpy and KFAK-peptide incubated at 37°C on day 1 (left column) and day 7 (right column). (A-B) 4Bpy and (C-D) KFAK-peptide.

2.3.2 AFM topography of samples incubated at 70°C

A temperature of 70°C was deliberately chosen to avoid degradation of the fibril on the one hand and to have clearly different thermal incubation conditions on the other hand. It was found that fibril formation was accelerated. The formation and deformation of the structures are illustrated in Figure 6 as a function of incubation time. The topography image obtained at 0 h in Figure 6 (0h) demonstrates that the vast majority of particles have a spherical or elliptical shape with a height ranging from 8 nm to 70 nm. After 2 h of incubation, nanofibrils with a height ranging from 6-15 nm were observed. These structures prevailed until 8 h of incubation as illustrated in Figure 6 (2h-8h). However, they vanish after 24 h of incubation. Instead, short fibrils (around 5nm) or even spherical-like structures with a height between 10-40 nm are observed. This suggests that the nanofibrils degraded in Figure 6 (24h). According to the results of incubation at 70°C, nanofibrils formed in less than 8 h, which is significantly faster than incubation at 37 °C, which takes four to seven days.

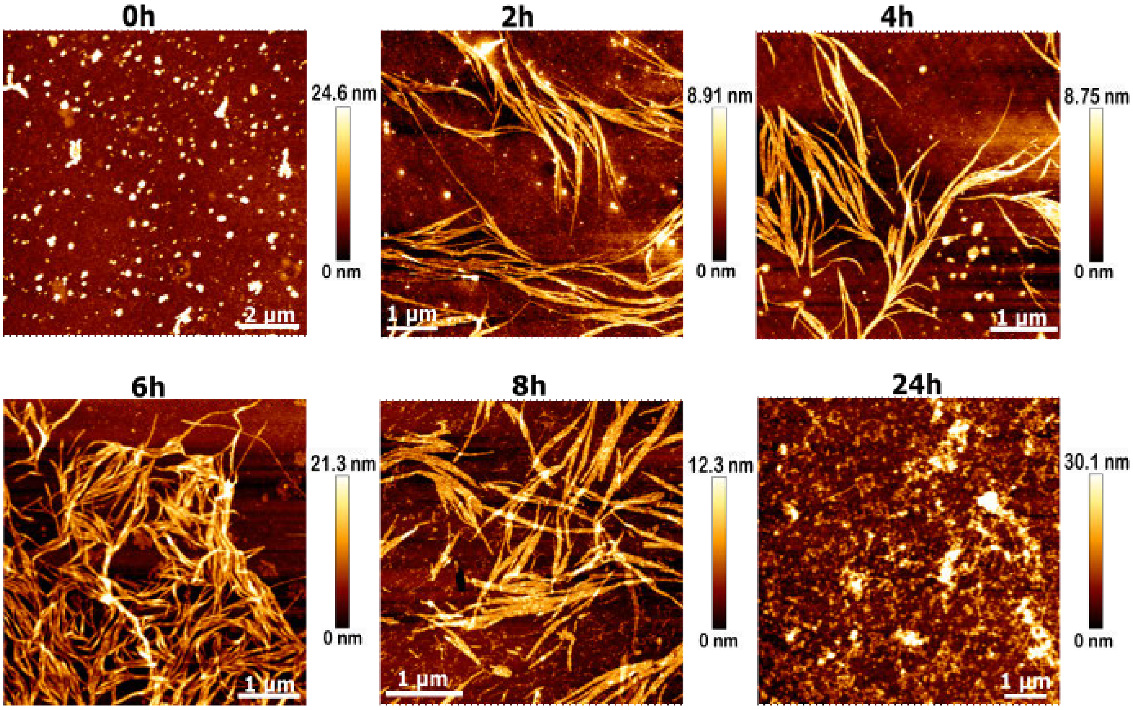

Figure 6. AFM topography of the KFAK peptide-4Bpy adduct incubated at 70°C for different time periods. 0–8 h and after 24 h.

A further incubation of pure KFAK-peptide, as well as 4Bpy, was carried out under the same conditions in order to confirm that the growth of nanofibrils was a result of the combination of both components. Figure 7 and Figure 8 show the topography images of the pure KFAK-peptide and the pure 4Bpy sample, respectively. Figure 7 clearly demonstrates that there is no indication of nanofibril formation and that the peptide shapes are globular or elliptical instead, following the incubation period. By using cross-section analysis, the height of the structure ranges between 5-13 nm on average. The same phenomenon can also be seen in Figure 8, where the majority of the 4Bpy particles are globular in shape with a height of 5-9 nm on average. Concluding, the formation of nanofibrils was initiated by interactions between 4Bpy and the KFAK-peptide.

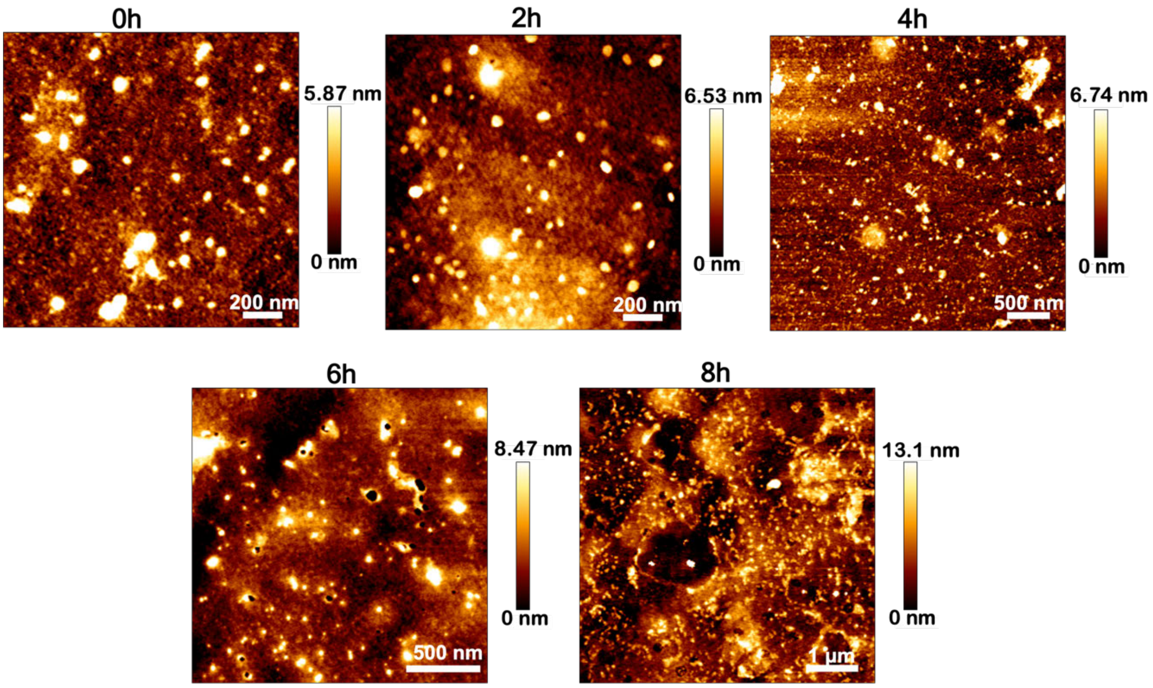
0h
5.87 nm
0 nm
200 nm
2h
6.53 nm
0 nm
200 nm
4h
6.74 nm
0 nm
500 nm
6h
8.47 nm
0 nm
500 nm
8h
13.1 nm
0 nm
1 µm

Figure 7. AFM topography of the pure KFAK-peptide incubated at 70°C for different time periods (0 h, 2 h, 4 h, 6 h, and 8 h).

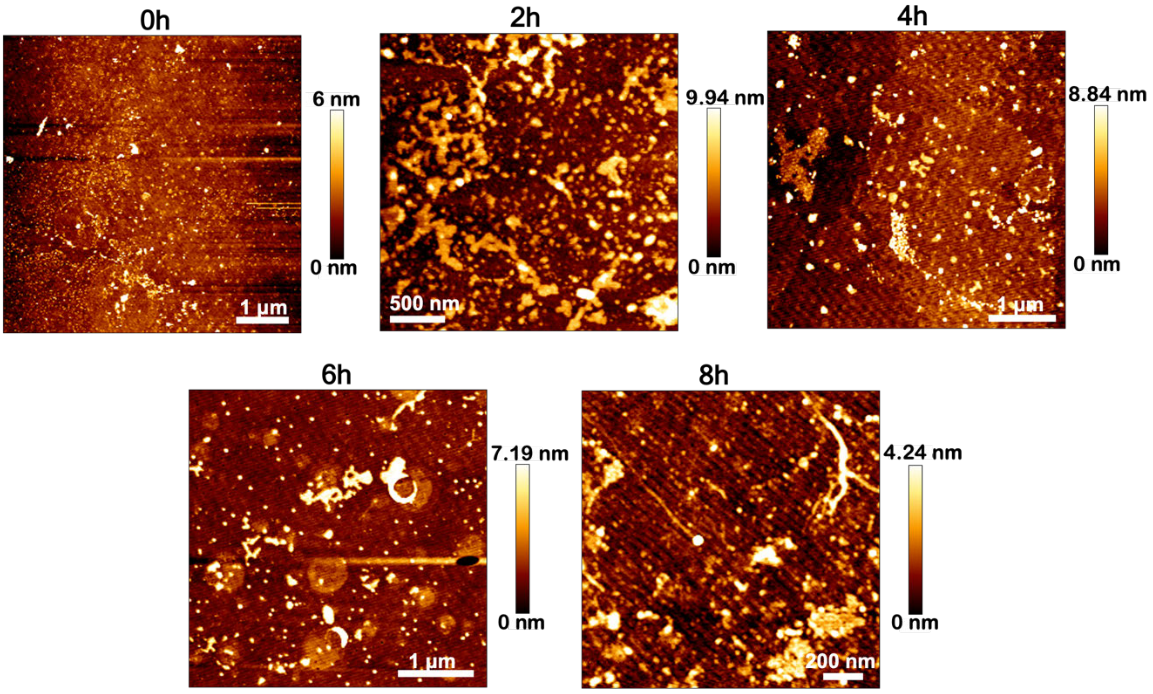
0h
6 nm
0 nm
1 µm
2h
9.94 nm
0 nm
500 nm
4h
8.84 nm
0 nm
1 µm
6h
7.19 nm
0 nm
1 µm
8h
4.24 nm
0 nm
200 nm

Figure 8. AFM topography of pure 4Bpy incubated at 70°C for different time periods (0 h, 2 h, 4 h, 6 h, and 8 h).

From all AFM topography images in Figures 4 and 6, it is evident that the length of the nanofibrils ranges from hundreds of nanometers to micrometers and is not homogeneous. First, based on the sequence of the KFAK-peptide, single peptides consist of 14 amino acids. Assuming the molecules are linearly stretched, the distance between amino acids can be determined by the length of the peptide bond, which is approximately 1.32 Å (0.13 nm) [127]. Second, the interaction distance of a 4Bpy molecule with the N-terminus or C-terminus of a peptide is calculated to be between 1.68 to 2.41 Å (0.16-0.24nm) [126]. Therefore, the totals length that can be expected after adding the length of a single molecule of 4Bpy to the length of a single KFAK-peptide (H_2N-KKKFAFAFAFAKKK-COOH) is approximately 2.06 nm. The length of this theoretically calculated single nanofibril structure is extremely lower when compared to the present result of nanofibrils (Figures 1 & 6). Therefore, it is reasonable to draw the conclusion that the nanofibrils that were observed in this experiment are not the result of a single peptide molecule but rather of multiple peptides that have bound together to form a longer structure by 4Bpy which results in a KFAK-4Bpy alternating structure in 2D and 3D stacking.

Even though it was not possible to achieve the 2D nanopatch structure as described by Liu *et. al.*, [126], which was anticipated would be promising for the direct sequencing utilizing TERS, it is still advantageous to carry on with the study. The nanofibril structure is suspected to be an open structure arranged in multiple layers, which is already challenging for the sequencing analysis. Nevertheless, retrieving additional information from nanofibrils using TERS would be still advantageous. First, TERS is employed to validate the AFM results regarding the involvement of the organic molecule 4Bpy in the formation of the nanofibril structure. Second, TERS is used to distinguish individual amino acids as well as the 4Bpy, which can still be beneficial information for future research on direct protein sequencing using TERS.

2.3.3 1st TERS experiment with 5nm step size

In the first approach, the TERS experiment aimed at the differentiation of the KFAKpeptid-4Bpy adduct on individual fibrils. Therefore, the step size between the measurement points was set to 5 nm. The AFM topography is shown in Figure 9A, where single nanofibrils are visible. Figure 9B shows a 3D image of the area given in Figure 9A. Figure 9C provides height information along the blue line in Figure 9B, which was determined to be 15 nm.

In the first step, conventional Raman spectra of the bulk KFAK-peptide and 4Bpy and the adduct were recorded. This way, the marker bands of the individual components can be assigned to distinguish them in the KFAK peptide-4Bpy adduct.

The spectra in Figure 9D show a strong Raman band at 1295 cm^{-1} in both the pure spectrum of 4Bpy and the spectrum of the adduct (KFAK-4Bpy), but not in the pure KFAK-peptide spectrum. Consequently, this band from 4Bpy can serve as a Raman marker band for 4Bpy. It can be assigned to the vibrational stretching of the two pyridyl rings in combination with the individual ring breathing modes [128]. It is evident that some bands were detected in the pure KFAK-peptide and in the adduct spectrum, but not in the spectrum of pure 4Bpy. These bands were used as Raman marker bands for the peptide. The omnipresent Raman bands 998 cm^{-1} and 1002 cm^{-1} are the characteristic ring breathing modes of 4Bpy and phenylalanine. Consequently, when assigning bands, it must be taken into consideration that additional Raman marker bands are required to accurately identify the adduct structure and prevent confusion.

The first TERS measurement was carried out by using a step size distance of 5 nm along the line indicated in Figure 9A. An acquisition time of 1 s was used for each spectrum and three consecutively selected spectra is presented in Figure 9E. Since the aim of this experiment was to determine whether or not the peptide and 4Bpy can be differentiated in the nanofibrils at all, this rather large step size between the measurement points was sufficient. In addition, TERS, as described in Chapter 1, has different selection rules and a high spatial resolution; hence, TERS band assignments cannot be completely correlated with conventional Raman spectra, and variation in the TERS spectra is expected (i.e., distinct band position and intensity). In order to rectify the situation, a combination of conventional Raman and TERS results was used as a reference for band assignment.

In the first TERS result, by comparing the TERS spectra and the Raman spectra in Figure 9D, it is evident that the marker bands from 4Bpy (highlighted in grey) were detected at 1298 cm^{-1} and 1503 cm^{-1}. The remaining bands for example at 1016-1034 cm^{-1} and 1127 cm^{-1} can be signed to amino acids phenylalanine, which is highlighted (blue), while bands at 1072 cm^{-1} and 910 cm^{-1} are from lysine (red), and bands at 774 cm^{-1} and 849 cm^{-1} can be assigned to alanine (green). Additionally, certain TERS spectral bands cannot be observed in conventional Raman spectra. For example, there are bands at 1127 cm^{-1} (phe), 910 cm^{-1} (lys), and at 774 cm^{-1} from alanine. These bands are typically weak in conventional Raman spectra [129], but they can be enhanced in TERS. And vice versa, for instance, phenylalanine bands at 836 cm^{-1} and around 1003 cm^{-1} are prominent in conventional Raman spectra but not in TERS spectra. This might be due to the TERS's selection rules, as mentioned previously. The Raman spectra were obtained from bulky samples, which indicates that it is an average of all different molecular vibrations within the laser spots. On the other hand, TERS is a method with a high spatial resolution that is sensitive to the orientation of the molecule. More details regarding the appearance and disappearance of certain Raman marker bands would be discussed in the second TERS results. Based on the findings of the initial TERS experiment, it is possible to draw the conclusion, that the result confirmed and added additional chemical information to the findings obtained from the AFM. The presence of Raman marker bands of both 4Bpy and KFAK-peptide confirmed that the nanofibrils were produced by binding of 4Bpy molecules to the KFAK-peptide.

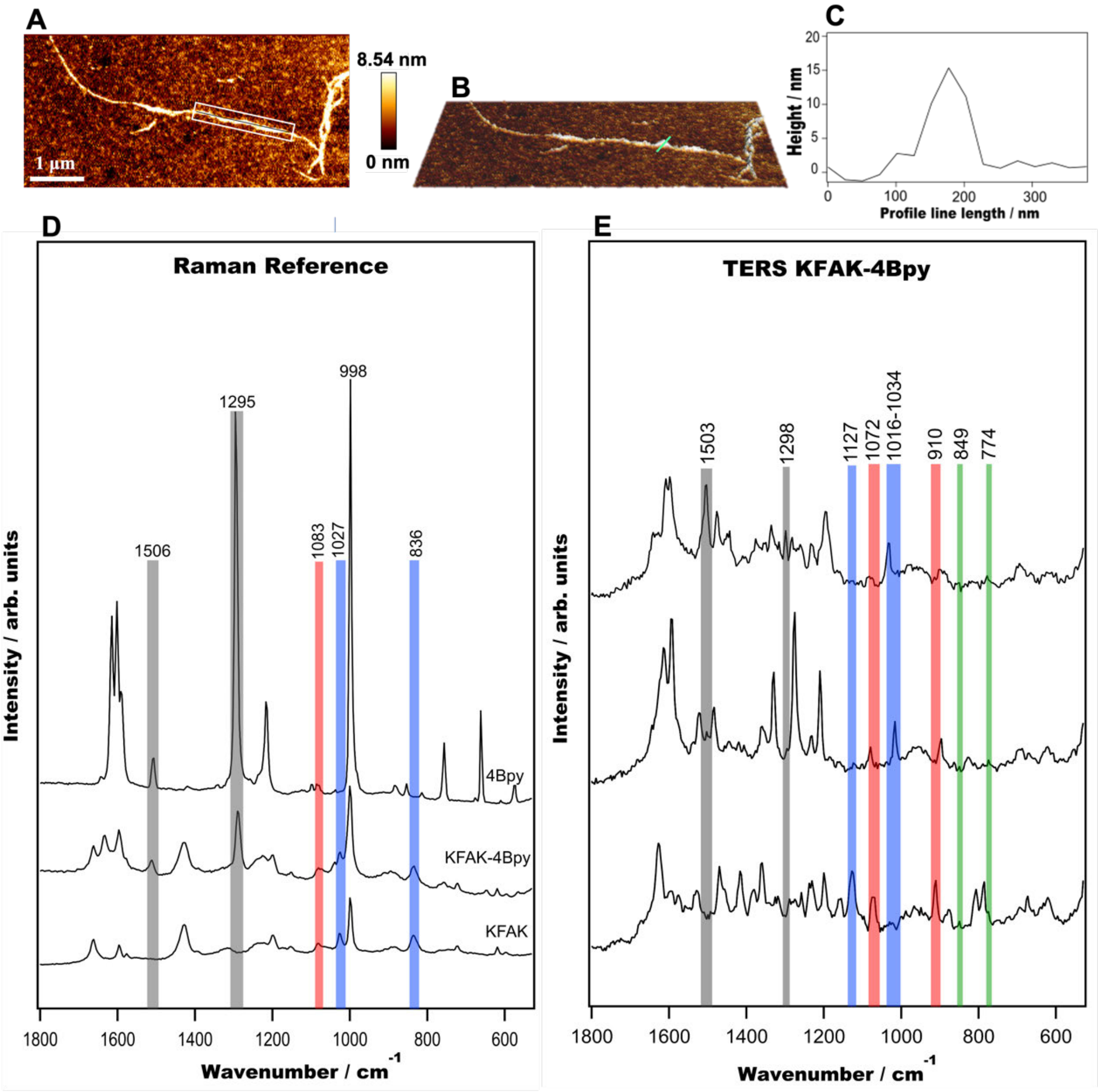

Figure 9. Selected TERS and standard Raman spectra of a KFAK peptide-4Bpy adduct. (A) AFM topography of individual nanofibrils from the adduct, (B-C) 3D image of the area in A, (C) profile line of a single fibril across the grey line in B. (D) Raman spectra of pure 4Bpy, the adduct of 4Bpy and KFAK-peptide, and KFAK-peptide (5-30 s acquisition time). (E) Selected TERS spectra from the area in A along the black line within the white rectangle in A; blue, red, and green bars indicate the marker bands of phenylalanine, lysine, and alanine respectively, and grey bars indicate the marker bands of 4Bpy. Spectra were acquired with a 1s acquisition time and a 5nm step size. All measurements used λ= 532 nm with ~500 µW laser power.

2.3.4 High-resolution TERS experiments with 0.5 nm step size

The primary objective of the second TERS experiment was the direct identification of the individual amino acids along a single filamentous structure. In order to distinguish individual amino acids, a 0.5 nm step-size was defined between measurement points. Apart from that, the same parameters as in the first experiment were used. First, a topography scan was carried out to select an appropriate stretched and thin area on the fibril. In Figure 10A, the AFM topography of the nanofibrils is given which is supplemented by a 3D image of the same sample area in Figure 10B. Finally, Figure 10C presents the corresponding profile lines indicated by lines 1 and 2 in Figure 10B with heights of 14 nm and 6 nm, respectively.

The TERS spectra were acquired on the main axis of the fibrils along lines d and e in Figure 10A. First, a total of 100 continuous spectra were collected, and eleven consecutively measured spectra that contained good signal-to-noise ratio enabling band assignments were selected in Figure 10D. Biomolecules (such as protein or amino acids) are typically weak Raman scatterers [102, 130]. In addition, in ambient conditions, a longer acquisition time and smaller step-size can cause thermal drift, which then affects the Raman signal, which may explain why only eleven spectra contain prominent Raman marker bands [81, 102]. A single peptide has the sequence of H_2N-KKKFAFAFAFAKKK-COOH, and like in the first TERS experiment, it is clearly possible to assign and differentiate lysine (K), phenylalanine (F), and alanine (A). These bands are highlighted in red, blue, and green, respectively. In addition, the bands from 4Bpy are highlighted grey, and the strong band from the silicon probe is highlighted yellow. The amino acids were assigned using at least two Raman marker bands. Phenylalanine (F) is designated by the spectral lines at 1003 cm^{-1} and 1034 cm^{-1}. Lysine (K) was assigned the bands at 1073 cm^{-1} and 1173 cm^{-1}, while alanine (A) was assigned the bands at 850 cm^{-1} and 925 cm^{-1}. However, it can be noticed that the Raman marker bands used to assign the spectra in this experiment differed from those used in the initial TERS experiments. This may be related to the TERS's selection rules (as previously mentioned), specifically with regard to the orientation of the molecule. For example, in the first TERS experiment, the Raman marker band at 1003 cm^{-1} from phenylalanine could not be observed, whereas, in this TERS result, it can sometimes be observed. It is also possible that the TERS probe acquired the signal at a location where no aromatic ring of phenylalanine was present.

According to the study that was carried out by Deckert-Gaudig *et. al.*, [131] the distinctive ring breathing mode was obscured in the AFM-TERS spectra of flatly adsorbed phenylalanine. This has to do with the orientation of the phenyl ring molecule with respect to the direction of the electric fields (E-fields). In a back-reflection TERS setup (which is also used in this experiment), the E-fields that are parallel to the z-axis of the tip will give a strong enhancement to the molecule in the same orientation, whereas the molecule perpendicular to the z-axis will receive a weak enhancement. Therefore, it is also possible to conclude that the molecular orientation of some phenyl rings in these nanofibrils was perpendicular and contributed to the obscuration of the marker band at approximately 1003 cm^{-1}.

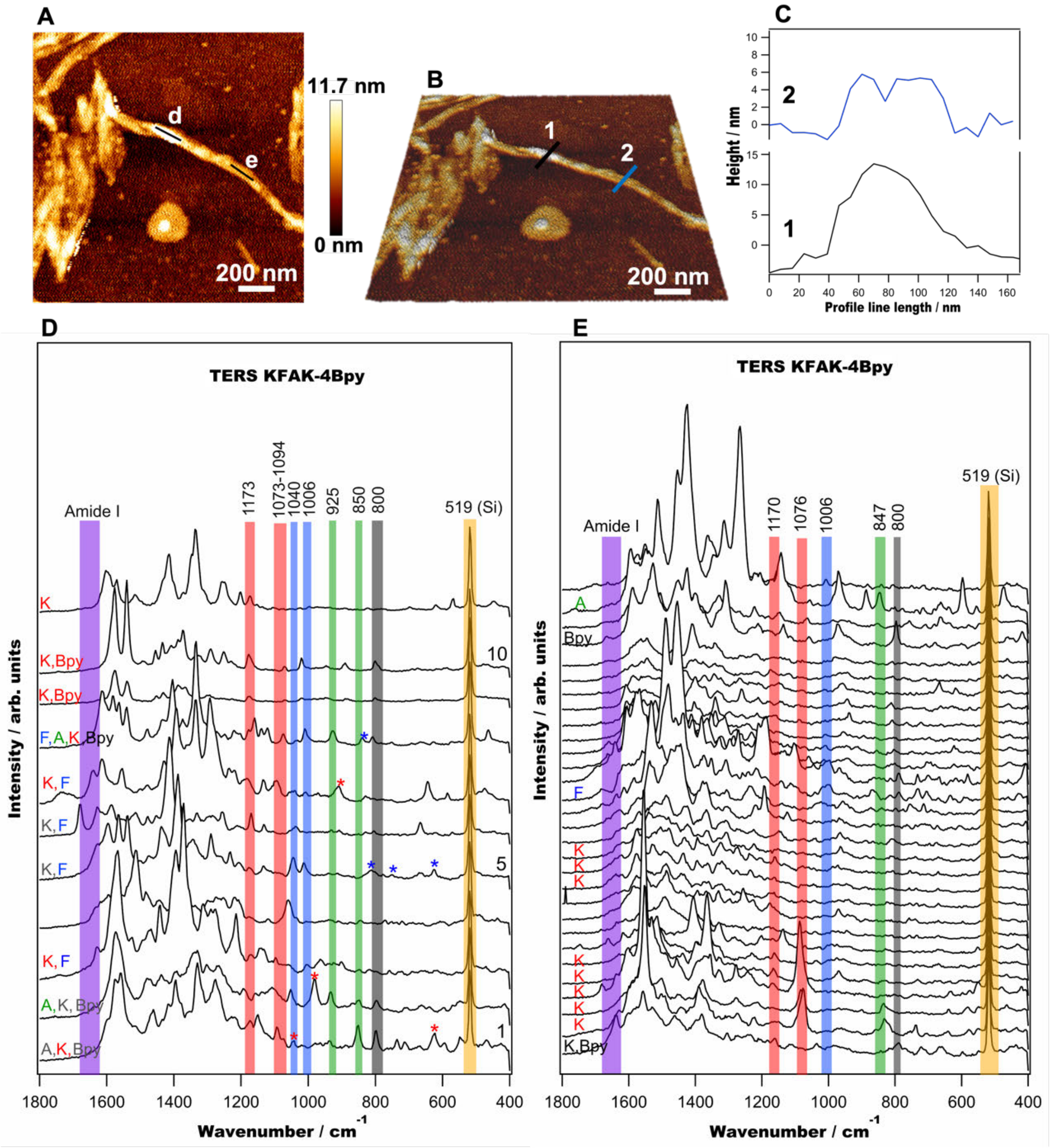

Figure 10. Selected TERS spectra of KFAK peptide-4BY adduct at successive measurement points separated by 0.5 nm. (A) AFM topography of the nanofibrils. (B, C) 3D image of Figure A and profile lines 1 and 2 across single filaments as indicated in B. (D, E) TERS spectra acquired along the lines d and e in Figure (A). Amide I bands are highlighted purple, lysine (K) red, phenylalanine (F) blue, alanine (A) green, and 4Bpy grey, the band marked yellow is from the silicon (Si) AFM tip. All the TERS measurements used λ= 532 nm with ~500 μW laser power and 1s acquisition time.

Most spectra contain bands originating from at least two different amino acids. For instance, spectrum no. 1 in Figure 10D contains bands from alanine and lysine and additional bands from 4Bpy. However, additional bands originating from lysine were observed, including bands marked with a red asterisk (*). As a result, it was determined that lysine (K) is the predominant amino acid in the spectra. This is illustrated by the fact that the letter K is colored, while the letters A and Bpy are grayed out. Similarly, the situation applies to other spectra. For instance, spectrum number 5 shows primarily phenylalanine (F) bands, including bands marked with a blue asterisk (*), with one from the lysine (K) band appearing at 1173 cm^{-1}; therefore, the letter F is colored. In addition, in Figure 10D (spectra no 3-7), it can also be assumed that the TERS tip was detecting the middle part of the nanofibril structure where the 4Bpy is away. This is demonstrated by the decreasing intensity of the 4Bpy Raman marker band (at 800 cm^{-1}) from spectrum no. 1 to spectrum no. 2, followed by the absence of the 4Bpy band from spectrum no. 3 to spectrum no 8.

It is noticeable that in the Figure 10D-E the Raman marker band used to assign 4Bpy is at 800 cm^{-1}. In contrast to the first TERS experiment (Figure 9), the assignment of 4Bpy was accomplished by the assignment the Raman marker bands at 1298 cm^{-1} and 1503 cm^{-1}, which could not be detected in the second results. On the basis of a previous study utilizing low-temperature ultrahigh-vacuum TERS to distinguish the configurations of 4Bpy molecules adsorbed on the Ag (111) surface, it was determined that three distinct molecular orientations of 4Bpy possessed a distinct Raman fingerprint [128]. For instance, the strong peak at 806 cm^{-1} can be associated with an out-of-plane vibration for a flat-lying adsorption configuration of 4Bpy [128, 132]. On the other hand, when the molecule has a different orientation, such as when it is standing upright on a surface, bands between 1298 cm^{-1} and 1301 cm^{-1} are expected. It is therefore reasonable to assume that the TERS probed different molecular orientations of 4Bpy in the first and second TERS experiments, resulting in the assignment of distinct Raman marker bands.

Interestingly, the 4Bpy band at 800 cm^{-1} was continuously present in the same spectrum as the lysine band (e.g., spectra no 1 and 10). This is in good agreement with the study that was conducted by Liu *et. al.,* [126], in which it was explained that the 4Bpy will interact with lysine (K) residues at the very ends of the peptide chains by leading to the formation of a 4Bpy-H_2N-KKKFAFAFAFAKKK-COOH-4Bpy structure. Since phenylalanine is bound to either alanine or lysine, it can also be observed that the phenylalanine bands appear in the same spectra as either lysine or alanine (for example, spectra no. 5 and no. 8). Since the nanofibrils in the experiment were multilayer with random molecular orientation rather than monolayer assemblies, it was only natural that more than one amino acid was detected simultaneously in each spectrum in the TERS experiments.

Figure 10E shows the spectra of a further TERS experiment recorded along line e in Figure 10A. Like in the previous experiments, the amino acids and 4Bpy could be distinguished by the same marker bands. First, the band at 1006 cm^{-1} was assigned to phenylalanine (F) marked blue, whereas bands at 1076 cm^{-1} and 1170 cm^{-1} were assigned to lysine (K) marked red, and bands at 847 cm^{-1} were assigned to alanine (A) which marked green. Moreover, the Raman marker band from 4Bpy is located at 800 cm^{-1}. Again, the 4Bpy is found in the same spectra as lysine (K). In contrast to Figure 10D, it is possible to observe that there are more selected spectra in Figure 10E. The selection of the spectra is always based on the spectra that show a high signal-to-noise ratio Raman marker bands. In Figure 10D, only eleven spectra from a 100-point TERS measurement demonstrate consecutively prominent Raman marker bands from amino acids as well as 4Bpy. Figure 10E, on the other hand, demonstrates that the prominent bands do not appear consecutively, and the Raman marker bands that originate from amino acids and 4Bpy are less apparent. In addition to that, certain spectra did not even have any Raman marker bands. Therefore, only 12 of the selected 30 spectra can be assigned to the amino acids and 4Bpy. Various plausible explanations emerge, including the fact that the orientation of the molecule at a particular location is not parallel to the z-axis of the tip, preventing the enhancement of the vibration mode. Another possible explanation is that the TERS tip's enhancement properties degraded after multiple measurements, which resulted in a weak signal as shown in Figure 10E. Lastly, as was previously explained, the biomolecule protein is not a strong Raman scatterer and by adding the possibility of tip degradation as well as a thermal drift to the explanation, these combination factors could also affect the spectral variation with respect to the band position and intensity [76, 81, 102].

In addition, Raman marker bands from the peptide backbone corresponding to Amide I were detected between 1638 cm^{-1} and 1680 cm^{-1} (marked purple). However, these bands were observed not in all spectra, which may be attributable to the heterogeneous multilayer structure of the nanofibrils, wherein some of the peptide bonds may be covered up by the organic molecule 4Bpy or amino acid residues, thereby obscuring the bands. In addition to peptide bond coverage and the possibility of peptide bond cleavage due to the plasmonic hot spot under the TERS tip, the absence of an Amide I band may also be associated with the orientation of the molecule in relation to the polarization of the excitation light [81].

This high-resolution TERS experiment not only demonstrated that three different amino acids could be distinguished from one another but also confirmed the theoretically predicted attachment of bipyridyl to lysine by Liu *et. al.,* [126]. This information can be utilized for future TERS-based direct protein sequencing experiments. In Table 1 all bands and assignments from the Raman and TERS experiments are summarized.

Table 1. Detected bands in the TERS spectra of the KFAK peptide-4BY adduct and tentative assignment.

Wavenumber (cm^{-1})	**Assignment**	**Reference**
519	Silicon	
622	**Lysine**	[129]
735		
907		
978		
1038		
1073		
1094		
1170-1173		
622	**Phenylalanine**	[129, 133]
750		
815		
840		
1003-1016		
1034-1041		
1611		
850	**Alanine**	[129]
925		
1020		
800	**Bipyridyl**	[128, 132]
659		
1298		
1503		
1638-1680	**Amide I**	[134, 135]

2.4 Chapter 2 Conclusion

Initially, the main objective of this study was an approach to direct peptide sequencing using TERS. The first step is to develop a method to unfold the 3D protein structure and stretch it into its primary form. After that, TERS was used to distinguish subnanoresolution amino acids. The organic molecule 4,4' bipyridyl (4Bpy) was introduced to the KFAK-peptide solution in order to address the first issue. This 4Bpy will bind to and interact with the amino acid at the N or C terminus of the peptide, causing the peptide to arrange in an open structure 2D nanosheet. However, the current results produce nanofibril structures rather than 2D nanosheet structures. AFM topography demonstrates the development of these nanofibril structures at two different temperatures. It requires 7 days of incubation to form the structure at 37°C. On the other hand, at a temperature of 70°C, the structure can form in as little as 2 hours of incubation time and disintegrate after 24 hours. AFM results also illustrated that the fibrils were formed with length ranges from hundreds of nanometers to micrometers and height of around 6-15 nm, also it is not homogeneous. The AFM results for pure KFAK-peptide and 4Bpy indicate that fibrils were formed due to the addition of the organic molecule 4Bpy. Although it was not possible to proceed with the direct sequencing experiment using TERS due to the unexpected formation of nanofibrils, continuing to analyze the nanofibril's structure using TERS still provides valuable information. The first TERS results with a 5nm step size validate the AFM findings that nanofibrils are formed by the introduction of 4Bpy, as indicated by the appearance of Raman maker bands from both the organic molecule 4Bpy at 1298cm^{-1} and 1503 cm^{-1} as well as bands from KFAK-peptide through amino acids Raman marker bands at 1016-1034 cm^{-1} and 1127 cm^{-1} (phenylalanine), at 1072 cm^{-1} and 910 cm^{-1} (lysine), and bands at 774 cm^{-1} and 849 cm^{-1} (alanine). The fibrils were then characterized using a 0.5 nm step size in the second TERS results. In addition to demonstrating that TERS can distinguish between three distinct amino acids (lysine, phenylalanine, and alanine) and 4Bpy, the results also confirm the theoretically predicted attachment of bipyridyl to lysine. These study's findings can all be utilized for future experiments, and another improved method must be proposed in the future to precisely stretch/unfold the protein structure in order to achieve direct protein sequencing analysis using TERS.

CHAPTER 3
RESULTS

The Disintegration of Insulin Amyloid Fibrils Monitored using Atomic Force Microscopy and Surface-Enhanced Raman Spectroscopy

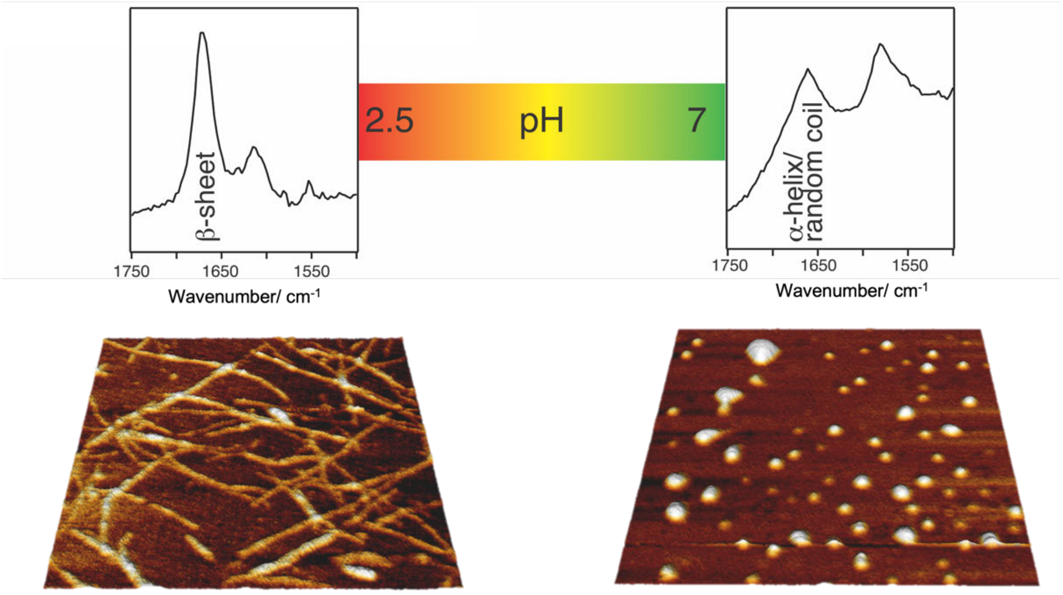

This chapter was modified from the *Journal Spectrochimica Acta Part A: Molecular and Biomolecular Spectroscopy,* Volume 256, DOI: https://doi.org/10.1016/j.saa.2021.119672, (2021), Erwan Yudiar Darussalam, Orsolya Peterfi, Tanja Deckert-Gaudig, Ludovic Roussille, Volker Deckert, pH-dependent disintegration of insulin amyloid fibrils monitored with atomic force microscopy and surface-enhanced Raman spectroscopy [135].

3.1 Introduction

Amyloid fibrils are a phenomenon where the native structure of the protein is misfolded into an ordered aggregate and it is associated with the development of various neurodegenerative diseases, such as Alzheimer's disease, Parkinson's disease, systematic amyloidosis, and diabetes type II. The aggregates have a polymorphic shape, ranging from nanometer-sized oligomers to intertwined filamentous micrometer-long structures [136-140]. Protein fibrillation has been shown to involve a delicate molecular equilibrium, with a hydrogen bond-based network generating the β-sheet core throughout the self-assembling process [141-144].

One acknowledged pathway of amyloid fibril formation is through a so-called nucleation growth mechanism. The native protein structure can be globular, partially folded or intrinsically unordered (unfolded state) [145, 146]. Generally, there are three major phases of protein fibrillation including aggregation (Figure 1). The process starts with the nucleation phase, where the native protein structure misfolds and assemblies into oligomeric species. In this stage, one or more higher-order oligomers can form a fibril nucleus, which can then assemble into amyloid fibrils by rapidly adding other monomers. In the elongation phase, preliminarily formed fibrils can split creating another coupling position where new monomers attach. This process continues until nearly all free monomers are added and transformed into a fibril structure. This phase runs exponentially (see blue line in Figure 1) and is followed by the stationary phase, where fibrils can attach to each other side-by-side or intertwine. In addition, interactions with other proteins or non-proteinaceous molecules from the environment may occur, possibly leading to the formation of amyloid plaques [146].

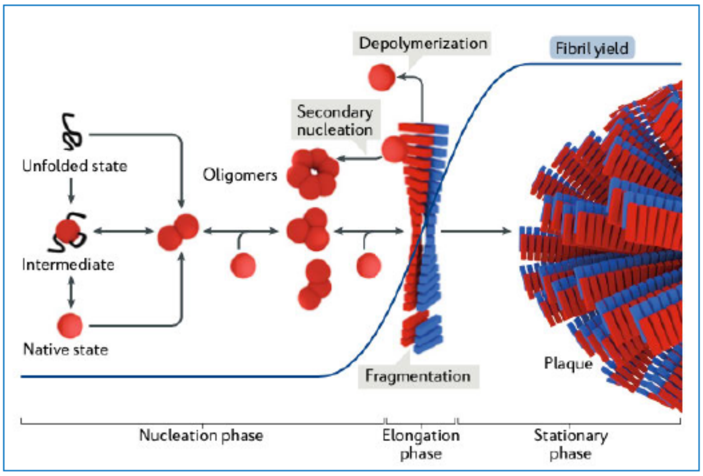

Figure 1. Mechanism of amyloid fibrillation which started with the nucleation phase transforms unfolded/intermediate/native state to oligomers structure, followed by the elongation phase, in which oligomers add up other monomers to form fibrils, and finally, the stationary phase, in which fibrils attach to each other and form amyloid plaques, adapted from the journal under permission [146].

Some researchers have investigated the molecular origins of fibril stability, and they revealed that electrostatic and van der Waals interactions, as well as π-π aromatic stacking, are involved. The kinetics reaction, as well as the molecular and morphological structures of intermediates and mature fibrils, are all affected by mechanical or chemical perturbations. Also, the supramolecular morphology of the fibril is controlled by interactions between peptide chains, which are unique to each protein. This challenges both the development of therapeutics as well as the establishment of a generally valid building process to disintegrate amyloidogenic aggregates.

Several studies have found that a number of factors can influence the properties of a peptide or protein, resulting in the aggregation or disaggregation of fibrils [136, 137, 139, 140, 147]. Protein sequence, pH value, molecule net charge, excipients, and interfaces are all chemically important. Whereas pressure, temperature, agitation, and lyophilization are all physical conditions that might affect the stability of peptides or proteins. Changing the pH of the growth solution is the simplest chemically induced fibrillation modification. Since distinct amino acids are prone to protonation (i.e., glu, his, arg, lys) or deamidation (i.e., asn, gln), working under acidic or basic environments alters not only the peptide/local protein's structure but also its net charge state. Electrostatic attractive/repulsive interactions between peptide chains change as a result of this. In the experiments, this can result in the aggregation process being accelerated or suppressed, resulting in the formation of morphologically distinct aggregates [147-153]. The ability to disturb the well-ordered structural network in mature fibrils can be exploited by introducing or removing protons [150, 151, 154, 155].

The behavior of insulin-mature fibrils at varied pH values ranging from 2.5-7 is the focus of this experiment. Only two previous studies, to my knowledge, have looked at the influence of pH variations on insulin amyloid fibrils, but there is no detailed information about molecular structural changes and morphology at the single-particle level [150, 155]. Insulin is a 51-amino-acid peptide with two chains (one with 21 residues and the other with 30 residues) linked by disulfide bridges. During fibrillation, the S-S bonds between the cysteine residues connecting two strands have been shown to remain intact [156], and the naturally predominant alpha-helical structure transforms into a highly organized beta-sheet-rich conformation. This significant conformational change is linked to the development of a number of intertwined filamentous structures.

The insulin fibrillation process, like that of other peptides and proteins, has been found to be highly susceptible to environmental factors [149, 157-160]. Individual species can be investigated in-situ with scanning probe microscopy to see how insulin changes morphologically during fibrillation. The height, length, elasticity/stiffness, and adherence of amyloid fibrils may be determined using atomic force microscopy (AFM) not only for dry samples but also in a liquid environment. This allows for direct observation of the dynamic aggregation process as well as visualization of morphological and mechanical features [58, 161-164].

To obtain chemical information, Raman spectroscopy, among other techniques, is well suited to describe amyloidogenic species not only in the bulk sample [165-168] but also at the single fibril level when applied in the near-field [110, 169-171]. Raman spectroscopy does not require any labelling that could interfere with the chemical structure of the probed sample, and the sample does not need to be specifically pre-treated. Surface-enhanced Raman scattering (SERS), in which the electromagnetic field is enhanced by surface plasmons in rough nanostructured surfaces, such as silver or gold when irradiated with the appropriate laser wavelength, overcomes the drawback of conventional Raman spectroscopy's low sensitivity in the visible range. The chemical characterization can be done all the way down to the single-molecule level because of this phenomenon. For example, see references [172-174] and more explanation in Chapter 1. This label-free method (e.g., conventional Raman spectroscopy) provides particular information about the chemical composition of the probed sample in addition to its great sensitivity. As a result, SERS has become a widely used technique in the surface and biological analysis [175, 176]. When applied to amyloid fibrils, the change of the peptide's native structure to a beta-sheet-rich conformation can be determined by analyzing the amide I band area, which reveals particular information about a peptide bond's environment. While Raman spectroscopy detects bands at 1640-1664 cm^{-1} for alpha-helix and random coil structures, bands at 1665-1679 cm^{-1} can be attributed to beta-sheet structures. [110, 169-171].

Insulin from the bovine pancreas was fibrillated at pH 2.5 in this work, and the resulting gel was suspended in pH 4–7 solutions. The degradation of mature fibrils to amorphous aggregates was visible in the AFM topography images of the dried samples. The disintegration of the well-ordered β-sheet structure in the fibrils to a conformation dominated by α-helix /unordered structures was confirmed by SERS experiments.

3.2 Experiments

3.2.1 Sample preparation

Bovine pancreatic insulin (Sigma-Aldrich, Germany) was dissolved (60 mg/mL) in HCl (pH 2.5) and heated at 70°C for 2.5 hours. After settling to room temperature, 10 µl of the fibrillar gel was resuspended in an aqueous solution (pH 2.5, 4, 5, 6, and 7), 1:100 (V/V) respectively. A 20 mM Tris (tris(hydroxymethyl)aminomethane) solution was used to modify pH values from 4 to 7. 10 µl of the solution was pipetted onto glass coverslips that had been cleaned with ethanol (Figure 2). The drop was gently removed from the glass surface with a pipette after 5 minutes of incubation and rinsed twice with the corresponding solution. For the AFM measurements in the dry state, the samples were dried at ambient temperature. The pH 2.5 sample was incubated, washed, and transferred to an AFM liquid cell for in situ AFM imaging in solution. AFM pictures were acquired immediately after 700 µl of a pH 4 solution was injected. Samples were treated as indicated below for the SERS studies.

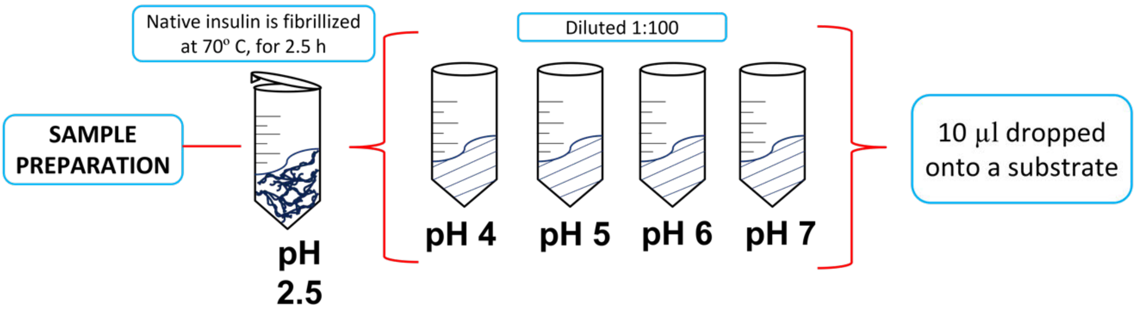
Native insulin is fibrillized at 70° C, for 2.5 h
SAMPLE PREPARATION
pH 2.5
Diluted 1:100
pH 4
pH 5
pH 6
pH 7
10 µl dropped onto a substrate

Figure 2. Sample preparation scheme

3.2.2 AFM Topography Measurements

A JPK NanoWizard I (Bruker-JPK BioAFM, Germany) AFM in intermittent contact mode was used to conduct the AFM measurements. Tap 190Al-G cantilevers from Budget Sensors, Bulgaria were utilized for dry-state measurements. Equipped with NSG10 (NT-MDT, Russia) cantilevers, liquid measurements were performed. Images at a resolution of 256 x 256 pixels were scanned at 1-10 µm. For each different pH condition, at least 10 different scan locations were examined. The same sample region was scanned continually for up to 80 minutes to observe the dynamic degradation process in liquid. By using a line-by-line polynomial fit approach, topography pictures' offsets were adjusted (JPK imaging processing software, Bruker-JPK, Germany).

3.2.3 SERS Measurements

Following the instructions from Leopold et al. as described in ref [177], a silver colloidal SERS substrate was prepared. A pre-cleaned glass slide, which was previously treated with HNO3/H2O2 (3:1) for 2.5 h and dried under argon was used to drop 10 µl silver colloid. On the silver nanoparticles, 10 µl of the same insulin fibril suspensions (pH 2.5, 4, 5, 6, 7; $c = 1.10^{-4}$ mol/L) used for AFM imaging (Figure 2) were drop-cast. The solution was gently sucked off after 5 minutes and the sample was washed with 10ml of the relevant solution. SERS spectra were obtained shortly after drying under argon. The microscope objective for the Raman system was 40x (NA 1.35). A power on the sample of 50 µW of 532 nm excitation laser light was applied. At tacq = 3-10 s with 6 acc., spectra were collected at 20–30 different locations of each sample. In order to improve visualization, all raw spectra were loaded into Igor-Pro 7.08 32-bit (Wave Metrics Inc. USA) and arranged with a y-offset. No additional data processing was performed.

3.3 Results and Discussion

3.3.1 AFM Topography Measurements in the Dried State

Insulin fibrils disintegrate in an aqueous suspension at pH > 8, creating amorphous aggregates/oligomers that can be observed with an AFM or a transmission electron microscope (TEM), according to two previous studies [150, 155]. Individual structures or the dynamics of the disintegration process were not explored in the reported data, which are exclusively for bulk samples. The morphology of disintegrating insulin structures following treatment with pH 4-7 solutions were initially studied using an AFM on dried samples in the studies. Following that, SERS experiments focusing on the specimen's secondary structure were carried out.

The long intertwined structures in Figure 3A, which were produced at pH 2.5, had a typical height of 5 nm and a length of several micrometers. The findings are in line with prior findings that demonstrate insulin favorably aggregates in low pH solutions and is extremely stable in their growth medium [110, 159, 165, 178, 179]. The shape of insulin fibrils became less distinct when suspended in a pH 4 solution, with structures that were typically shorter and thicker (height around 10-15 nm, see Figure 3B), indicating the beginning of disintegration. Despite the fact that the majority of the structures observed were filamentous, a few irregularly structured aggregates (height 17-25 nm) were discovered. The pH-dependent studies were expanded to include samples suspended in pH 5-7 solutions, and the AFM scanned topographies are given in Figure 3 C-E. The gradual degradation process is readily visible when the pH value of the medium increases to 5 and 6 (Figures 3C and D). The majority of the structures found at pH 5 were filamentous, similar to pH 4, whereas the appearance of pH 6 particles was already more comparable to the condition at pH 7.

Elongated structures were almost impossible to detect at pH 7, and the sample was dominated by more or less spherical particles with a height of 6-17 nm (see Figure 3E). The height variations of fibrils and disintegrating species are shown in Figure 3F by profile lines over selected places on the samples. To ensure that the process was homogeneous, each sample was examined in 10 different locations or scanning areas, three of which are depicted in Figure 4. It's worth noting that Tris(hydroxymethyl)aminomethane (Tris) was used instead of NaOH to adjust the pH. As a result, sample-tip interactions were better controlled in subsequent in-situ AFM experiments in the liquid (next sub-chapter) [180]. According to a previous study [155], the usage of Tris instead of NaOH did not affect the results.

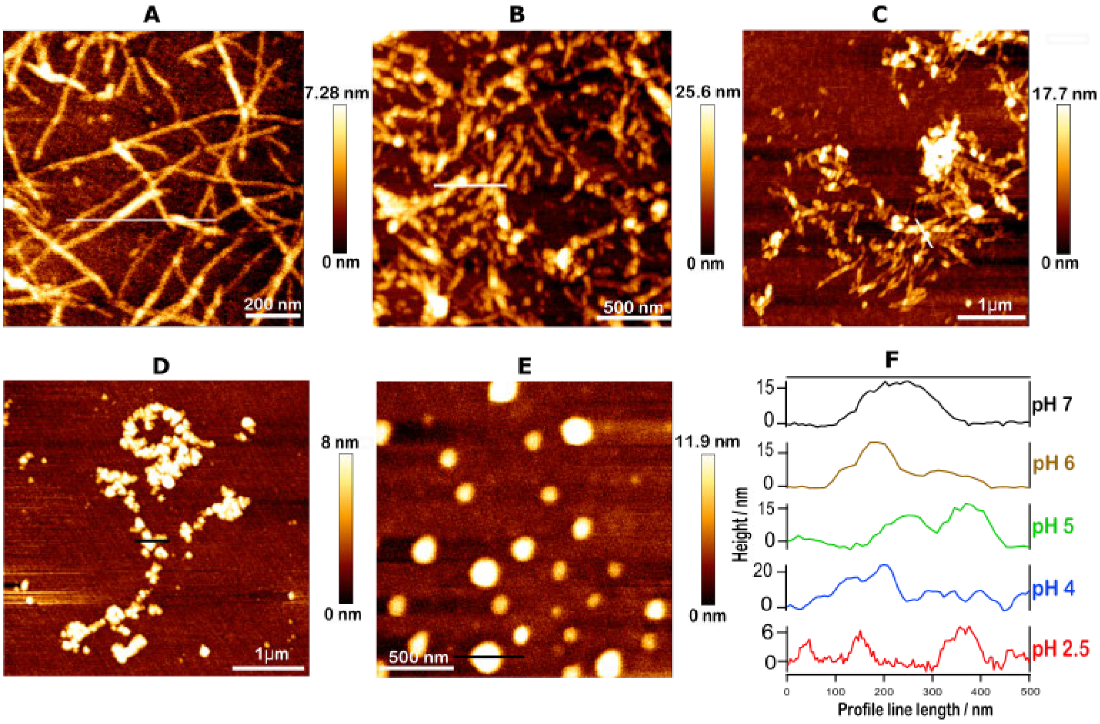

Figure 3. AFM topography of dried insulin aggregates. (A) Mature insulin fibrils grown at pH 2.5 (B) mature fibrils suspended in pH 4 (C) mature insulin fibrils suspended at pH 5, (D) mature insulin fibrils suspended at pH 6, (E) mature insulin fibrils suspended at pH 7, (F) profile lines across representative structures of the samples in (A)-(E). White and black lines, respectively, in (A)-(E) indicate measured profile lines. The images in (A)-(E) were offset-corrected applying a line-by-line polynomial fitting procedure.

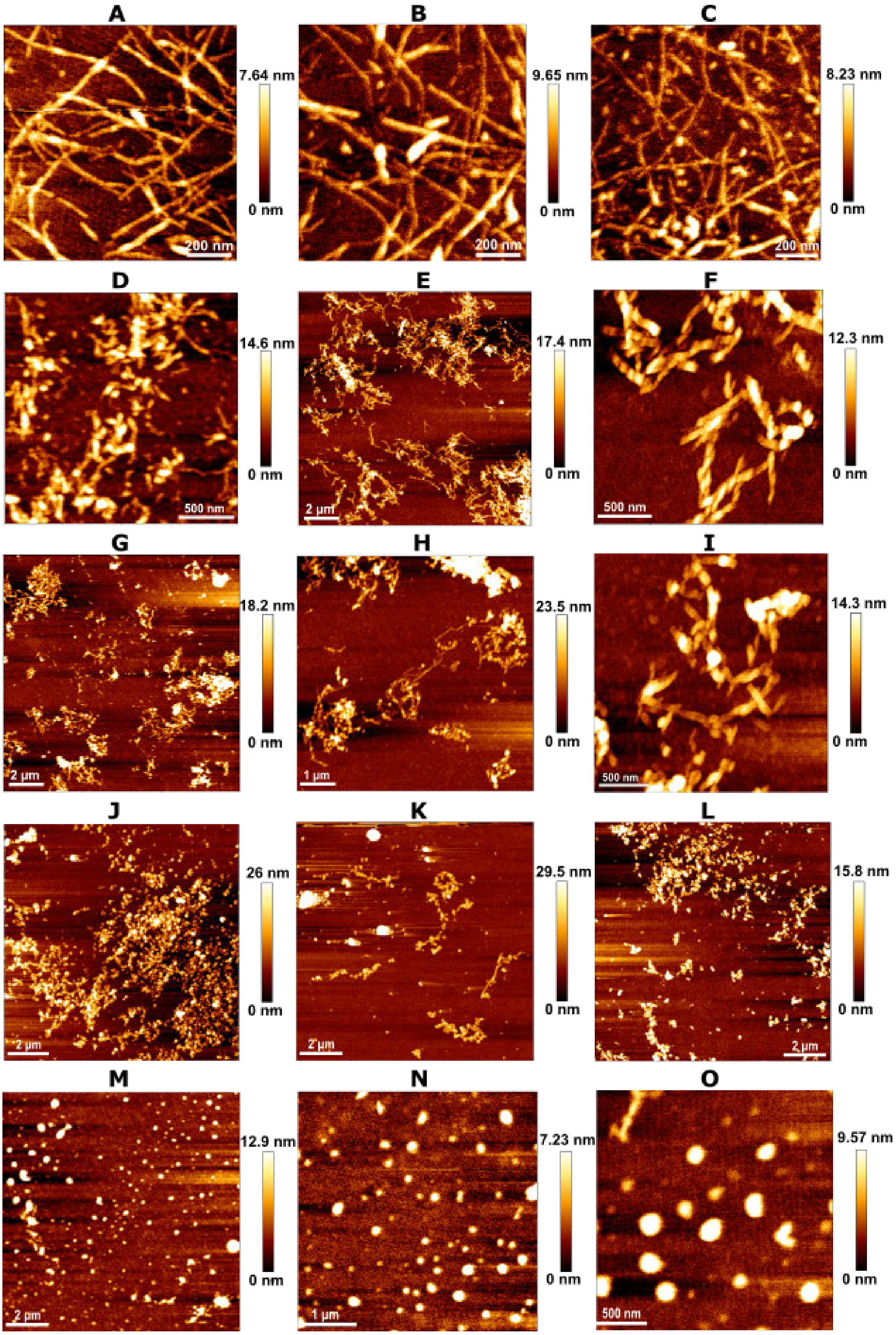
A
7.64 nm
0 nm
200 nm
B
9.65 nm
0 nm
200 nm
C
8.23 nm
0 nm
200 nm
D
14.6 nm
0 nm
500 nm
E
17.4 nm
0 nm
2 µm
F
12.3 nm
0 nm
500 nm
G
18.2 nm
0 nm
2 µm
H
23.5 nm
0 nm
1 µm
I
14.3 nm
0 nm
500 nm
J
26 nm
0 nm
2 µm
K
29.5 nm
0 nm
2 µm
L
15.8 nm
0 nm
2 µm
M
12.9 nm
0 nm
2 µm
N
7.23 nm
0 nm
1 µm
O
9.57 nm
0 nm
500 nm

Figure 4. AFM topography of dried insulin aggregates, measured on 3 different areas. (A-C) Mature insulin fibrils grown at pH 2.5, (D-F) mature fibrils suspended in pH 4, (G-I) mature insulin fibrils suspended at pH 5, (J-L) mature insulin fibrils suspended at pH 6, and (M-O) mature insulin fibrils suspended at pH 7.

3.3.2 AFM Topography Measurements in a Liquid Environment (pH 4)

In-situ AFM measurements were performed at pH 4 to gain a better understanding of the dynamic pH-dependent amyloid fibril disintegration process. The sample was transferred to a liquid AFM cell and studied immediately after suspending the fibrillar gel in a pH 4 solution. Figure 5 A-D shows four topography images of a repeatedly scanned area from a period of 34 min. The complete data set is available in Movie 1 along with two more datasets in the online Supplementary Material of the publication [135]. Datasets in Movies 2 and 3 in the Supplementary material therein illustrate the continual disintegration of mature fibrils following suspension in pH 4 solution, a part of which could also be seen in Figure 6.

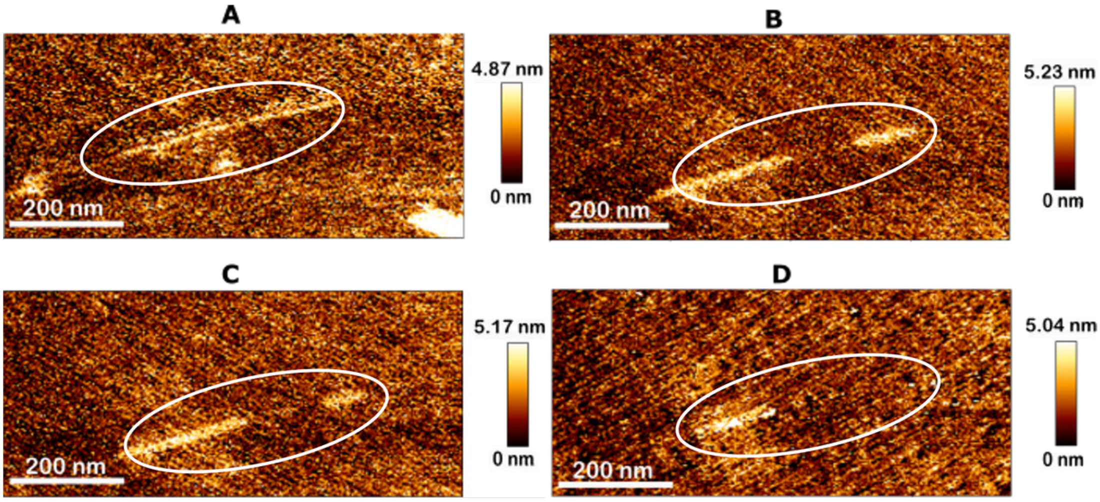

Figure 5. In situ monitoring of the disintegration of a mature insulin fibril at pH 4 with an AFM in liquid. (A) Topography image scanned immediately after suspending the fibrillar gel in pH 4 solution, (B) topography after 8 min, (C) topography after 12 min, (D) topography after 32 min. Scan rate 2.5 Hz, 256x256 px.

The fibril separated before the right end constantly shortened and eventually dissolved after 18 minutes, as seen in Figure 5. The left end of the fibril, on the other hand, showed similar behavior at first but eventually remained stable. More dynamic experiments revealed that not all fibrils were equally susceptible to pH changes across the time period studied. This correlates to the image in Figure 3B, in which filamentous structures dominate the general topography and unordered aggregates are only observed at a random position. According to prior research in this field [150, 155], soluble particles were generated instead of insoluble aggregates that separated from the glass surface during disintegration. At pH > 4, Shammas *et. al.* [155], found morphological alterations in fibril broadening and shortening, which confirms our findings in Figure 3B. In their investigations, however, filamentous structures were only seen dissolving above pH 8, with complete dissociation at pH 12. The fact that a partial disaggregation could be seen at pH 4 in the current studies is most likely to be attributed to the different sensitivity of the detection methods used. Shammas et al. evaluated the absorbance of the solution in order to quantify the concentration of soluble insulin produced.

In Figure 6, another AFM data set is presented. This time, the measurement lasted 80 minutes. To illustrate the degradation process, six AFM photos were chosen. The journal's supplementary material contains the entire data set (in movie format) [135]. The results support earlier findings by demonstrating a similar amyloid fibril disintegration process in which not all fibrils dissociate but rather some of them remain stable. The fibrils on the topographical images, however, are thicker in comparison to the prior image. This might be caused by AFM tip convolution [181]. Using the same tip for extended periods of time while scanning could wear it down. Consequently, a blunt AFM tip can cause the sample's AFM topography to become broader. In Figure 7 the effect of tip convolution is illustrated.

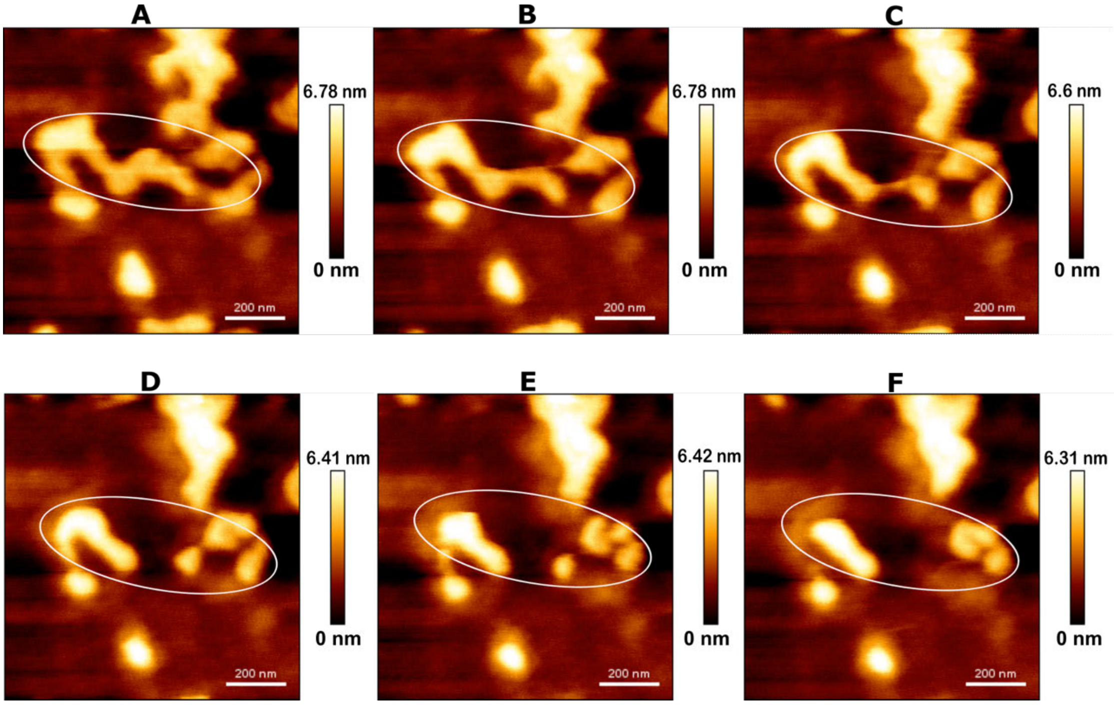

Figure 6. AFM topography of the disintegration of a mature insulin fibril in a liquid environment at pH 4. (A) After 8 min scanning, (B) 11 min, (C)14 min, (D) 17 min, (E) 20 min, and (F) 24 min. The disintegration process can be observed under the elliptical mark (white).

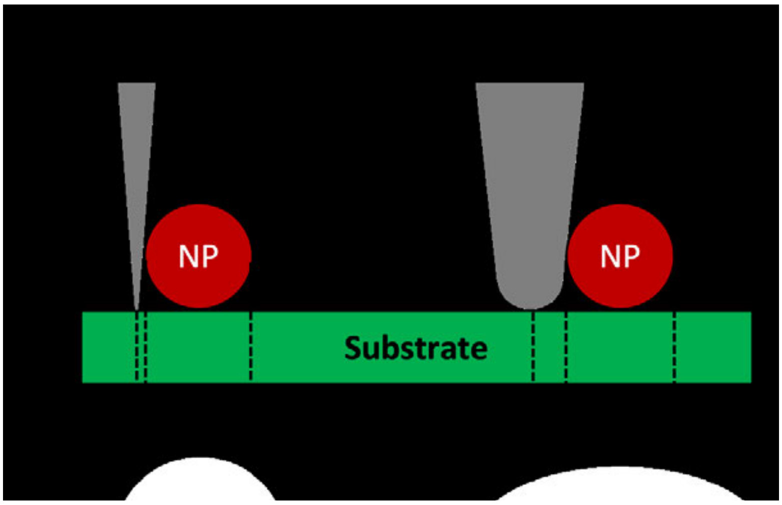

Figure 7. AFM tip convolution scheme demonstrating the distinction between sharp and blunt AFM tips, the latter of which can result in a wider AFM topography.

3.3.3 SERS Measurements (pH 2.5, 4, 7)

Infrared spectroscopy and the thioflavin T (ThT) binding assay were used in previous studies to detect the (partial) unfolding of the β-sheet structure in bulk samples [150, 155]. In the present study, SERS was employed to sensitively determine conformational changes. It can be assumed that the pH-dependent fibril dissociation is accompanied by a change in the secondary structure of the peptide.

In the beginning, the standard Raman technique was used to probe bulk samples of insulin fibrils produced at pH 2.5 (Figure 8A). Strong bands at 1670 cm^{-1} indicate the presence of a β-sheet secondary structure. After that, the SERS experiment was performed on other insulin fibrils produced at pH 2.5 which were obtained on silver colloids (see Figure 8B). Despite the fact that silver nanoparticles are susceptible to hydrochloric acid solutions, band positions are unaffected, as proven in a study of silver island films [182]. The spectrum information is limited to the surface of the probed particles because SERS is a surface-sensitive detection technique. As a result, the spectra are affected by the relative orientation of molecules directly interacting with the SERS substrate. Slight heterogeneities in band position, intensity, and width are frequently seen in the studies, and SERS spectra might differ significantly from far-field Raman spectra.

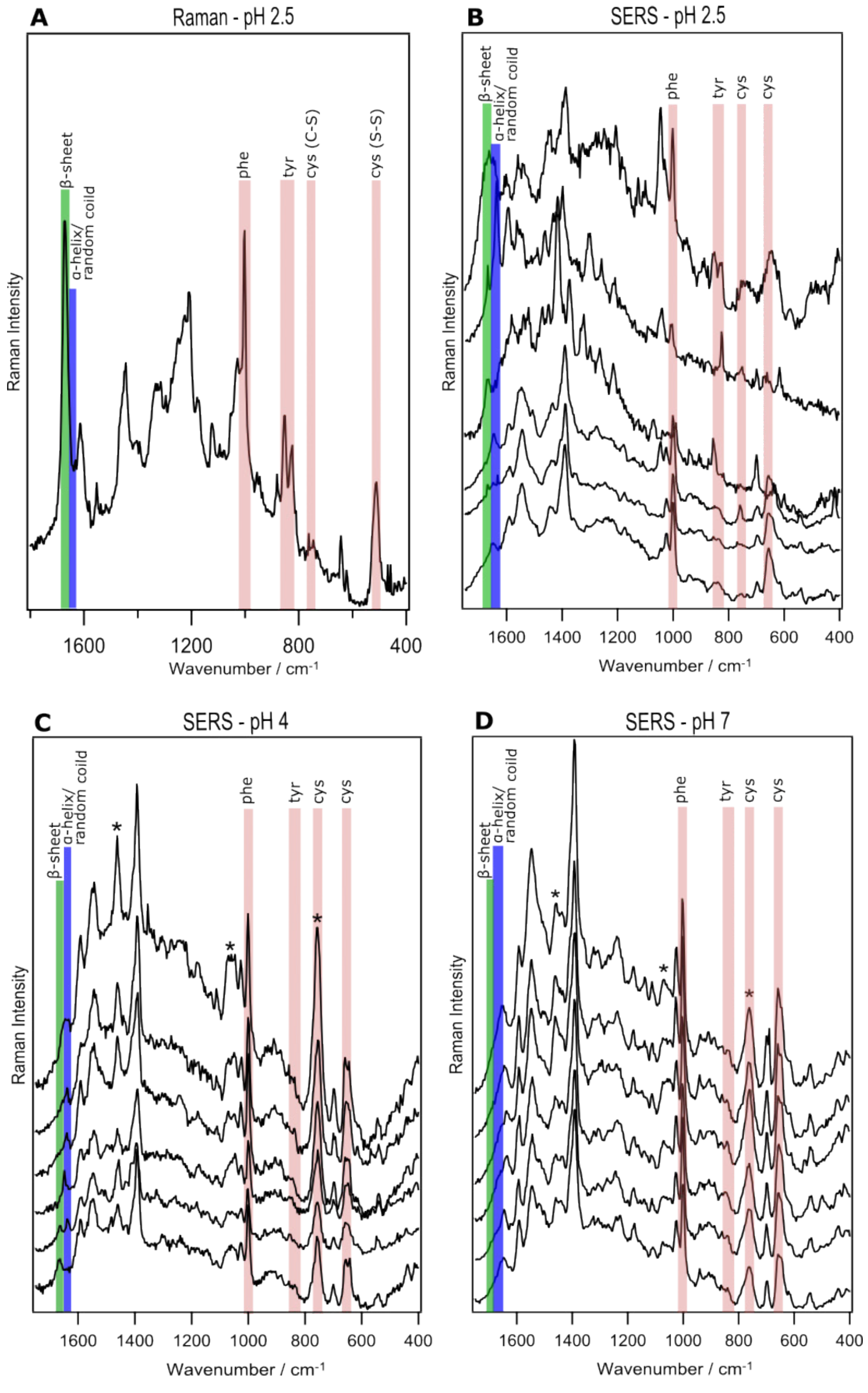

Figure 8. (A) Standard Raman spectrum of insulin fibrils grown in pH 2.5 solution. λ = 532 nm, t_{acq} = 60 s, P = 550 µW. (b-d) SERS spectra of dried insulin aggregates on silver colloids, (B) SERS spectra of insulin fibrils after suspension at pH 2.5, tacq = 3–10 s, 6 acc, P = 50 µW; (C) SERS spectra of insulin fibrils after suspension at pH 4, t = 5 s, 6 acc, P = 50 µW; (D) SERS spectra of insulin fibrils after suspension at pH 7, t = 5 s, 6 acc, P = 50 µW. Spectra in (B-D) were acquired in different areas on the samples. Amide I band regions indicating a-helix/unordered structures (blue) and b-sheet structures (green) are highlighted. The marked bands (*) might contain some additional contributions from Tris. For better visibility, the spectra are arranged with a y-offset.

The spectra in Figure 8B show intensity fluctuations and heterogeneity, although the distinctive bands of aromatic and nonaromatic side chains of amino acid residues can be identified at 998 cm^{-1} (phenylalanine, phe), 825, 856 cm^{-1} (tyrosine, tyr) [110], and 656, 759 cm^{-1} (cysteine, cys) [156, 166, 183]. A number of factors, including low surface concentration, molecule orientation in specific hotspots, thermally driven atomic reconstruction, and photophysical and photochemical processes, can cause SERS intensity fluctuations (SIFs) [184, 185]. Amide I band at 1668–1676 cm^{-1} (green bar) show β-sheet structure, which is commonly used as a marker band for amyloids [29]. Amide I bands are mostly contributed from the c=o stretching vibration mode (80%), and addition from C-N stretching (10%), and N-H bending vibration (10%) (Figure 9).

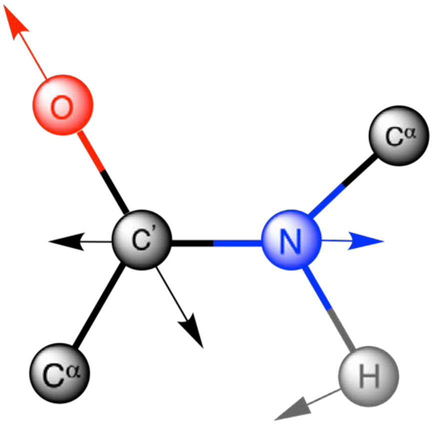

Figure 9. Molecular vibration mode of amide I. O = Oxygen (Red), C= Carbon (Black), N= Nitrogen (Blue), and H= Hydrogen (grey).

A contribution from a-helix/random coil structures can be seen in additional bands at 1634–1648 cm^{-1}. It was anticipated that mixed secondary structures would be detected, including a-helix/random coil and β-sheet, and the finding is consistent with the findings of near-field Raman studies [186, 187]. Because soluble components were eliminated during sample preparation, contributions from native insulin could be excluded.

The following SERS experiment was performed on an aliquot of mature insulin fibril suspension at pH 4 and pH 7, respectively. After incubation on the SERS substrate, samples were washed to eliminate the contribution of non-fibrillar insulin. In conventional Raman, the spectra were dominated by signals from Tris due to the low molar concentration of insulin, which obscured any insulin bands and provided no valuable information. Figures 8C and D show six of the 20 spectra obtained at various locations across the samples. When comparing the SERS spectra to the Raman spectrum in Figure 8A, it is clear that the band at 759 cm^{-1} attributed to cys is greatly enhanced in the SERS spectra. This can be explained by the silver substrate's strong affinity for sulfur in cysteine, as previously described [188]. The fact that no S-S modes were detected in Figure 8 B-D suggests that the disulfide bridges were broken by binding of the cys residue to the silver substrate via Ag-S bonds.

Low-intensity bands at 1664 cm^{-1} can be assigned to β-sheet structures in Figure 8C, while a band at 1639 cm^{-1} indicates α-helix/unordered structures in the majority of the spectra (green). This observation matches the partial disintegration of the intertwined fibril shape at pH 4 as measured by the AFM (Figures 3B, 4 (D-F), 5 & 6). The SERS spectrum in Figure 8D was recorded on the amorphous aggregates generated when mature insulin amyloid fibrils were treated with a pH 7 solution. Amide I bands were only identified around 1636–1652 cm^{-1} (green, α-helix/random coil) in these studies. No spectrum indicates the presence of β-sheet structures in this condition, which is consistent with the AFM results in Figures 3E and 4 (M-O), which show no more filamentous structures.

The protonation state of different amino acid residues, and hence the net charge of the peptide in amyloid fibril, are thought to have changed as pH increased. As a result, the hydrogen bond-based network and the overall fibrillar structure were destabilized. Previous pH-dependent amyloid disintegration experiments and modeling revealed that mainly the residues glutamic acid (glu), histidine (his) lysine (lys), arginine (arg), and tyrosine (tyr) were involved in this process [150, 154, 155, 189]. In a model peptide, the pKs of these amino acids were evaluated, and it was discovered that glu is partially deprotonated at pH 4 and fully deprotonated at pH 7 [190]. His is protonated at pH 4 and deprotonated at pH 7. Finally, up to high pH values, tyr (uncharged) lys and arg (protonated) remain unchanged. When applying these findings to present AFM and Raman data, it should be noted that the values are simply approximations because the model molecule has no significant hydrogen bonds. Thus, one of the driving mechanisms in the disintegration of the β-sheet secondary structure of insulin fibrils at pH 4–7 was postulated to be the deprotonation of glu and his residues. Indeed, near-field Raman spectroscopic results reported a high abundance of COOH groups (17%) on pH 2.5 insulin fibrils [187], which renders the aggregates prone to pH changes. Although tyr (27%) and NH_3^+ /NH_2^+ (19%) were also frequently present on insulin fibrils [187], they were most likely not implicated because the protonation state does not alter within the pH range investigated. The role of histidine did not seem to be decisive either, since it was hardly detected (<1%) [187] on the fibrils. Last but not least, it should be noted that the pH can also affect how peptides and solvents interact, which might lead to a disintegration [154].

3.4 Chapter 3 Conclusion

In this study, mature insulin fibrils were generated at pH 2.5 and suspended in solutions with a pH range of 4 to 7, after which the aggregates were examined using AFM and SERS. According to the topographical images, most of the observed structures at pH 4 were still filamentous, albeit with a greater height and shorter length. As the pH of the solution was elevated to 5 and 6, more disordered particles were observed, until no more fibrils could be identified at pH 7. With in-situ liquid AFM measurements at pH 4, the morphological gradual degradation could be observed time-dependently. Some fibrils disintegrated within minutes of being examined, while others remained intact. The amide I band was shifted from 1670 cm^{-1} for the pH 2.5 condition to 1638 cm^{-1} for the pH 7 condition in the corresponding SERS studies, which supported the gradual disintegration of the insulin fibrils' well-ordered β-sheet structure. Contributions of the β-sheet and α-helix/unordered conformation were concurrently found in the spectra of the samples suspended in pH 4 solution. After examining models that calculated the pKs values of particular amino acid residues in proteins, it was suggested that the alteration in the protonation state of the glutamic acid residue was a significant factor in the disintegration of the fibril backbone. The findings show that the well-ordered β-sheet structure of amyloid fibrils can disintegrate without the need for a specially formulated substance when the pH is changed.

CHAPTER 4
RESULTS

SARS-CoV-2 Characterization by Correlative Atomic Force - Fluorescence Microscopy and Tip-Enhanced Raman Spectroscopy (TERS)

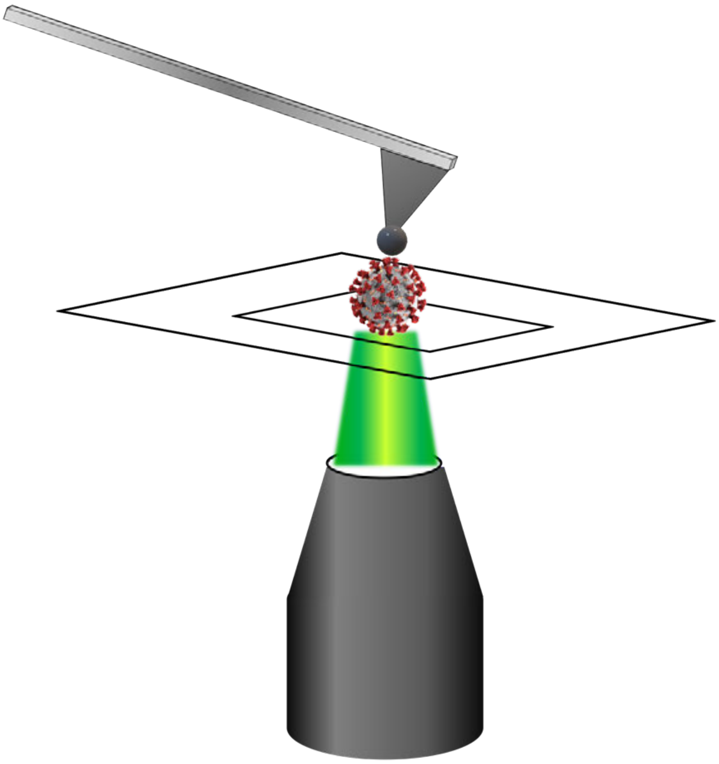

Manuscript in preparation

4.1 Introduction

Novel coronavirus disease-19 (COVID-19) is caused by severe acute respiratory syndrome coronavirus 2 (SARS-CoV-2), a highly pathogenic virus that causes severe respiratory infections [191]. Patients experience a variety of symptoms, including fever, coughing, shortness of breath, headache, muscle aches, and gastrointestinal symptoms. Pneumonia, pulmonary edema, acute respiratory distress syndrome (ARDS), and multiple organ failure are hallmarks of severe COVID-19 courses. Most patients have a mild course of the disease, but in some cases, such as the elderly with comorbidities, the infection can progress to a life-threatening condition [192].

SARS-CoV-2 was discovered in late 2019 in a cluster of pneumonia patients in Wuhan, China [193]. The virus has 79% sequence similarity to SARS-CoV, which originated in China and caused an epidemic in 2003 and belongs to the genus Sarbecovirus [194, 195]. As of September 5, 2022, there had been over 600 million confirmed cases of coronavirus disease 2019 (COVID-19), with over 6.4 million deaths worldwide (Figure 1) [196].

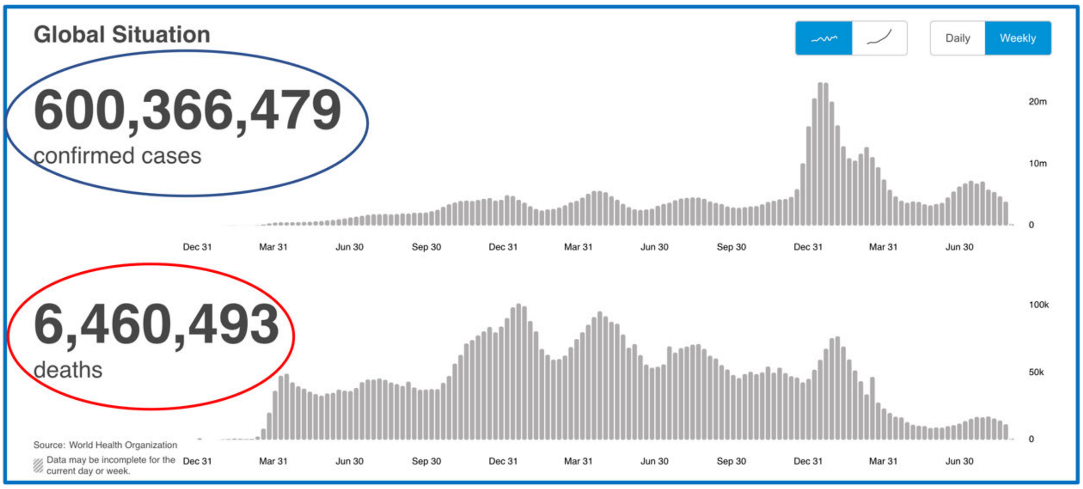

Source: World Health Organization

Data may be incomplete for the current day or week.

Figure 1. COVID-19 confirmed and death cases data statistics up to September 2022, (adapted from WHO [196], open access issued under the Creative Commons Attribution-Noncommercial-Share Alike 3.0 Intergovernmental Organization (CC BY-NC-SA 3.0 IGO) license, https://creativecommons.org/licenses/by-nc-sa/3.0/igo/).

The genetic material of SARS-CoV-2 is a single-stranded, positive-sense RNA between 26 and 32 kilobases in length. There are 24–27 viral proteins encoded by the genome, including four structural proteins and nonstructural proteins. These four structural proteins are the tiny envelope protein (E), nucleocapsid protein (N), matrix protein (M), and spike protein (S) (Figure 2) [197, 198]. In comparison to the other key structural proteins, the E protein is the tiniest one, yet it also has the greatest unanswered questions surrounding it. During the process of viral replication, there is a high level of E expression within the infected cell; yet, only a minute percentage of this protein gets incorporated into the virion envelope. The vast majority of the protein is found at the sites of intracellular trafficking, namely the endoplasmic reticulum (ER), the Golgi, and the ER-Golgi intermediate compartment (ERGIC), where it takes part in the assembly and budding of the coronavirus [199].

The N protein is the only protein that is responsible for the formation of the nucleocapsid, and its primary function is to attach to the RNA genome of the coronavirus. While the N protein does participate in activities that are associated with the viral genome, it is also important to the replication of viral RNA and the cellular response of the host to viral infection. In both the assembly process and the budding process, the endoplasmic reticulum localization of N protein serves a purpose. In addition, it has been demonstrated that the expression of the N protein dramatically promotes the formation of virus-like particles in certain coronaviruses [200].

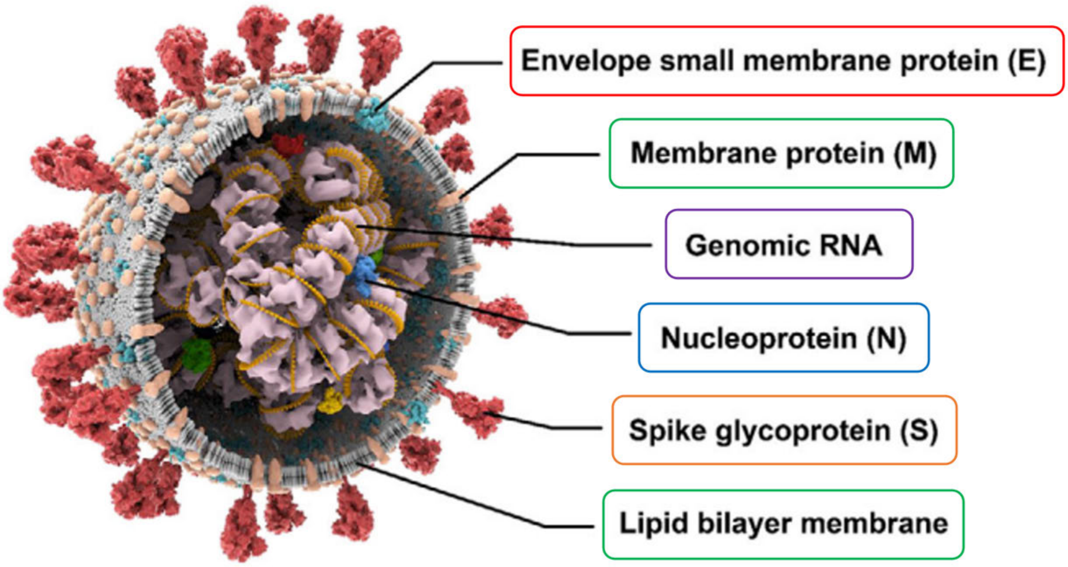

Figure 2. Schematic of SARS-CoV-2 structure (adapted from Bao *et al.* [201], open access article distributed under the Creative Commons CC-BY license terms, (https://creativecommons.org/licenses/by/4.0/).

The M protein of coronavirus plays a critical function in virus assembly by transforming cellular membranes into factories where virus and host components assemble to form new virus particles. The M proteins of SARS-CoV, SARS-CoV-2, MERS-CoV, MHV, FCoV, IBV, TGEV, and BCoV are localized near the Golgi apparatus. Reverse genetic studies and research on the assembly of virus-like proteins (VLP) reveal that the M protein promotes assembly by interacting with the viral ribonucleoprotein (RNP) and S glycoproteins at the budding site and by forming a network of M-M associations that is capable of excluding some host membrane proteins from the viral envelope [202].

The S glycoprotein is a type 1 membrane glycoprotein that has a variety of functional domains in close proximity to the amino (S1) and carboxy (S2) termini. The S1 subunit is located on the periphery and is involved with receptor-binding functions [203, 204]. In contrast, the S2 subunit is a transmembrane protein that is responsible for mediating the fusion of viral and cellular membranes. In a general sense, the S glycoprotein is responsible for facilitating the binding of the virus to susceptible cells, causing cell fusion, and inducing antibodies that are neutralizing. The S1 monoclonal antibody seems to arise most efficiently because it has a higher level of neutralizing activity than the S2 functional component, which also contains numerous antigenic sites [198, 205].

In clinical microbiological laboratories, molecular biology techniques are used to identify numerous pathogens (bacteria, fungi, and viruses), which in turn provide analytical platforms for the diagnosis of different pathogenic infections [206]. Several different molecular bio-tools, such as polymerase chain reaction (PCR), nucleic acid fractionation, molecular cloning, microarray, laser capture microdissection confocal microscopy, DNA sequencing, and blotting (both Southern and Western), have been successfully utilized as promising diagnostic tools for the diagnosis of a wide variety of pathogenic diseases [207, 208]. The use of PCR is now regarded as the most reliable method for detecting new emerging coronaviruses (SARS-CoV-2). However, these approaches have a number of limitations, including the fact that they are time-consuming, destructive, and need expensive reagents; as a result, their utility in characterizing the virus, including the extraction of topographic and chemical information, is limited.

Currently, the two most common techniques for visualizing virus structure are X-ray crystallography and electron microscopy (EM). X-ray crystallography can be used to acquire high-resolution information on viral proteins, macromolecular assemblies, and even complete viruses on occasion. However, the samples of interest need to be crystallized in order to employ this technique, which limits its application [209, 210]. In the study of SARS-CoV-2, room-temperature X-ray crystallography was utilized to investigate the viral main protease, which plays a fundamental role in the virus replication [211]. EM, on the other hand, has been widely used to study viruses since its invention in 1931 [212]. One of the most significant advantages of using electron microscopy (EM) to diagnose viral infections is that the technique does not require the use of organism-specific reagents to identify the pathogenic agent [213]. In addition to this, it is able to generate images rapidly and at a high resolution that is greater than one nanometer (0.1nm) [214].

In terms of the SARS-CoV-2 analysis, cryo-electron microscopy was used to characterize the virus's morphological structure, which demonstrated that the virus particles are generally spherical or fairly pleiomorphic and that they have a diameter that ranges from 84 to 126 nm, with an average of 108 nm (Figure 3 A & B) [46]. The SARS-CoV-2 is also clearly visible under the colorized transmission electron microscope (TEM) (Figure 3 C & D)[215]. Despite its benefits, the method has some drawbacks, such as the need to image samples in a vacuum to prevent electron beam scattering, making it impossible to study the dynamics of biological processes in living specimens [209]. Also, samples with low viral particle concentrations ($<10^5$ L^{-1}) may result in low EM sensitivity [214].

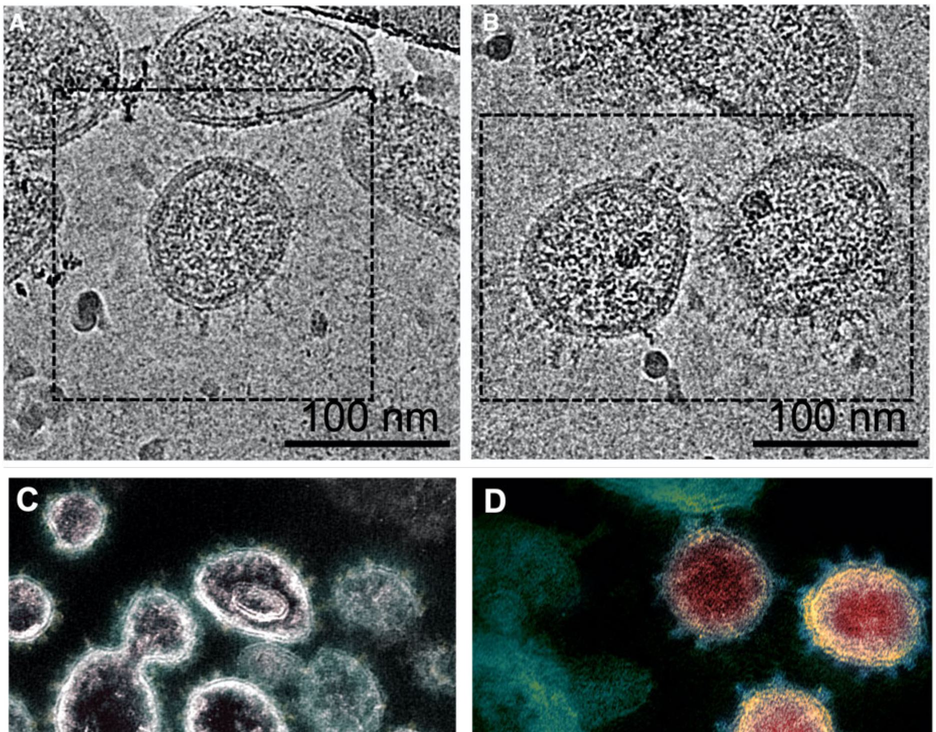

Figure 3. Electron microscope image of SARS-CoV-2. (A & B) Viruses were imaged with a cryo-electron microscope (adapted from Liu *et. al* [46], open access articles distributed under the terms of the Creative Commons CC-BY license, https://creativecommons.org/licenses/by/4.0/). (C & D) Viruses were imaged and colorized with the transmission electron microscope (adapted from images of 'Novel Coronavirus SARS-CoV-2', published by NIAID [215] and licensed under CC BY 2.0). To view a copy of this license, visit https://creativecommons.org/licenses/by/2.0/

Atomic force microscopy (AFM) is another imaging technology that allows nanoscale imaging of the morphology of biological samples in their native liquid environment. AFM does not necessarily require sample fixation, coating, or staining, which allows scanning of native and inactivated hydrated viral particles at high resolution and in three-dimension without further sample preparation [216, 217]. A more detailed explanation of the AFM technique is presented in Chapter 1. Therefore, this technique is suitable for acquiring SARS-CoV-2 topographic information. In order to obtain the chemical information, however, further techniques are required. Vibrational spectroscopies, such as Raman spectroscopy (RS), are emerging as potentially useful alternatives in the field of molecular diagnostics. It is possible to identify target molecules in a specific manner without destructing using a noncontact measuring method, requiring only a short amount of detection time and little to no sample pretreatment [218, 219]. Tip-Enhanced Raman scattering (TERS), on the other hand, is an advanced method from traditional Raman that can produce not only high-resolution images but also enhanced Raman signals, which can be used to obtain information from the surface of the virus. The method was explained in more detail in Chapter 1, Raman and TERS subchapter.

In this study, SARS-CoV-2 was investigated using a variety of techniques, including atomic force microscopy (AFM), fluorescence microscopy, and tip-enhanced Raman scattering (TERS). First, AFM was used to acquire topographical data from SARS-CoV-2, which was subsequently confirmed using fluorescence microscopy. Fluorescence microscopy is a reliable technique that is widely employed in almost every field of biology, including virology. Importantly, due to antibody staining or genetically encoded tags, its sensitivity (down to single molecules) and specificity are extraordinarily high. Fluorescence microscopy's ability to work with living cells, which enables the study of structures and processes in real-time, is another significant advantage [220]. Following the AFM-fluorescence correlation study, the TERS technique is applied to the surface of the virus in order to extract chemical information.

4.2 Experiments

4.2.1 Sample Preparation

a. Virus Propagation and Characterization

The SARS-CoV-2 subtype with ethics permission number 2018-1263, SARS-CoV-2/hu/Germany/Jena-vi005587/2020 was isolated from respiratory samples of patients at the Jena University Hospital and titrated using a standard plaque assay as originally explained [192]. The viral strain was produced and disseminated in Vero-76 cell cultures in DMEM (Dulbecco's modified Eagle's medium) (Sigma-Aldrich, Taufkirchen, Germany) supplemented with 10% fetal bovine serum (FBS) (PAN-Biotech, Aidenbach, Germany) and 1% Penicillin/Streptomycin (Biozym, Oldendorf, Germany). Under the obtainable accession number MW633323, the determined sequence is accessible in the NCBI Genbank.

b. SARS-CoV-2 Inactivation

Inactivation using UV-C radiation and paraformaldehyde (PFA) was employed to study SARS-CoV-2 in facilities outside of BSL-3 (Biosafety Level-3). To begin, supernatants were placed under a UV-C lamp (sterileAir AG, Weinfelden, Switzerland) according to the manufacturer's recommendations for 30 minutes to inactivate the virus-containing stock samples. Vero-76 cells were infected with UV-C-treated supernatants and the corresponding control stock solution to determine effective inactivation. Cells were observed under a light microscope 48 hours after infection, and any potential CPE (cytopathic effect) induced by virus particles that were still active was examined. The cells were then treated with WST-1 (4-[3-(4-(4-Iodophenyl)-2-(4-nitro-phenyl)-2H-5-tetrazolio] 1,3-Benzene Sulfonate) (Roche, Basel, Switzerland) at 37 °C for two hours with 5% CO_2. WST-1 is a stable tetrazolium salt that, when combined with NADH, produces the dye formazan [221]. As a result, it is a reliable tool for quantifying cell viability by measuring the resulting formazan levels with the Tecan SPECTRAfluor (Tecan, Männedorf, Switzerland) at an optical density of 492 nm (reference filter 620 nm). When compared to the active virus stock, cells treated with the inactivated virus stock had no CPE and the same viability values as the corresponding untreated cell control.

As an established method of chemical inactivation, virus stocks were diluted 1:5 in distilled water with 4% PFA and incubated for 30 minutes at 37 °C with 5% CO_2 [222]. To remove medium-containing phenol red and salts, 100 µl of inactivated supernatants were washed twice with distilled water before being resuspended in 100 µl of distilled water.

4.2.2 AFM Topography Measurements

AFM measurements were performed directly on inactivated virus samples obtained from Jena University Hospital. A viral sample of 10 µL was immobilized directly onto a glass substrate for 20 minutes, washed twice with 10 µL of distilled water and dried with argon. This glass substrate had been cleaned with nitric acid and hydrogen peroxide (HNO3/H2O2) solution (3:1) and then treated for 30 minutes with 50µL poly-L-lysine (0.1% w/v), washed twice with 50µL distilled water, and dried with argon before use. AFM imaging was carried out in intermittent contact mode in ambient conditions. For AFM imaging, a Tap190 Al-G tip from Budget Sensors, Bulgaria with a resonance frequency of about 160 kHz and a spring constant of 48 N/m was used. Images with a resolution of 256x256 pixels were obtained. Topography images were offset corrected by applying a line-by-line polynomial fit procedure or a plane correction (JPK imaging processing software, Bruker-JPK, Germany).

4.2.3 AFM-Fluorescence Correlation Measurements

A schematic representation of the overall AFM-fluorescence correlation study can be illustrated in Figure 4. Initially, AFM measurements were performed on the special glass substrate with fiducial markers, which was previously treated with poly-L-lysine (same as the previous standard AFM experiment). Prior to immunolabeling and fluorescence imaging of the sample, AFM images of the viruses on specific grid numbers or letters were acquired and documented.

In the next step, the same slides were used to stain the immobilized virus particles with immunofluorescence by incubating them in 5 % Bovine Serum Albumin (BSA) for 30 min at room temperature. Then, the slides were treated with a specific mouse SARS-CoV-2 spike antibody (1A9) (GeneTex; Irvine, USA, Cat#GTX632604 1:500 diluted in distilled water for 90 minutes. After 2 washing steps with distilled water, slides were further incubated in Alexa Fluor® 488 AffiniPure Goat Anti-Mouse IgG (H+L) (Jackson Immuno Research Labs, West Grove, Cat#115-545-146 1:1000 in distilled water for 1 hour. After another two washing steps, slides were used for the microscopical analysis.

For fluorescence microscopy imaging, a 488 nm laser with a power of 25µW was used to excite the dye molecule. An optical microscope (Zeiss LSM 980) with an objective oil lens (Plan-Apochromat 63x/1.4 NA) was used. To achieve a correlation of AFM-fluorescence data, the same sample areas were investigated on the same specific grid numbers and letters (locations) as AFM images (red square on the glass substrate in Figure 4). Images were processed (colorized, contrast adjustment, and image overlay) using ImageJ (Fiji) software [223]. After that, the sample was remeasured with AFM.

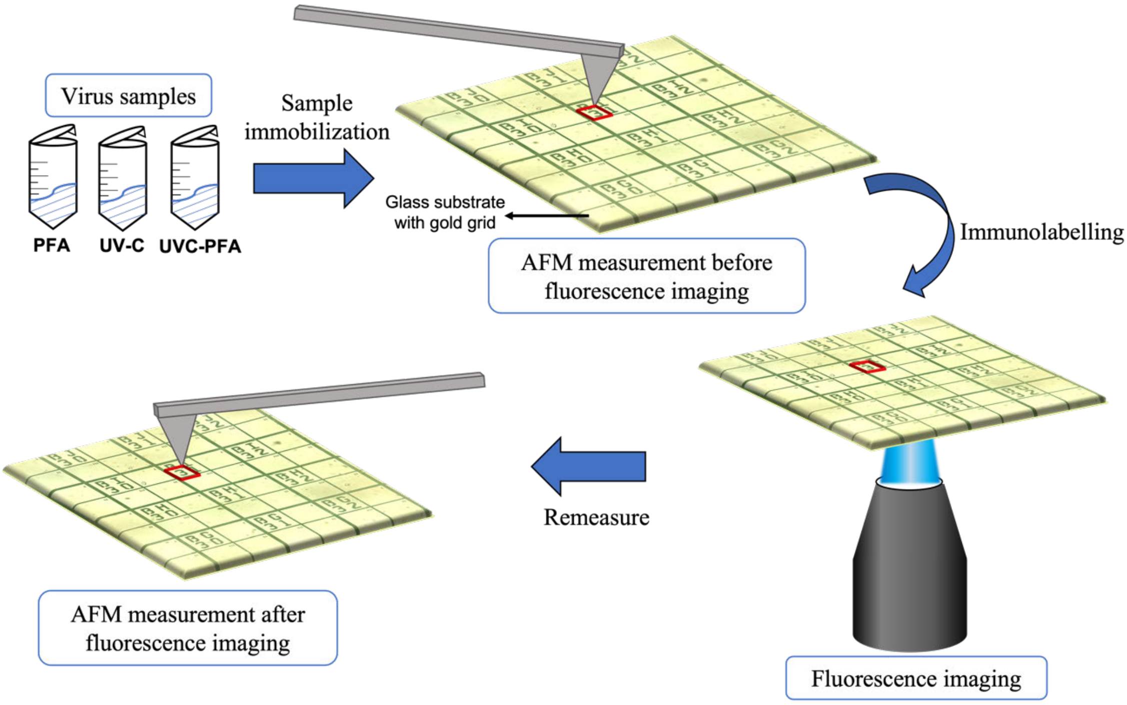
Virus samples
PFA
UV-C
UVC-PFA
Sample immobilization
Glass substrate with gold grid
AFM measurement before fluorescence imaging
Immunolabelling
Fluorescence imaging
Remeasure
AFM measurement after fluorescence imaging

Figure 4. Scheme of the AFM-fluorescence correlation measurements

4.2.4 TERS Measurements

TERS measurements were performed using a transmission setup with back-scattering geometry. The TERS setup included a Raman spectroscope connected to an AFM (Nano Wizard, JPK Instrument AG). The glass slide containing the adsorbed virions was placed in the sample holder and illuminated from below. The excitation laser was focused on the sample and the AFM tip using an oil immersion objective with a magnification of 60x (Olympus, NA 1.45). Traditional AFM probes (TAP 190 Al-G, resonance frequency: 160 kHz) for intermittent mode, were coated with 25 nm silver and stored in an argon atmosphere until used as TERS tips. For excitation, a laser with a wavelength of 532 nm and a power of 550 µW on the sample was used and was coupled to the inverse microscope (Olympus). A closed-loop XY piezo scanning stage was used to scan the samples. After scanning the virus surface, distinct measurement points in terms of a grid (10 x 10) were selected. The tip and sample were irradiated with the laser, and TERS spectra were recorded point-wise with an acquisition time of 1s. The direction of the tip on the TERS grid can be illustrated in Figure 5. For better visualization, all raw spectra were imported into Igor-Pro 7.08 32-bit (WaveMetrics Inc. USA) and arranged with a y-offset. There was no further data processing.

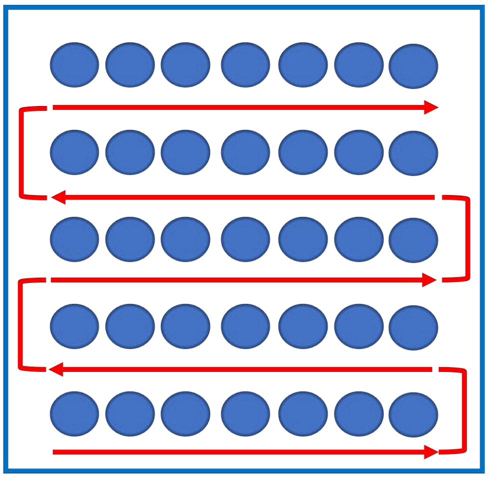

Figure 5. Illustration of the movement of the tip along the TERS grid

4.3 Results and Discussion

4.3.1 AFM Topography Measurements

Representative topography images of SARS-CoV-2 are shown in Figure 6. The virus appears to have the shape of spherical or ellipsoidal particles. However, despite the fact that well-spherical structures are to be expected, this was not always the case. A virus particle was also observed to be combined with some residues, resulting in a non-spherical shape. During the process of sample preparation, a total of three distinct inactivation procedures were used. First, the AFM topography shown in Figure 6 (A-C) was obtained from a viral sample that had been treated with PFA to inactivate the virus. It shows a virus cluster (6A) in addition to individual viruses (6B and C) that have heights of 93 nm and 68 nm respectively. The cluster virus was measured directly from a glass substrate, without Poly-l-lysine pre-treatment. Second, the AFM topography illustrated in Figure 6 (D-F) was acquired from a viral sample that had been inactivated by exposure to UV-C radiation.

It presents individual viruses with a similar shape and average height between 50-86 nm. Nonetheless, clustered viruses were identified in this virus sample to a negligible degree. In addition, it was difficult to detect the virus on the substrate, which is suspected that the virus amount on the substrate was significantly lower than in the PFA sample. Third, the virus sample was inactivated by UV-C radiation followed by incubation in a PFA solution. The detected particles are shown in Figure 6 (G-I). Figure 6G shows viruses with a height of 82 nm. Individual viruses with heights of 62 nm and 75 nm were also found in Figure (H-I) respectively. Even though clustered viruses were rarely found, it was comparatively easy to locate individual viruses on a substrate compared to UV-C samples.

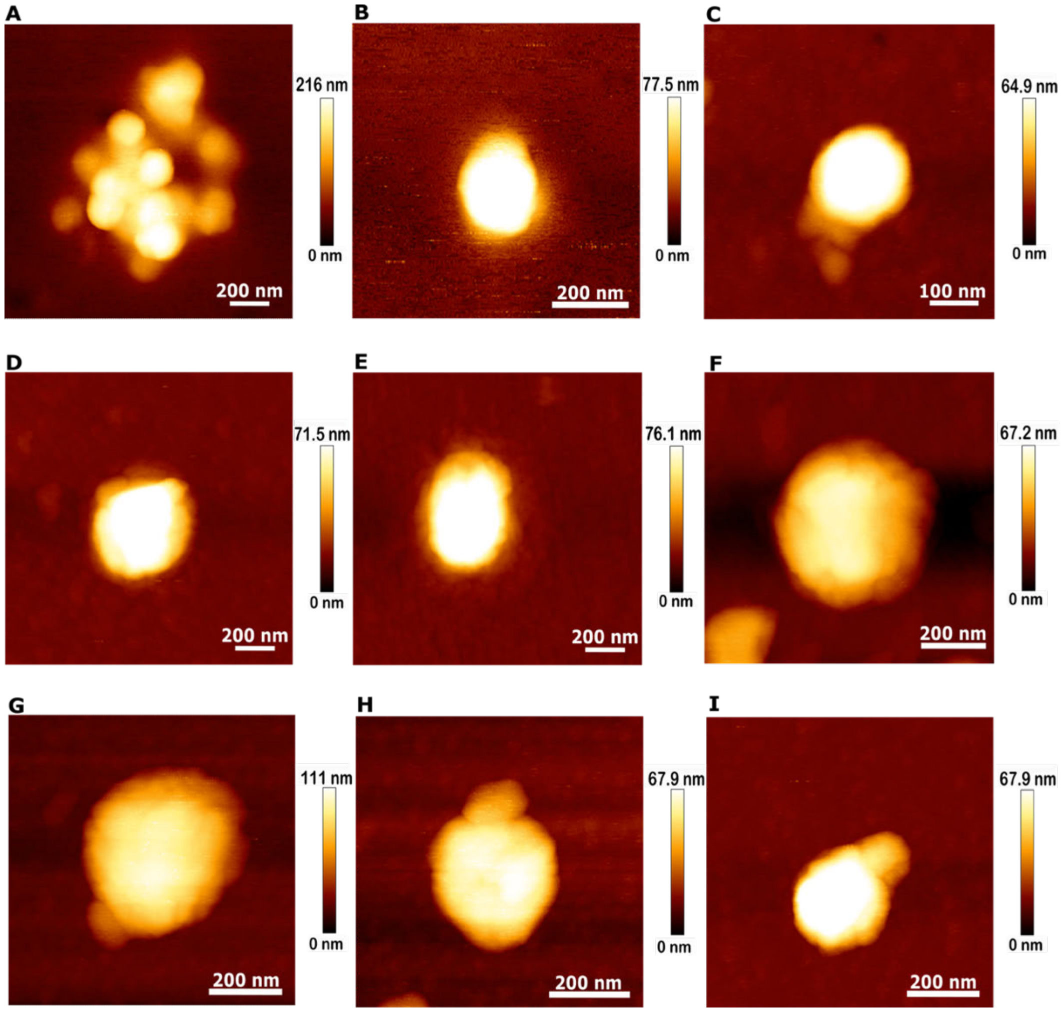
A
216 nm
0 nm
200 nm
B
77.5 nm
0 nm
200 nm
C
64.9 nm
0 nm
100 nm
D
71.5 nm
0 nm
200 nm
E
76.1 nm
0 nm
200 nm
F
67.2 nm
0 nm
200 nm
G
111 nm
0 nm
200 nm
H
67.9 nm
0 nm
200 nm
I
67.9 nm
0 nm
200 nm

Figure 6. AFM topography of SARS-CoV-2 from differently inactivated samples. (A-C) Paraformaldehyde (PFA), (D-F) Ultra Violet-C (UV-C), and (G-I) PFA-UVC inactivation respectively.

In the initial stages of the AFM SARS-CoV-2 investigations, the PFA inactivation method was utilized extensively. This was due to the fact that the PFA inactivation approach is the most often employed virus inactivation method in Biolabs [224, 225]. It has been demonstrated that 4% paraformaldehyde fixation of SARS-CoV-2-infected cells successfully inactivates the virus [226]. PFA is responsible for the formation of covalent crosslinks between peptide/protein molecules, which act as glue [227]. As a result, the virus is expected to cluster in some instances. On the other hand, PFA can also bond with itself and form aggregates with a spherical structure similar to that of the virus (Figure 7), which can cause confusion when attempting to identify virus particles (as mentioned as well in Yao's thesis result [228]). The height characteristics, however, show that the PFA aggregates have a lower average height, which is below 35 nm. Consequently, the virus can still be differentiated.

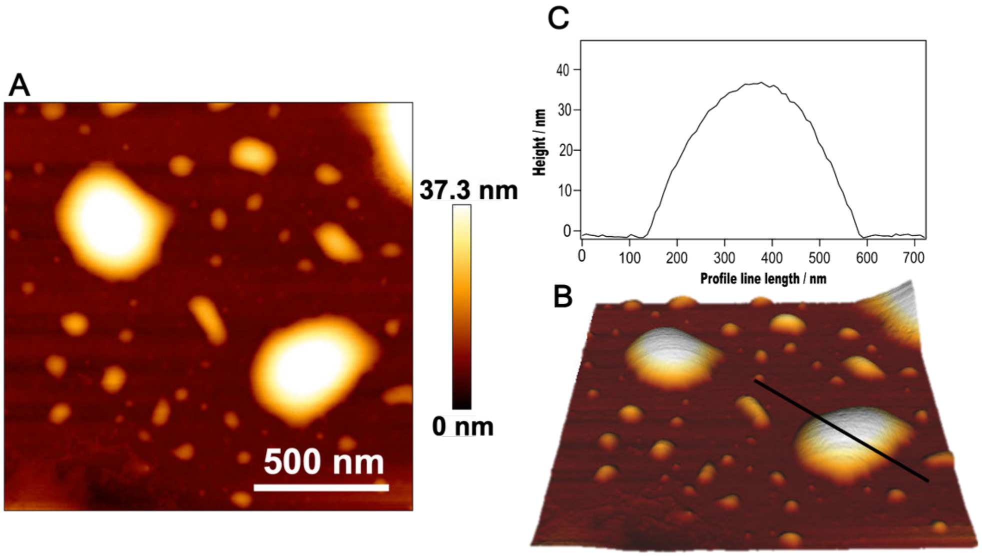

Figure 7. AFM topography of pure PFA (A). (B) 3-D image from the AFM topography in Figure A. (C) height information from the structure in Figure B (black line).

To prevent any PFA's influence on the viral structure, another non-chemical inactivation utilizing Ultraviolet (UV) irradiation is carried out. UV irradiation has been thoroughly studied, is frequently employed, and offers a number of benefits, including rapid efficacy, no chemical residue, and minimal sample degradation [229]. There are three types of ultraviolet light: UV-A (315–400 nm), UV-B (280–315 nm), and UV-C (100–280 nm), with UV-C being the most widely used for germicidal purposes. Viral inactivation at a wavelength of 254 nm can be attributed to direct UV-C light absorption and photochemical damage to nucleic acid, which disrupts the viral replication [229-231]. The challenge with using a UV-C inactivated sample for an AFM investigation is that it is relatively difficult to find the virus on the glass substrate. This might be due to the lack of a chemical agent, such as PFA, capable of strongly immobilizing viruses to the substrate or forming virus clusters. Consequently, the viruses are easier to remove from the substrate for example during the washing process, resulting in a lower population. To improve the situation, glass substrates must be modified by coating with Poly-L-lysine (PLL). PLL is a water-soluble, cationic polypeptide composed of naturally occurring L-lysine with amine groups on the side chains. It has a lot of potential in biological applications such as cell culture as coating materials, and bacterial immobilization via an electrostatic interaction [232, 233].

Under physiological conditions, the spike protein of SARS-CoV-2 has a heterogeneous charge distribution [234]. The protein's surface is positively charged, while the middle and lower portions are negatively charged, as experimentally demonstrated by Turoová et al., [235], this ensures its stability and prevents cluster formation. As PLL also carries a positive charge, this may explain why it is not entirely effective at interacting with the virus, and the cluster is difficult to observe in the absence of covalent crosslinkers such as PFA.

In order to take advantage of both PFA and UV-C as an inactivation method, the combination of the two is utilized. In the beginning, viruses were inactivated by employing UV-C, which, as was previously explained, is a quick method that minimizes the amount of sample degradation and structural alterations. After that, PFA is used to strengthen the adhesion to the glass substrate via the crosslinking mechanism. Although some PFA aggregates are still present, they are not as abundant as in PFA-inactivated samples, which is a major advantage.

Within the context of this AFM study, the most important identification characteristics are height and morphology. The height characteristic indicates that different inactivation methods result in a similar height of the virus, which is between 50 and 85 nm, and morphology analysis shows that the virus particles are generally spherical or fairly pleiomorphic, which agrees with the electron microscope result [46]. On the other hand, the particles can also be confused with other materials, such as cell debris aggregates. Fluorescence microscopy is thus used to validate the virus appearance obtained by AFM.

4.3.2 AFM-Fluorescence Microscopy Correlation Study

A designed glass substrate covered with a grid composed of numbers and letters was utilized to verify the AFM results (Figure 8). The same three distinct inactivation-method samples from the previous section were utilized. First, using the AFM, the virus needs to be located close to a particular number or letter on the grid (Figures 10, 11, 12 A-white square). This information must then be documented so that the virus can be easily tracked. As mentioned beforehand, the viruses were selected by characterizing the shape and height topography, which is somewhere above 50 nm. The detailed AFM images of the viruses from each sample were given in Figures 10, 11 (C and D), and 12 (C-F) respectively so that they could be observed more clearly. Following that, the sample is immunolabeled with a specific spike protein antibody in preparation for fluorescence imaging. The scheme of the AFM-fluorescence correlation study is illustrated in Figure 9.

Immunolabeling has been accomplished with the use of dye molecules, Alexa fluor 488. Alexa dyes are frequently used to label proteins because they are more resistant to photobleaching and self-quenching. In contrast to other fluorophores such as fluorescein and sulforhodamine, its fluorescence is significantly quenched upon conjugation to biological molecules, particularly proteins. Furthermore, because of their high quantum efficiencies, they are well-suited for single-molecule studies in which brightness is a key factor. It is also water-soluble and pH-insensitive from 4 to 10 [236, 237].

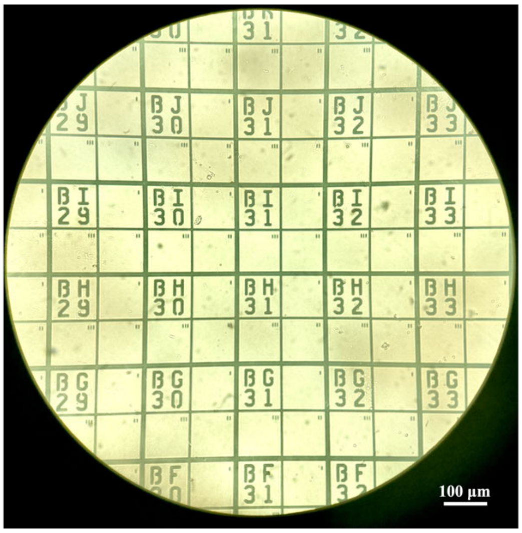

Figure 8. Image of a special glass substrate with grid numbers and letters, obtained by light microscope with 20x objective lens.

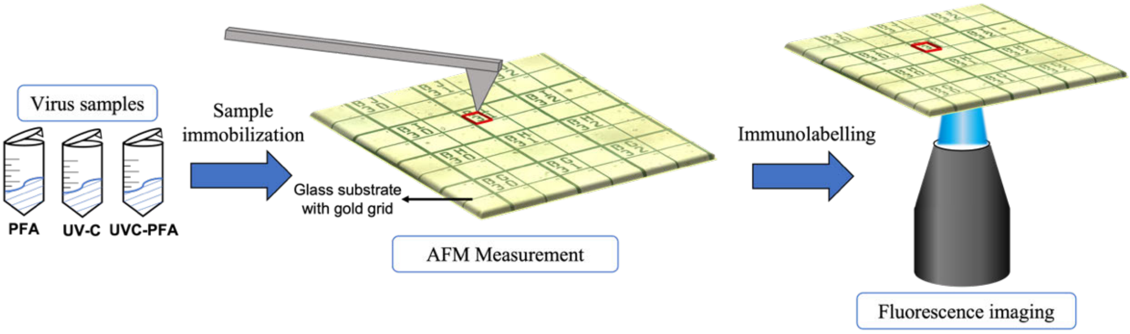
Virus samples
PFA
UV-C
UVC-PFA
Sample immobilization
Glass substrate with gold grid
AFM Measurement
Immunolabelling
Fluorescence imaging

Figure 9. Illustration of AFM-fluorescence correlation measurements

Fluorescence imaging has been performed using a laser wavelength of 488 nm with a power of 25 µW. Begin by locating the same number or letter grid used in AFM measurement. Then by observing the fluorescence, it must be determined whether the virus can be located in the same position (Figure 9). Because it has been immunolabeled specifically for SARS-CoV-2, the fluorescence emission observed must originate from the virus. According to the findings, fluorescence imaging was successful in confirming the presence of at least 5 virus particles in the samples that were inactivated with PFA. Of these virus particles, two are represented in the AFM topography shown in Figures 10 C and D. The virus has two different heights, which are 82 and 69 nanometers respectively.

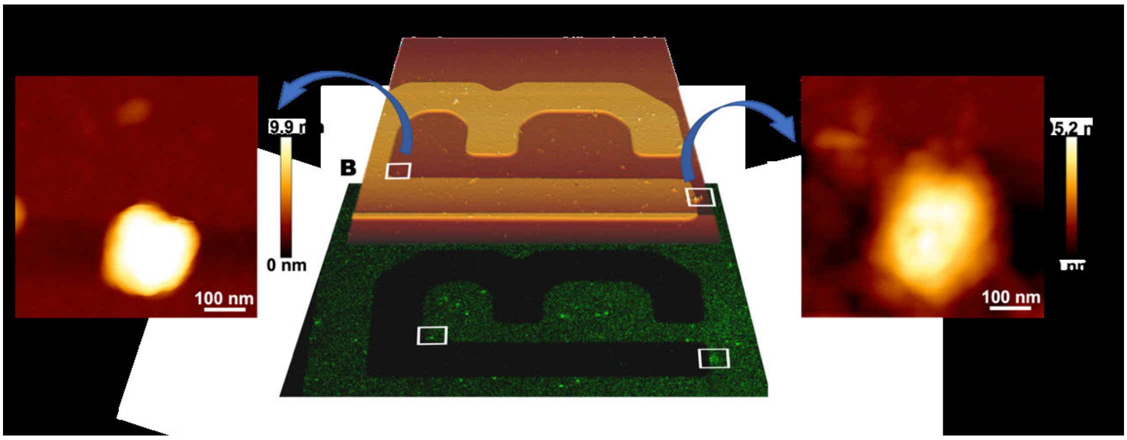

Figure 10. AFM-fluorescence microscopy correlation experiments. (A) AFM topography of a PFA-inactivated SARS-CoV-2 sample on a substrate patterned with gold letters and numbers. (B) Fluorescence image from the same sample area in Figure (A). (C, D) Detailed AFM topography of the virus marked in Figure A with a white square.

A superimposition of two images, the fluorescence and the white field of the grid, is required in order to locate the same virus on the letter "B" of the grid in Figure 11B. This takes place as a result of the fluorescence being less intense, which makes the grid letter "B" impossible to see. Eleven virus particles originating from samples that had been inactivated by UV-C were successfully observed and correlated, two of which are illustrated in Figures 11 C and D. The topography images that are presented in Figure 11C demonstrate that the height is 57 nm, which is a little bit lower when compared to the height of the other inactivated samples. It is possible that this is because the particle in the images is not the virus itself but rather a virus fragment. However, the majority of the virus particle heights that have been measured are still between 60 and 85 nm, as shown for instance in Figure D, which has a height of 77 nm.

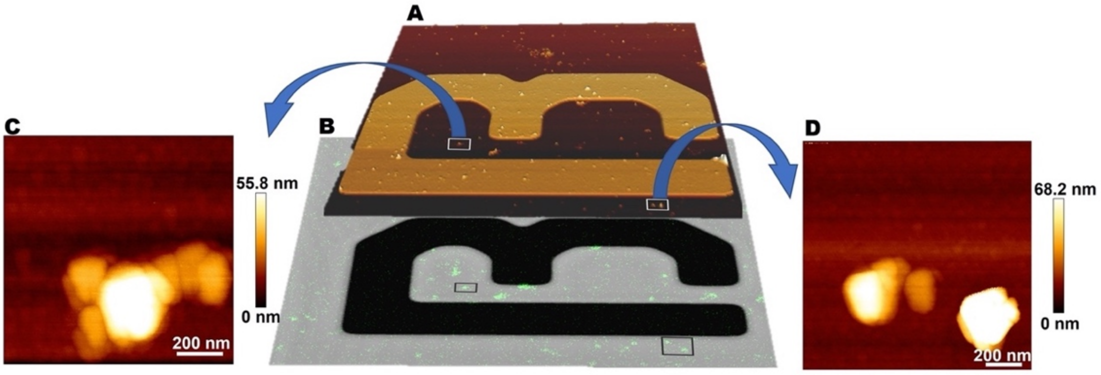

Figure 11. AFM-fluorescence microscopy correlation experiments. (A) AFM topography of a UV-C-inactivated SARS-CoV-2 sample on a substrate patterned with gold letters and numbers. (B) Fluorescence image from the same sample area in Figure (A). (C, D) Detailed AFM topography of the virus marked in Figure A with a white square.

Figure 12 presents the results of yet another AFM-fluorescence study, which successfully correlated twenty-two virus particles derived from UVC-PFA-inactivated samples. Figure 12 C-F presents four different topography images, each of which has a different height (66, 82, 59, and 67 nm respectively).

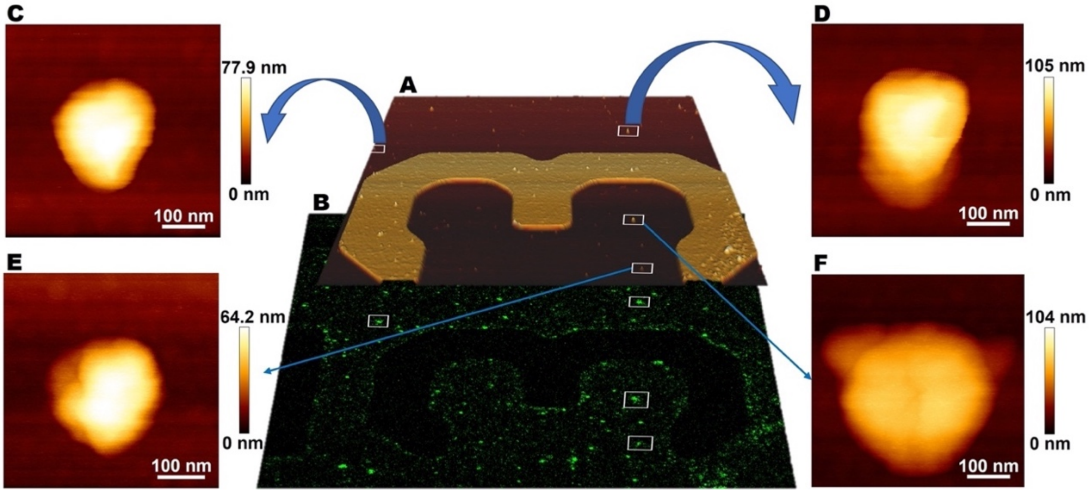

Figure 12. AFM-fluorescence microscopy correlation experiments. (A) AFM topography of a UV-C-PFA-inactivated SARS-CoV-2 sample on a substrate patterned with gold letters and numbers. (B) Fluorescence image from the same sample area in Figure (A). (C-F) Detailed AFM topography of the virus marked in Figure A with a white square.

Despite the successful AFM-fluorescence correlation study shown in Figures 10, 11 and 12, some areas could not really be correlated. For instance, some AFM virus particles, with typical heights ranging from 50 to 85 nm, either did not show fluorescence or had a very weak intensity (e.g., Figure 13). This could be due to the immunolabelling not being properly bound to the virus particles or the virus being washed during the labeling process. On the other hand, while there was a lot of fluorescence in the fluorescence image, the height was less than 35 nm in the AFM images (Figure 14). This could be because the fluorescence immunolabeling in this study is specifically bound to the S protein found on virus surfaces, therefore, any particle containing S protein including fragments from broken viruses would also be labeled and produce fluorescence despite the low topography height. The AFM-fluorescence correlation study confirms that the spherical or ellipsoidal particles observed on the AFM images are SARS-CoV-2 with a height ranging from 50 to 85 nm.

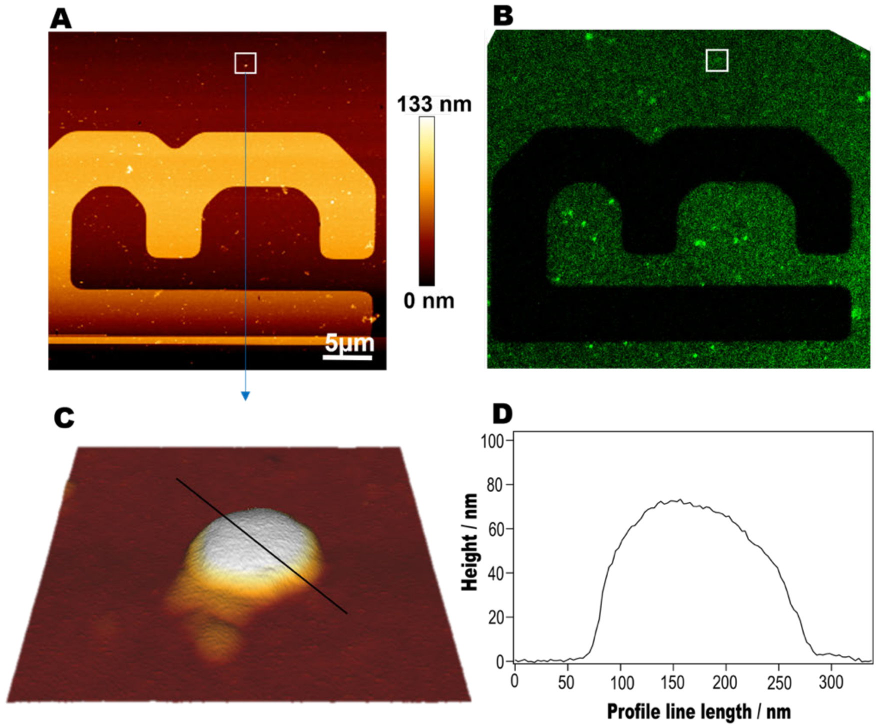
A
133 nm
0 nm
5μm
B
C
D
100
80
60
40
20
0
Height / nm
0
50
100
150
200
250
300
Profile line length / nm

Figure 13. False negative AFM-fluorescence microscopy correlation experiments. (A) AFM topography of the virus (marked in a white square). (B) Fluorescence image from the same sample area as in Figure A, with weak fluorescence visible from the same virus. (C, D) 3D image of Figure A and line profile across single particle as indicated in C.

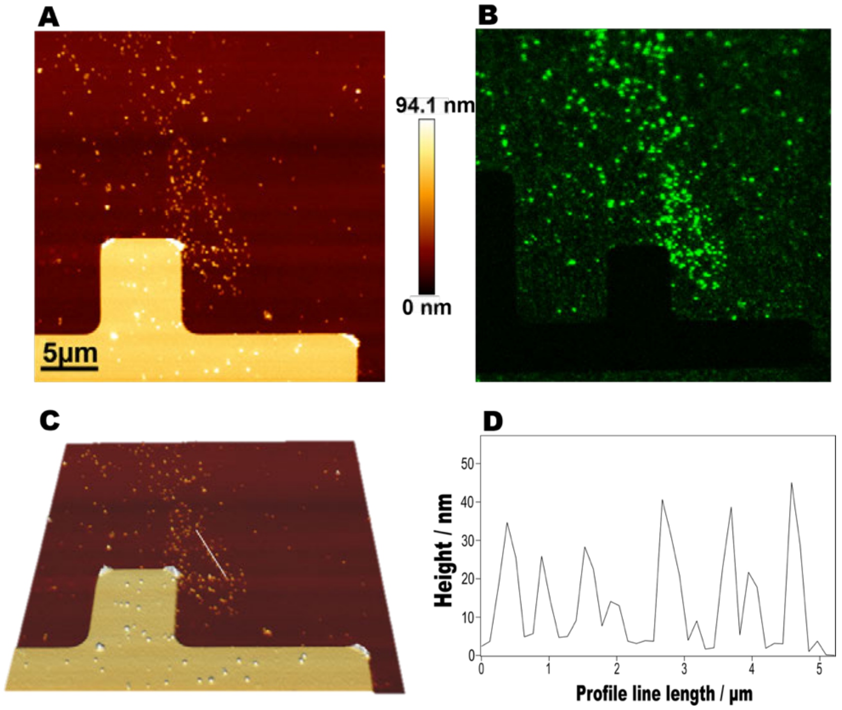
A
B
94.1 nm
0 nm
5μm
C
D
50
40
30
20
10
0
Height / nm
0
1
2
3
4
5
Profile line length / μm

Figure 14. False positive AFM-fluorescence microscopy correlation experiments. (A) AFM topography of virus fragment. (B) Fluorescence image from the same sample area as in Figure A. (C, D) 3D image of Figure A and line profile across virus fragments as indicated in C.

4.3.3 TERS Measurements of SARS-CoV-2

Tip-enhanced Raman scattering (TERS) was used to obtain chemical information from the surface of SARS-CoV-2. Figure 15 shows the results from UVC-PFA inactivated samples. Compared to the UV-C sample, the UVC-PFA sample demonstrates to have several virus clusters (as explained in the AFM result) so that TERS information can be obtained from a different virus simultaneously.

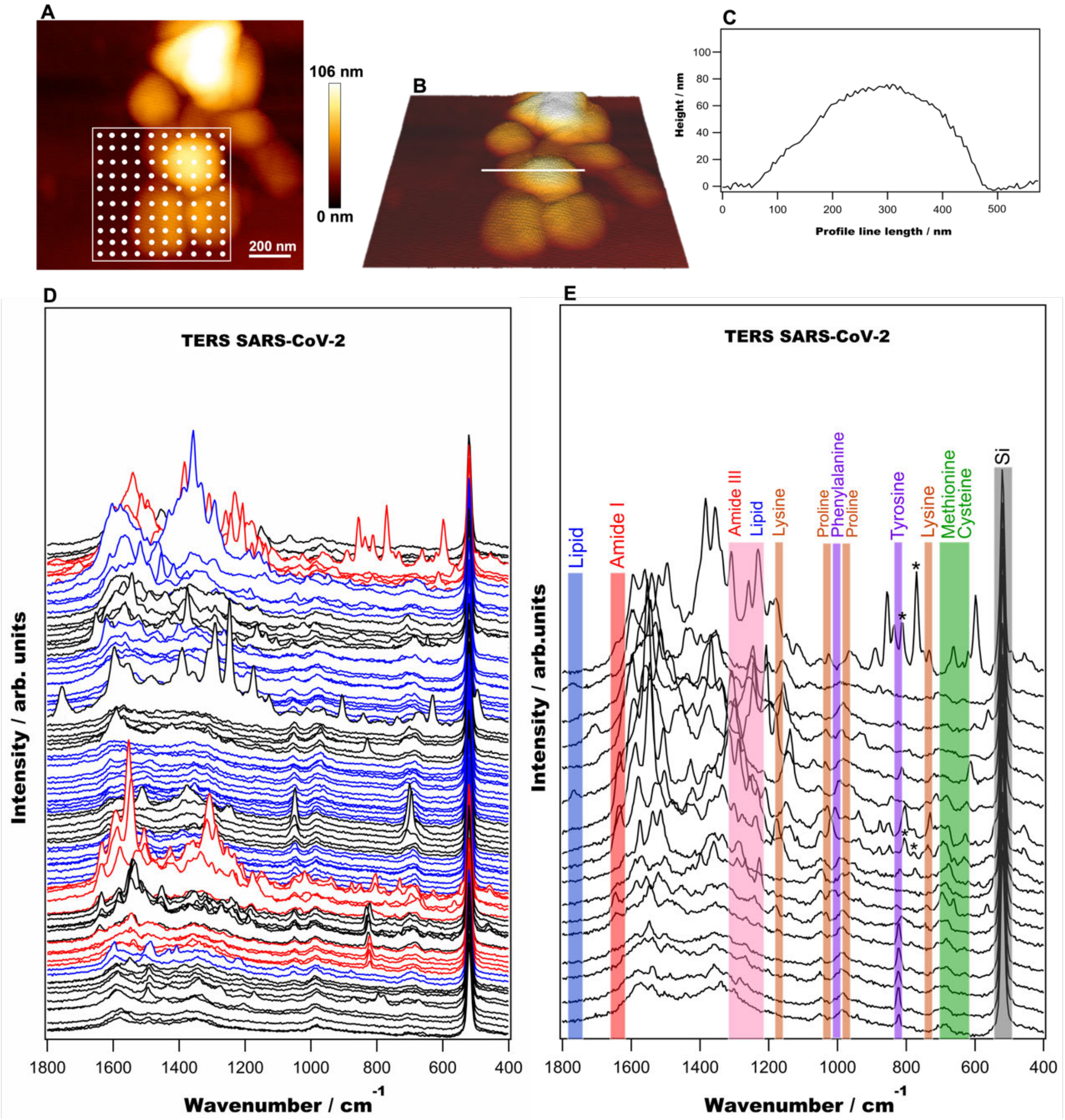

Figure 15. TERS spectra acquired on SARS-CoV-2. (A) AFM topography of clustered viruses, (B, C) 3D image of Figure A and line profile across single particle as indicated in B. (D) TERS spectra from 100 measurement points on the grid in Figure A, (blue and red = spectra from the virus particles, black = outside the virus/ on glass substrate). (E) Selected TERS spectra from Figure D red, with highlighted bands from lipids (blue), protein secondary structure (Amide I, III, red), aromatic amino acids (purple), aliphatic amino acids (brown), amino acids containing sulfur (green) and bands from RNA (*). The sharp peak at 521 cm^{-1} is from the Silicon (Si) of the AFM tip (grey).

The AFM topography result in Figure 15A indicates that the viruses are in a cluster with a height of around 65-72 nm. Figure 15B shows a three-dimensional image of the virus morphology with a spherical structure, and Figure 15C provides specific height information from a white line drawn in Figure 15B, which is 72 nm.

The TERS spectra were recorded in a grid with 10 by 10 points of measurement (Figure 15A), with a step size of 70 nm between each point, and the direction of the measurement was illustrated in Figure 5. After that, the findings are presented in Figure 15D. It can be observed that some spectra exhibit very few or no bands at all, which were obtained from places or points outside of the viruses (e.g., first 10 spectra, black). In this measurement, rather than concentrating on achieving a high spatial resolution, the primary goal is to acquire the very first TERS information from a number of different virus particles. Consequently, the spectra illustrated in Figure 15E were chosen based on the appearance of significant or high-intensity bands, which makes it easier to extract information from the spectrum.

The analysis of the spectra results from Figure 15E can then be divided into three categories of biopolymers. First, bands from proteins dominate the TERS spectra of SARS-CoV-2. The analysis can be divided into two different protein-level structures. In the beginning, an analysis of protein secondary structure can be observed at 1630-1660 cm^{-1}, marked red in Figure 15E. These bands can be assigned to the Amide I signature. As mentioned in Chapter 3, the Amide I bands contain contributions from C=O stretching vibration (80%), C-N stretching (10%), and N-H bending vibrations (10%) of the peptide backbones [166]. From the Amide I position (1635-1645 cm^{-1}), it was concluded that α-helix structures dominate, so it can be speculated that the S2 subunit of S protein was probed. It is well known that the S-glycoprotein contains three main regions. These regions are referred to as signal peptides, S1 subunit, and S2 subunit area. Both the binding of receptors and the fusing of membranes are the responsibilities of the subunit areas (S1 and S2) (Figure 16B-D) [238, 239]. The S2 subunit is composed of a variety of domains, one of which is made up of heptapeptide repeat sequence 1 (HR1) and heptapeptide repeat sequence 2 (HR2). This HR1 and this HR2 combine to form the six-helical bundle (6-HB) (Figure 16E), which is necessary for the S2 subunit to perform its function of viral fusion and entry [238, 240, 241]. Therefore, it can be postulated that with TERS the alpha-helix structure of 6-HB in the S2 subunit was probed. Figure 16 illustrates the structure of the SARS-CoV-2 spike protein.

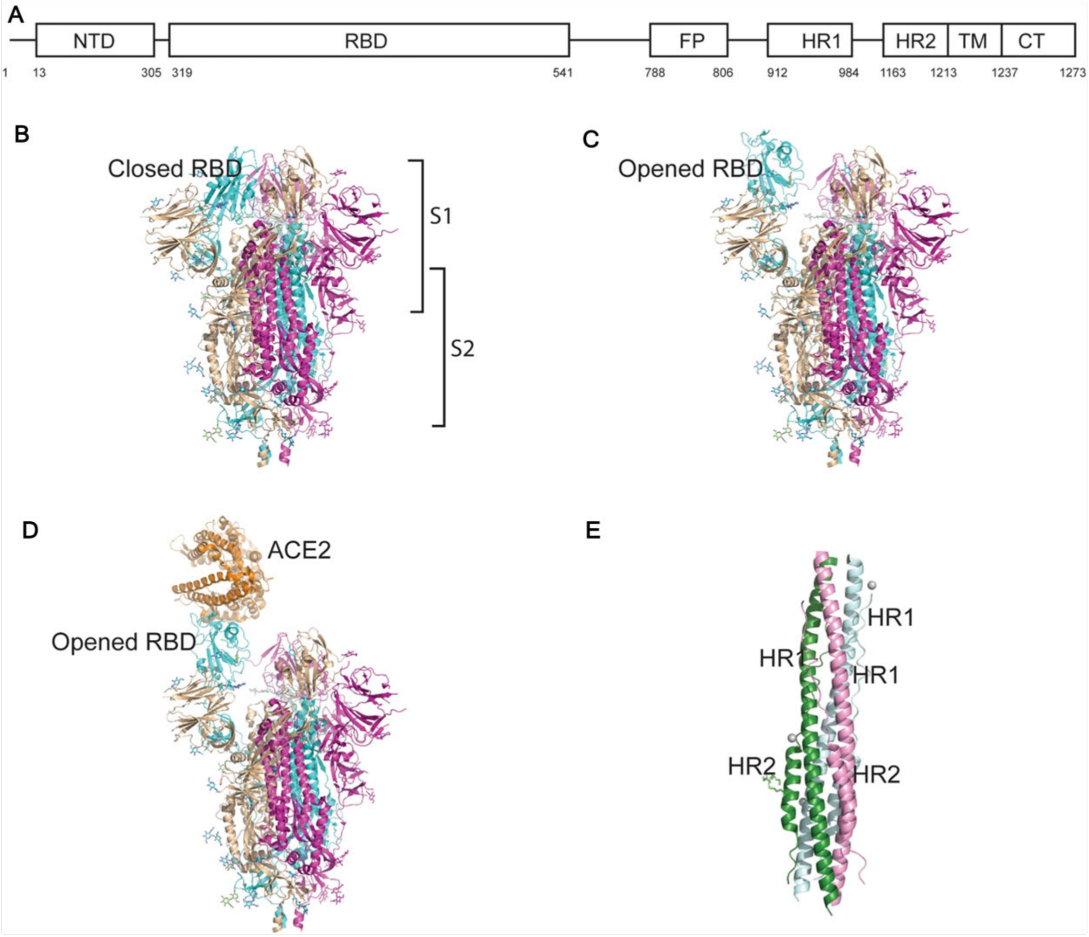

Figure 16. (A) Schematic representation of the SARS-CoV-2 spike protein. The S1 subunit consists of the N-terminal domain (NTD) and receptor binding domain (RBD). The S2 subunit contains fusion peptide (FP), heptad repeat 1 (HR1), heptad repeat 2 (HR2), transmembrane domain (TM), and cytoplasmic tail (CT). (B–C) The S protein RBD closed and opened status. (D) The S protein binds to ACE2 (Angiotensin-converting enzyme 2) with opened RBD in the S1 subunit. (E) The six-helix structure formed by HR1 and HR2 of the S2 subunit. Images adapted from Huang *et. al.,* [238], under the terms of license number 5435410588937.

Another Raman marker band of the protein's secondary structure is the Amide III region around 1200-1340 cm^{-1}. These bands are generated by complex vibration modes in the peptide backbones that involve C-N stretching and N-H bending. However, assigning and interpreting this region to the protein secondary structure can be challenging because other functional groups for example from lipids such as C-H stretching at 1200-1400 cm^{-1} can overlap [134]. As a result, Amide I bands are predominantly used to investigate and characterize the protein's secondary structure.

The second analysis of protein bands is based on the primary structure from the amino acids. The results are divided into two groups: aromatic and non-aromatic amino acid side chain residues. In the aromatic amino acids, two Raman marker bands are observed between 824-828 cm^{-1} and around 1005 cm^{-1} (marked purple in Figure

15E), which can be assigned to out-of-plane ring vibrations of tyrosine and the symmetric ring breathing of phenylalanine, respectively. In addition, bands from tyrosine at 824-828 cm^{-1} are predominantly detected. This could be also coming from the S2 subunit of the S protein. A study by Howard *et. al.,* [242], demonstrates that in S-glycoproteins of coronaviruses, there is a region called juxta membrane domain (JMD), a region in the ectodomain between the end of HR2 and the beginning of the transmembrane domain) (Figure 16A), which is rich in aromatic amino acids. The results show that JMD of coronaviruses contains 14 amino acids, six of which are tyrosine and tryptophan residues, that play important roles in membrane fusion. The result is also in a good correlation with the appearance of the alpha-helix structure, which is postulated to belong to the S2 subunit of the S protein. Because tyrosine bands appear in the same spectra as alpha-helix structures, it is very likely that they originate from the same location, namely the S2 subunit. Despite the fact that S2 subunits are not located on the surface, it is possible that the spike protein of the virus is not in an upright position but rather horizontally flat, exposing the S2 subunit to the TERS probe. This explanation is plausible given the interaction tendency between positively charge Poly-L-Lysine (PLL) on the substrate and the negatively charge S2 subunit (explained previously).

Non-aromatic amino acids are another category group to be investigated. The bands at 737, 1172 cm^{-1} and at 986, 1037 cm^{-1} in the TERS spectra in Figure 15E can be assigned to lysine and the aliphatic amino acid proline, respectively (marked brown). The bands from the sulfur-containing amino acids cysteine and methionine (marked in green) were detected between 632-698 cm^{-1} and can be assigned to molecular stretching of C-S in cysteine and methionine side chain residues.

The second type of biopolymer refers to the detection of lipids indicated by bands between 1745-1764 cm^{-1} (blue bar). These bands can be assigned to C=O the stretching mode in phospholipids. These lipid bands could be generated from the virus's bilayer lipid membrane. These bands are randomly observed because the lipid membrane is located beneath the surface/S protein, as shown in Figure 2. It is suspected that some areas of the virus's surface are devoid of S protein spikes, allowing the TERS probe to reach the bilayer lipid membrane and acquire signals from the lipid structure.

And last is the appearance bands from biopolymer nucleic acid (RNA), at ~781-810 cm^{-1} (marked in asterisk*). The origin of these bands is from the symmetric stretching of the molecule (-O-P-O-) in the RNA backbone. As mentioned previously, TERS is a surface-sensitive technique, and the RNA resides within the virus (Figure 2). Accordingly, the occurrence of RNA bands is unexpected. It is hypothesized that

RNA from broken viruses might attach to the surface of the other viruses, such that when TERS probes the surface of the virus, the signal from RNA can also be retrieved. However, this is not always the case, as seen by the infrequent occurrence of RNA bands. Nevertheless, the possibility of the existence of this band cannot be excluded. In addition, a strong Raman band at 520 cm^{-1} originated from the TERS probe's Silicon tips (in Figures 15 and 17).

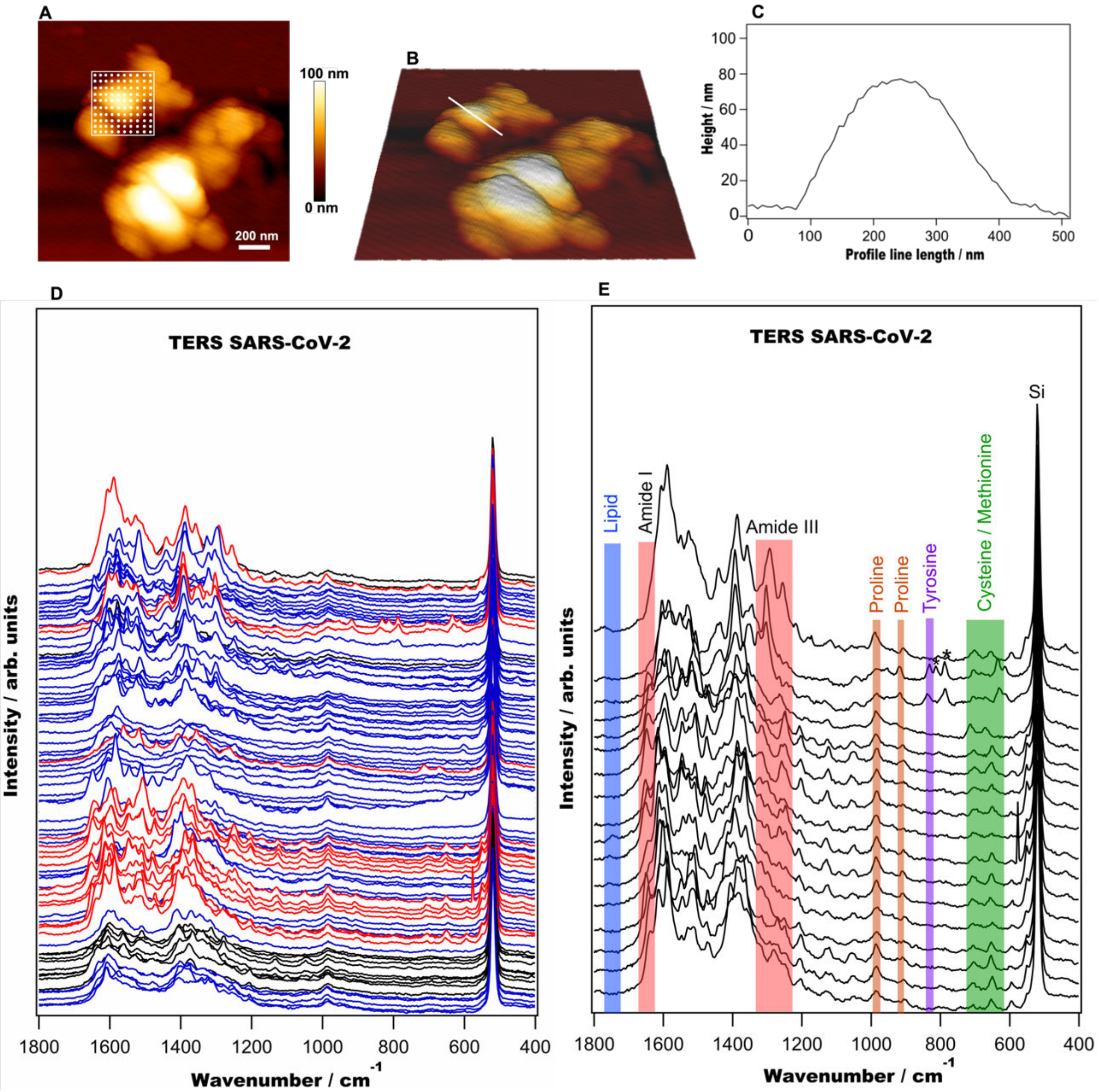

Figure 17. TERS spectra acquired on SARS-CoV-2. (A) AFM topography of clustered viruses, (B, C) 3D image of Figure A and line profile across single particles as indicated in B. (D) TERS spectra from 100 measurement points on the grid in Figure A, (blue and red = spectra from the virus particles, black = outside the virus/ on glass substrate). (E) Selected TERS spectra from Figure D red, with highlighted bands from lipids (blue), protein secondary structure (Amide I, III, red), aromatic amino acids (purple), aliphatic amino acids/proline (brown), amino acids containing sulfur (green) and bands from RNA (*). The sharp peak at 521 cm^{-1} is from the Silicon (Si) of the AFM tip.

A second TERS data set from a different virus cluster is given in Figure 17, where Figure 17A shows the AFM topography of the virus cluster, and Figure 17B is the 3D image of Figure 17A. In Figure 17C, the virus height (white line Figure 17B) is determined as 78 nm. The TERS spectrum was obtained using a 10 x 10 grid with a 40 nm step size and the same direction of the measurement which was illustrated in Figure 5. Figure 17D represents 100 spectra acquired from the grid. A smaller step size was chosen to confine the probe to a smaller area. The selected spectra from Figure 17D are given in Figure 17E showing that three types of biopolymers can also be identified.

First, one spectrum with bands at 788-810 cm^{-1} can be assigned to the RNA backbone's stretching mode (marked with an asterisk*). Although it only appears in one spectrum, however, the possibility of the existence of this band cannot be excluded. Another band at 1745 cm^{-1} can be assigned to the C=O stretching mode from phospholipids (marked in blue). Second, lipid bands were detected more frequently in this TERS data set than in the previous one, although the band intensity was still weak. It can be hypothesized that the location of the lipid beneath the S protein is one of the reasons because TERS is a near-field technique (as previously stated), therefore, tip and sample distance play important roles in generating enhanced Raman signal. A second possibility is that the laser's focus was altered slightly during the measurement, which will also affect the signal's intensity. On the other hand, it could be because the TERS tip's enhancement properties were reduced after several measurements, which would explain the phenomenon [76].

Finally, proteins can be identified by their secondary structure and amino acids. The secondary structure is characterized by a prominent Amide I band at approximately 1645 cm^{-1}, which originates from the alpha-helix structure. In addition, beta-sheet structures of the protein are indicated by bands between 1664-1680 cm^{-1} (marked red). Possible Raman marker bands from Amide III can also be observed at around 1235-1300 cm^{-1}.

The amino acids assignment in this TERS data set appears to be slightly different since there are no aromatic amino acids (phenylalanine) were detected. Firstly, it is possible that the TERS probe acquired the spectra from the location which no appearance of phenylalanine. Secondly, it could be due to the selection rules, one of which is based on the orientation of the molecules in regard to the tip and incident light polarization, which could affect the band detection [76]. On the other hand, the bands originating from aromatic amino acids (tyrosine) can still be observed at 831 cm^{-1}. This is consistent with previous TERS findings that provided an explanation for the predominance of tyrosine in S protein. In addition, two Raman marker bands from an aliphatic amino acid (proline) can also be observed at 921 cm^{-1} and 986 cm^{-1} (Figure 17E, highlighted in brown), which are the result of ring breathing vibration.

Furthermore, Raman marker bands from cysteine and methionine around 635-701 cm^{-1} appear frequently (marked green). The results are consistent with the study by Singh *et al.*[243], which indicated that the protein sequence of SARS-CoV-2 spike protein is rich in cysteine (Cys) residue. From the sequence of 1273 amino acids, there are 40 cysteine residues, 9 of which are located in the receptor-binding domain (RBD) of the S1 subunit (Figure 16). It is plausible that the TERS probe acquired spectra from the surface-located S1 subunit region during this TERS measurement. Furthermore, among known human pathogens in the closely related family of β-coronaviruses, the S protein of SARS-CoV-2 has the most cysteine-rich cytoplasmic tail [244]. Cysteine residues play critical roles in protein structural stabilization, catalytic activity, and post-translational modification.

Methionine is one of the most hydrophobic amino acids found in nature and its residues are typically found buried in the hydrophobic core of globular proteins or attached to lipid bilayers. Consequently, the appearance of the C-S bands from methionine is not expected. Nonetheless, the molecular symmetry properties of methionine residues of the spike protein play a crucial role in a variety of tasks during the virus's lifecycle. Bands at 652 cm^{-1} correspond to C–S bond stretching vibrations on the CH_2 side of molecules in the gauche rotameric configuration, whereas the signal at 669 cm^{-1} originates from the identical vibrational mode on the CH_2 side of molecules in the trans configuration. In contrast, signals at position 698 cm^{-1} can be assigned to C–S stretching of the carboxyl side of the CH_3 molecule in gauche and trans configurations [245, 246]. All bands assignment from TERS results is given in Table 1.

Using TERS, proteins and their secondary structure including specific amino acids can be characterized in a complex environment (i.e., virus particle) that contains other biopolymers such as lipids and nucleic acid (RNA). On the basis of the presence of protein, lipid, and RNA bands in TERS spectra, it can also be concluded that, in addition to fluorescence, TERS can confirm that the particles in AFM with around 50-85 nm high topography are SARS-CoV-2.

Table 1. Wavenumber, vibrational origin, type of biopolymer, and literature references from all TERS results.

Wavenumber (cm^{-1})	Assignment	Biopolymer	Ref
521	Silicon	-	[76]
632-637	C-S stretching cysteine	Protein*	[245, 247]
652-655	C-S stretching in methionine (CH$_2$ side; gauche)	Protein*	[245, 246]
669-670	C-S stretching in methionine (CH$_2$ side; trans)	Protein*	[245, 246]
683-688	C-S stretching cysteine	Protein*	[245, 247]
697-699	C-S stretching in methionine (CH$_3$ side; gauche)	Protein*	[245, 246]
737-741	Lysine	Protein*	[129]
770	Out-of-plane ring deformation, uracil	Nucleic Acid	[245, 248]
781	-O-P-O- symmetric stretching in RNA backbone	Nucleic Acid	[245]
806-810	-O-P-O- symmetric stretching in RNA backbone	Nucleic Acid	[245]
824-831	Out-of-plane ring vibrations, tyrosine	Protein*	[133, 245]
920	Ring breathing in proline	Protein*	[129]
986	Ring breathing in proline	Protein*	[129]
1005	Symmetric ring breathing in phenylalanine	Protein*	[129, 133, 245]
1033-1037	Ring breathing in proline	Protein*	[129]
1172-1179	C-C, C-N stretching in lysine	Protein	[129]
~1231	PO$_2$ asymmetric stretching	Lipid	[134]
1235-1300	Amide III (CN stretching, NH bending CO stretching, O=C-N bending	Protein**	[134]
1632-1660	Amide I (α-helix, random coil)	Protein**	[134, 135, 166]
1664-1680	Amide I (β-sheet)	Protein**	[134, 135]
1745-1764	C=O stretching in phospholipids	Lipid	[134, 245]

*Amino Acids

** Secondary Structure

4.4 Chapter 4 Conclusion

This work employed Atomic Force Microscopy (AFM) and Tip-enhanced Raman scattering (TERS) to characterize severe acute respiratory syndrome coronavirus 2 (SARS-CoV-2). Three different inactivation method samples were used, those are PFA, UVC, and UVC-PFA. In the beginning, AFM was used to investigate the topography information from the virus. The results demonstrate that the virus has a spherical to ellipsoidal shape with an average height between 50 and 85 nm. It is easier to locate the virus in PFA-inactivated samples than in ones treated with UVC. This is due to the fact that PFA has the ability to covalent crosslinks between molecules and act as glue. Consequently, clustered viruses are also identifiable in the PFA samples. UVC-inactivation, on the other hand, has the advantages of rapid efficacy, absence of chemical residue, minimal sample degradation, and samples that resemble closer to the natural specimens. The AFM result was then validated using an AFM-fluorescence correlation study. In both AFM and fluorescence measurements, a special grid substrate is used to precisely locate the virus. Immunolabelling is used to ensure that the fluorescence is coming exclusively from the virus particles. The results show that viruses (from all three different inactivation methods) with an AFM topography height of 50-85 nm fluoresce in fluorescence imaging. At last, TERS was used to retrieve individual virus's chemical information. The measurement was carried out on clustered viruses from the UVC-PFA sample. More than 100 spectra were obtained from two different cluster viruses. The findings reveal that three types of biopolymers are identified: nucleic acid (RNA), lipids, and protein, which are components of the virus. Protein analysis revealed that the secondary structure (alpha helix) was the most prominent in the spectra. Furthermore, the primary structure reveals both aromatic and non-aromatic amino acids, especially sulfur-containing amino acids (methionine and cysteine), where cysteine is abundant in the spike protein of the virus. Overall, using TERS both morphology and chemical information from SARS-CoV-2 can be retrieved.

CHAPTER 5
GENERAL THESIS CONCLUSION

In the presented thesis it has been demonstrated that the combination of atomic force microscopy (AFM) and plasmon-enhanced Raman spectroscopy is a powerful analytical technique for characterizing proteins at the nanoscale level. It is possible to obtain not only high-resolution topography of the sample but also detailed chemical information of the sample surface. Within this work, three different topics were addressed. First, the primary peptide structure was studied in filamentous structures to develop an approach for direct protein sequencing using AFM and tip-enhanced Raman scattering (TERS). Since the formation and degradation of amyloidogenic structures is still not fully understood, the second study focused on the behavior of amyloid fibrils in solutions with different pH values. Finally, the last study addressed the identification of proteins in the complex environment of a virus surface on the way to classify virus strains by their morphologic and chemical fingerprint.

For the characterization of the primary structure, the native peptide structure first had to be unfolded and ensured that no refolding occurred. For this purpose, adducts from a short peptide composed of 14 amino acids and 4-bipyridine molecules were prepared. The topography of the produced filamentous structures was imaged with an AFM and TERS was used to discern the individual building blocks on the surface of the threads. Although the filaments were composed of multilayers, it was possible to identify the different amino acids and distinguish them from the bipyridyl residues. It turned out that the stretching and separation of the peptide-bipyridine adducts were major obstacles to the nanoscale studies. Nevertheless, the results confirmed the theoretically predicted attachment of the bipyridyl to the N- or C-terminus of the peptide.

In the second study, the examination of the secondary structure in insulin amyloid fibrils was performed employing AFM and surface-enhanced Raman scattering (SERS). In the experiments, a fibril dissociation was initiated by suspending the specimen in different pH solutions. The AFM topographies already indicated the degradation of the micrometer-long fibrils by the formation of unstructured aggregates. Amyloid fibrils were found to gradually dissolve with increasing pH, and this dynamic process could be monitored in situ by time-dependent measurements. This gradual degradation was also evident from a change in the secondary structure of the fibrils, as shown by the SERS results. By examining the Raman marker bands of the peptide's secondary structure, namely amide I, it was demonstrated that the content of the originally predominant β-sheet structure decreased in favor of α-helix and random coil structures. The results shed light on the behavior of insulin amyloid fibrils and deepen the understanding of this potentially pathogenic species.

Finally, an AFM in combination with fluorescence microscopy and TERS were used to identify SARS-CoV-2 particles and investigate the protein structure on the complex virus surface. In the first step, the morphology of the viruses was characterized followed by antibody labeling. By using specially structured substrates, it was possible to rediscover the particles characterized with the AFM in the subsequent fluorescence measurements. This complementary approach enabled the clear identification and distinction of the viruses from other sample material.

Lastly, TERS was used to retrieve chemical information from the surface of the virus. The spectra enabled a tentative differentiation of the different subunits of the spike protein. Besides the identification of proteins, lipids and nucleic acids were detected on the virus surfaces. It is anticipated that the combination of techniques as applied in the present work will be very useful in the detection and characterization of SARS-CoV-2 and other viruses in the future.

The results of this work show that AFM and plasmon-enhanced Raman spectroscopy, and the combination of both, allow the characterization of protein-containing samples that is not directly possible with other methods (e.g., X-ray crystallography, nuclear magnetic resonance, and Electron Microscopy). In particular, the detection capabilities of TERS with high sensitivity and high resolution without the need for labeling is a valuable tool to analyze protein structures at different levels: the primary structure (sequence) of a peptide should be accessible with the presented approach. On the other hand, valuable information about the peptide chain arrangement on the nanometer scale can be obtained via the secondary structure. Finally, the characterization of proteins in a complex environment with other biopolymers such as lipids and nucleic acids is also possible.

ZUSAMMENFASSUNG

In der vorliegenden Arbeit wurde gezeigt, dass die Kombination von Rasterkraftmikroskopie (AFM) und plasmonenverstärkter Raman-Spektroskopie eine leistungsstarke analytische Technik zur Charakterisierung von Proteinen auf nanoskaliger Ebene ist. Es ist möglich, nicht nur eine hochauflösende Topographie der Probe zu erhalten, sondern auch detaillierte chemische Informationen über die Probenoberfläche. Im Rahmen dieser Arbeit wurden drei verschiedene Themen behandelt. Erstens wurde die primäre Peptidstruktur in fadenförmigen Strukturen untersucht, um einen Ansatz für die direkte Proteinsequenzierung mittels AFM und spitzenverstärkter Raman-Streuung (TERS) zu entwickeln. Da die Bildung und der Abbau amyloidogenen Strukturen noch immer nicht vollständig verstanden ist, konzentrierte sich die zweite Studie auf das Verhalten von Amyloid-Fibrillen in Lösungen mit unterschiedlichen pH-Werten. Schließlich befasste sich die letzte Studie mit der Identifizierung von Proteinen in der komplexen Umgebung der Virusoberfläche auf dem Weg zur Klassifizierung von Virenstämmen anhand ihres morphologischen und chemischen Fingerabdrucks.

Zur Charakterisierung der Primärstruktur musste die native Peptidstruktur zunächst entfaltet und sichergestellt werden, dass keine Rückfaltung stattfindet. Zu diesem Zweck wurden Addukte aus einem kurzen Peptid, das aus 14 Aminosäuren und 4-Bipyridin-Molekülen besteht, hergestellt. Die Topographie der hergestellten fadenförmigen Strukturen wurde mit einem AFM abgebildet und TERS wurde verwendet, um die einzelnen Bausteine auf der Oberfläche der Fäden zu erkennen. Obwohl die Fäden aus mehreren Schichten zusammengesetzt waren, konnten die verschiedenen Aminosäuren identifiziert und von den Bipyridylresten unterschieden werden. Es stellte sich heraus, dass die Streckung und Trennung der Peptid-Bipyridin-Addukte ein großes Hindernis für die Untersuchungen im Nanomaßstab darstellten. Dennoch bestätigten die Ergebnisse die theoretisch vorhergesagte Bindung des Bipyridyls an den N- oder C-Terminus des Peptids.

In der zweiten Studie wurde die sekundäre Struktur in Insulin-Amyloidfibrillen mithilfe von AFM und oberflächenverstärkter Raman-Streuung (SERS) untersucht. In den Experimenten wurde eine Fibrillendissoziation durch Suspendieren der Probe in Lösungen mit unterschiedlichem pH-Wert ausgelöst. Die AFM-Topografien zeigten bereits den Abbau der mikrometerlangen Fibrillen durch die Bildung von unstrukturierten Aggregaten. Es wurde festgestellt, dass sich die Amyloidfibrillen mit zunehmendem pH-Wert allmählich auflösen, und dieser dynamische Prozess konnte in situ durch zeitabhängige Messungen verfolgt werden. Dieser allmähliche Abbau war auch an einer Veränderung der sekundären Struktur der Fibrillen erkennbar, wie die SERS-Ergebnisse zeigten. Durch Untersuchung der Raman-Marker-Banden der Peptid-Sekundärstruktur, nämlich des Amids I, konnte gezeigt werden, dass der Anteil der ursprünglich vorherrschenden β-Sheet-Struktur zugunsten von α-Helix und Random-Coil-Strukturen abnahm. Die Ergebnisse werfen ein neues Licht auf das Verhalten von Insulin-Amyloidfibrillen und vertiefen das Verständnis dieser potenziell pathogenen Spezies.

Schließlich wurde ein AFM in Kombination mit Fluoreszenzmikroskopie und TERS eingesetzt, um SARS-CoV-2-Partikel zu identifizieren und die Proteinstruktur auf der komplexen Virusoberfläche zu untersuchen. In einem ersten Schritt wurde die Morphologie der Viren charakterisiert, von einer Antikörper-Markierung gefolgt. Durch die Verwendung speziell strukturierter Substrate war es möglich, die mit dem AFM charakterisierten Partikel in den anschließenden Fluoreszenzmessungen wiederzuentdecken. Dieser komplementäre Ansatz ermöglichte die eindeutige Identifizierung und Unterscheidung der Viren von anderem Probenmaterial.

Schließlich wurde TERS eingesetzt, um chemische Informationen von der Oberfläche des Virus zu erhalten. Die Spektren ermöglichten eine vorläufige Unterscheidung der verschiedenen Untereinheiten des Spike-Proteins. Neben der Identifizierung von Proteinen wurden auch Lipide und Nukleinsäuren auf den Virusoberflächen nachgewiesen. Es ist zu erwarten, dass die Kombination von Techniken, wie sie in der vorliegenden Arbeit angewandt wurde, für den Nachweis und die Charakterisierung von SARS-CoV-2 und anderen Viren in Zukunft sehr nützlich sein wird.

Die Ergebnisse dieser Arbeit zeigen, dass AFM und plasmonenverstärkte Raman-Spektroskopie bzw. die Kombination beider Methoden eine Charakterisierung von proteinhaltigen Proben ermöglichen, die mit anderen Methoden (z. B. Röntgenkristallografie, Kernspinresonanz und Elektronenmikroskopie) nicht direkt charakterisieren kann. Die herausragenden Nachweisfähigkeiten von TERS mit hoher Sensitivität und hoher Auflösung ohne die Notwendigkeit von Markierungen stellen ein wertvolles Instrument zur Analyse von Proteinstrukturen auf verschiedenen Ebenen dar. Mit dem vorgestellten Ansatz sollte es möglich sein, die Primärstruktur (Sequenz) von Peptiden zugänglich zu machen. Des Weiteren können wertvolle Informationen über die Anordnung der Peptidketten auf der Nanometerskala aus der Sekundärstruktur gewonnen werden. Schließlich eröffnet die Möglichkeit zur Charakterisierung von Proteinen in einer komplexen Umgebung mit anderen Biopolymeren wie Lipiden und Nukleinsäuren vielfältige analytische Möglichkeiten.

REFERENCES

1. Peter J. Kennelly, et al., *Harper's Illustrated Biochemistry, Thirty-Second Edition.pdf*. 32 ed. 2023: McGraw Hill, LLC.
2. Buxbaum, E., *Fundamentals of Protein Structure and Function*. 2 ed. 2015: Springer Cham. XVI, 521.
3. Jung, J.W. and W. Lee, *Structure-based functional discovery of proteins: structural proteomics.* J Biochem Mol Biol, 2004. **37**(1): p. 28-34.
4. Wang, H.W. and J.W. Wang, *How cryo-electron microscopy and X-ray crystallography complement each other.* Protein Sci, 2017. **26**(1): p. 32-39.
5. Zheng, H., et al., *X-ray crystallography over the past decade for novel drug discovery - where are we heading next?* Expert Opin Drug Discov, 2015. **10**(9): p. 975-89.
6. Shin, J., W. Lee, and W. Lee, *Structural proteomics by NMR spectroscopy.* Expert Rev Proteomics, 2008. **5**(4): p. 589-601.
7. Takeuchi, K., K. Baskaran, and H. Arthanari, *Structure determination using solution NMR: Is it worth the effort?* J Magn Reson, 2019. **306**: p. 195-201.
8. Carroni, M. and H.R. Saibil, *Cryo electron microscopy to determine the structure of macromolecular complexes.* Methods, 2016. **95**: p. 78-85.
9. Franz Josef Giessibl, F.J.G., *Atomic Force Microscopy in Ultrahigh Vacuum.* Japanese Journal of Applied Physics, 1994. **33**(6S).
10. Joshi, J., S.V. Homburg, and A. Ehrmann, *Atomic Force Microscopy (AFM) on Biopolymers and Hydrogels for Biotechnological Applications-Possibilities and Limits.* Polymers (Basel), 2022. **14**(6).
11. Raman, C.V. and K.S. Krishnan, *A New Type of Secondary Radiation.* Nature, 1928. **121**(3048): p. 501-502.
12. Dodo, K., K. Fujita, and M. Sodeoka, *Raman Spectroscopy for Chemical Biology Research.* J Am Chem Soc, 2022. **144**(43): p. 19651-19667.
13. Allakhverdiev, E.S., et al., *Raman Spectroscopy and Its Modifications Applied to Biological and Medical Research.* Cells, 2022. **11**(3).
14. Bruce Alberts, A.J., Julian Lewis, David Morgan, Martin Raff, Keith Roberts, Peter Walter *Molecular Biology of the Cell.* 6th Edition ed. 2014: Garland Science.
15. Urry, L.A., et al., *Campbell Biology, 12th edition*. 2021, New York: Pearson.
16. Dietzen, D.J., *Amino Acids, Peptides, and Proteins*, in *Principles and Applications of Molecular Diagnostics*. 2018. p. 345-380.
17. Ramirez Hernandez, E., et al., *The Role of the SARS-CoV-2 S-Protein Glycosylation in the Interaction of SARS-CoV-2/ACE2 and Immunological Responses.* Viral Immunol, 2021. **34**(3): p. 165-173.
18. Langel, U., et al., *Introduction to Peptides and Proteins*. 2009: CRC Press.
19. Wang, L., et al., *Therapeutic peptides: current applications and future directions.* Signal Transduct Target Ther, 2022. **7**(1): p. 48.
20. Trivedi, M.V., J.S. Laurence, and T.J. Siahaan, *The role of thiols and disulfides on protein stability.* Curr Protein Pept Sci, 2009. **10**(6): p. 614-25.
21. Chothia, C., *Principles that determine the structure of proteins.* Annu Rev Biochem, 1984. **53**: p. 537-72.
22. Gross, M., *Proteins that convert from alpha helix to beta sheet: implications for folding and disease.* Curr Protein Pept Sci, 2000. **1**(4): p. 339-47.

23. Jing, X., et al., *Amino Acid Encoding Methods for Protein Sequences: A Comprehensive Review and Assessment.* IEEE/ACM Trans Comput Biol Bioinform, 2020. **17**(6): p. 1918-1931.
24. Whisstock, J.C. and A.M. Lesk, *Prediction of protein function from protein sequence and structure.* Q Rev Biophys, 2003. **36**(3): p. 307-40.
25. Einsteinium, T. *Twenty-one proteinogenic α-amino acids shown in their zwitterionic forms with side chain protonation states determined at physiological pH of 7.4.* 2022; Available from: https://commons.wikimedia.org/wiki/File:ProteinogenicAminoAcids.svg.
26. Gorbalenya, A.E. and C. Lauber, *Bioinformatics of virus taxonomy: foundations and tools for developing sequence-based hierarchical classification.* Curr Opin Virol, 2022. **52**: p. 48-56.
27. Flint, J., et al., *Principles of Virology, Multi-Volume, 5th Edition*. 2020: ASM Press.
28. Ennaji, M.M., *EMERGING AND REEMERGING VIRAL PATHOGENS*. 2020, United Kingdom: Academic Press.
29. Mejia-Mendez, J.L., et al., *Virus-like Particles: Fundamentals and Biomedical Applications.* Int J Mol Sci, 2022. **23**(15).
30. Harrison, S.C., *Mechanism of Membrane Fusion by Viral Envelope Proteins*, in *Virus Structure and Assembly*. 2005. p. 231-261.
31. Wisskirchen, K., et al., *New pharmacological strategies to fight enveloped viruses.* Trends Pharmacol Sci, 2014. **35**(9): p. 470-8.
32. Spriggs, C.C., M.C. Harwood, and B. Tsai, *How non-enveloped viruses hijack host machineries to cause infection.* Adv Virus Res, 2019. **104**: p. 97-122.
33. Owusu, I.A., et al., *Egress of non-enveloped enteric RNA viruses.* J Gen Virol, 2021. **102**(3).
34. Colm, G. *Simplified diagram of the structure of viruses*. 2008; Available from: https://commons.wikimedia.org/wiki/File:Virus_structure_simple.png.
35. Splettstoesser, T. *Diagram of the HIV virion*. 2014; Available from: https://commons.wikimedia.org/wiki/File:HI-virion-structure_en.svg.
36. Horowitz, E.D., et al., *Biophysical and ultrastructural characterization of adeno-associated virus capsid uncoating and genome release.* J Virol, 2013. **87**(6): p. 2994-3002.
37. Aherfi, S., et al., *Giant Viruses of Amoebas: An Update.* Front Microbiol, 2016. **7**: p. 349.
38. Nigel J. Dimmock, Andrew J. Easton, and K.N. Leppard, *ntroduction to Modern Virology*. 7th ed. 2016: Wiley-Blackwell.
39. Weigelt, J., et al., *Structural genomics and drug discovery: all in the family.* Curr Opin Chem Biol, 2008. **12**(1): p. 32-9.
40. Abbe, E., *Beiträge zur Theorie des Mikroskops und der mikroskopischen Wahrnehmung.* Archiv für Mikroskopische Anatomie, 1873. **9**(1): p. 413-468.
41. Gray, N., *Knowing the limit.* Nature Cell Biology, 2009. **11**(S1): p. S8-S8.
42. Takayanagi, K., et al., *Electron microscopy at a sub-50 pm resolution.* J Electron Microsc (Tokyo), 2011. **60 Suppl 1**: p. S239-44.
43. Morishita, S., et al., *Attainment of 40.5 pm spatial resolution using 300 kV scanning transmission electron microscope equipped with fifth-order aberration corrector.* Microscopy (Oxf), 2018. **67**(1): p. 46-50.
44. Miranda, K., et al., *Three dimensional reconstruction by electron microscopy in the life sciences: An introduction for cell and tissue biologists.* Mol Reprod Dev, 2015. **82**(7-8): p. 530-47.

45. Costa, T.R.D., A. Ignatiou, and E.V. Orlova, *Structural Analysis of Protein Complexes by Cryo Electron Microscopy.* Methods Mol Biol, 2017. **1615**: p. 377-413.
46. Liu, C., et al., *The Architecture of Inactivated SARS-CoV-2 with Postfusion Spikes Revealed by Cryo-EM and Cryo-ET.* Structure, 2020. **28**(11): p. 1218-1224 e4.
47. Wrapp, D., et al., *Cryo-EM structure of the 2019-nCoV spike in the prefusion conformation.* Science, 2020. **367**(6483): p. 1260-1263.
48. Venien-Bryan, C., et al., *Cryo-electron microscopy and X-ray crystallography: complementary approaches to structural biology and drug discovery.* Acta Crystallogr F Struct Biol Commun, 2017. **73**(Pt 4): p. 174-183.
49. Bian, K., et al., *Scanning probe microscopy.* Nature Reviews Methods Primers, 2021. **1**(1).
50. Gross, L., *Recent advances in submolecular resolution with scanning probe microscopy.* Nat Chem, 2011. **3**(4): p. 273-8.
51. Poggi, M.A., et al., *Scanning probe microscopy.* Anal Chem, 2004. **76**(12): p. 3429-43.
52. Binnig, G., et al., *Surface Studies by Scanning Tunneling Microscopy.* Physical Review Letters, 1982. **49**(1): p. 57-61.
53. Binnig, G. and H. Rohrer, *Scanning tunneling microscopy.* Surface Science, 1983. **126**(1-3): p. 236-244.
54. Binnig, G., C.F. Quate, and C. Gerber, *Atomic force microscope.* Phys Rev Lett, 1986. **56**(9): p. 930-933.
55. Seo, Y. and W. Jhe, *Atomic force microscopy and spectroscopy.* Reports on Progress in Physics, 2008. **71**(1).
56. Dufrene, Y.F., *Atomic force microscopy, a powerful tool in microbiology.* J Bacteriol, 2002. **184**(19): p. 5205-13.
57. Shao, Z., et al., *Biological atomic force microscopy: what is achieved and what is needed.* Advances in Physics, 1996. **45**(1): p. 1-86.
58. Allison, D.P., et al., *Atomic force microscopy of biological samples.* Wiley Interdiscip Rev Nanomed Nanobiotechnol, 2010. **2**(6): p. 618-34.
59. Peter Eaton and P. West, *Atomic Force Microscopy*. 2010: Oxford University Press, USA.
60. Xu, K., et al., *Recent development of PeakForce Tapping mode atomic force microscopy and its applications on nanoscience.* Nanotechnology Reviews, 2018. **7**(6): p. 605-621.
61. Moraille, P., et al., *Experimental methods in chemical engineering: Atomic force microscopy − AFM.* The Canadian Journal of Chemical Engineering, 2022. **100**(10): p. 2778-2806.
62. Hu, J., et al., *Review on the applications of atomic force microscopy imaging in proteins.* Micron, 2022. **159**: p. 103293.
63. Das, R.S. and Y.K. Agrawal, *Raman spectroscopy: Recent advancements, techniques and applications.* Vibrational Spectroscopy, 2011. **57**(2): p. 163-176.
64. Hanlon, E.B., et al., *Prospects for in vivo Raman spectroscopy.* Phys Med Biol, 2000. **45**(2): p. R1-59.
65. Tu, A.T., *Raman spectroscopy in biology : principles and applications*. 1982, New York: Wiley.

66. Wang, X., et al., *Fundamental understanding and applications of plasmon-enhanced Raman spectroscopy.* Nature Reviews Physics, 2020. **2**(5): p. 253-271.
67. Bunaciu, A.A., H.Y. Aboul-Enein, and Ş. Fleschin, *Vibrational Spectroscopy in Clinical Analysis.* Applied Spectroscopy Reviews, 2014. **50**(2): p. 176-191.
68. Mulvaney, S.P. and C.D. Keating, *Raman spectroscopy.* Anal Chem, 2000. **72**(12): p. 145R-157R.
69. Cordero, E., et al., *In-vivo Raman spectroscopy: from basics to applications.* J Biomed Opt, 2018. **23**(7): p. 1-23.
70. Fleischmann, M., P.J. Hendra, and A.J. McQuillan, *Raman spectra of pyridine adsorbed at a silver electrode.* Chemical Physics Letters, 1974. **26**(2): p. 163-166.
71. Jeanmaire, D.L. and R.P. Van Duyne, *Surface raman spectroelectrochemistry.* Journal of Electroanalytical Chemistry and Interfacial Electrochemistry, 1977. **84**(1): p. 1-20.
72. Creighton, J.A., *Surface raman electromagnetic enhancement factors for molecules at the surface of small isolated metal spheres: The determination of adsorbate orientation from sers relative intensities.* Surface Science, 1983. **124**(1): p. 209-219.
73. Zong, C., et al., *Surface-Enhanced Raman Spectroscopy for Bioanalysis: Reliability and Challenges.* Chem Rev, 2018. **118**(10): p. 4946-4980.
74. Unser, S., et al., *Localized Surface Plasmon Resonance Biosensing: Current Challenges and Approaches.* Sensors (Basel), 2015. **15**(7): p. 15684-716.
75. Mayer, K.M. and J.H. Hafner, *Localized surface plasmon resonance sensors.* Chem Rev, 2011. **111**(6): p. 3828-57.
76. Deckert-Gaudig, T., et al., *Tip-enhanced Raman spectroscopy - from early developments to recent advances.* Chem Soc Rev, 2017. **46**(13): p. 4077-4110.
77. Cai, L., et al., *Label-Free Surface-Enhanced Raman Spectroscopic Analysis of Proteins: Advances and Applications.* Int J Mol Sci, 2022. **23**(22).
78. Ding, S.-Y., et al., *Nanostructure-based plasmon-enhanced Raman spectroscopy for surface analysis of materials.* Nature Reviews Materials, 2016. **1**(6).
79. Le Ru, E.C., et al., *Surface Enhanced Raman Scattering Enhancement Factors: A Comprehensive Study.* The Journal of Physical Chemistry C, 2007. **111**(37): p. 13794-13803.
80. Han, X.X., et al., *Surface-enhanced Raman spectroscopy.* Nature Reviews Methods Primers, 2022. **1**(1).
81. Bonhommeau, S., G.S. Cooney, and Y. Huang, *Nanoscale chemical characterization of biomolecules using tip-enhanced Raman spectroscopy.* Chem Soc Rev, 2022. **51**(7): p. 2416-2430.
82. Mahapatra, S., et al., *Tip-enhanced Raman spectroscopy: Chemical analysis with nanoscale to angstrom scale resolution.* J Chem Phys, 2020. **153**(1): p. 010902.
83. Anderson, M.S., *Locally enhanced Raman spectroscopy with an atomic force microscope.* Appl. Phys. Lett, 2000. **76**(21): p. 3130–3132.
84. Hayazawa, N., et al., *Metallized tip amplification of near-field Raman scattering.* Optics Communications, 2000. **183**(1-4): p. 333-336.
85. Pettinger, B., et al., *Surface Enhanced Raman Spectroscopy: Towards Single Molecule Spectroscopy.* Electrochemistry, 2000. **68**(12): p. 942-949.

86. Stöckle, R.M., et al., *Nanoscale chemical analysis by tip-enhanced Raman spectroscopy.* Chemical Physics Letters, 2000. **318**(1-3): p. 131-136.
87. Kelly, K.L., et al., *The Optical Properties of Metal Nanoparticles: The Influence of Size, Shape, and Dielectric Environment.* The Journal of Physical Chemistry B, 2002. **107**(3): p. 668-677.
88. Cao, Y. and M. Sun, *Tip-enhanced Raman spectroscopy.* Reviews in Physics, 2022. **8**.
89. Chen, C., N. Hayazawa, and S. Kawata, *A 1.7 nm resolution chemical analysis of carbon nanotubes by tip-enhanced Raman imaging in the ambient.* Nat Commun, 2014. **5**: p. 3312.
90. Deckert-Gaudig, T., E. Kammer, and V. Deckert, *Tracking of nanoscale structural variations on a single amyloid fibril with tip-enhanced Raman scattering.* J Biophotonics, 2012. **5**(3): p. 215-9.
91. Jiang, S., et al., *Distinguishing adjacent molecules on a surface using plasmon-enhanced Raman scattering.* Nat Nanotechnol, 2015. **10**(10): p. 865-9.
92. Zhang, R., et al., *Chemical mapping of a single molecule by plasmon-enhanced Raman scattering.* Nature, 2013. **498**(7452): p. 82-6.
93. Trautmann, S., et al., *A classical description of subnanometer resolution by atomic features in metallic structures.* Nanoscale, 2017. **9**(1): p. 391-401.
94. Richard-Lacroix, M. and V. Deckert, *Direct molecular-level near-field plasmon and temperature assessment in a single plasmonic hotspot.* Light Sci Appl, 2020. **9**: p. 35.
95. Moretti, M., et al., *Reflection-mode TERS on Insulin Amyloid Fibrils with Top-Visual AFM Probes.* Plasmonics, 2013. **8**(1): p. 25-33.
96. Nicklaus, M., et al., *Note: tip enhanced Raman spectroscopy with objective scanner on opaque samples.* Rev Sci Instrum, 2012. **83**(6): p. 066102.
97. Langeluddecke, L., P. Singh, and V. Deckert, *Exploring the Nanoscale: Fifteen Years of Tip-Enhanced Raman Spectroscopy.* Appl Spectrosc, 2015. **69**(12): p. 1357-71.
98. Stadler, J., T. Schmid, and R. Zenobi, *Nanoscale chemical imaging using top-illumination tip-enhanced Raman spectroscopy.* Nano Lett, 2010. **10**(11): p. 4514-20.
99. Elbasuney, S. and A.F. El-Sherif, *Complete spectroscopic picture of concealed explosives: Laser induced Raman versus infrared.* TrAC Trends in Analytical Chemistry, 2016. **85**: p. 34-41.
100. Berweger, S. and M.B. Raschke, *Polar phonon mode selection rules in tip-enhanced Raman scattering.* Journal of Raman Spectroscopy, 2009. **40**(10): p. 1413-1419.
101. Kim, J., J.U. Lee, and H. Cheong, *Polarized Raman spectroscopy for studying two-dimensional materials.* J Phys Condens Matter, 2020. **32**(34): p. 343001.
102. Shao, F. and R. Zenobi, *Tip-enhanced Raman spectroscopy: principles, practice, and applications to nanospectroscopic imaging of 2D materials.* Anal Bioanal Chem, 2019. **411**(1): p. 37-61.
103. Neacsu, C.C., S. Berweger, and M.B. Raschke, *Tip-Enhanced Raman Imaging and Nanospectroscopy: Sensitivity, Symmetry, and Selection Rules.* NanoBiotechnology, 2009. **3**(3-4): p. 172-196.
104. Wang, X., et al., *Tip-enhanced Raman spectroscopy for surfaces and interfaces.* Chem Soc Rev, 2017. **46**(13): p. 4020-4041.

105. Schmid, T., et al., *Nanoscale chemical imaging using tip-enhanced Raman spectroscopy: a critical review.* Angew Chem Int Ed Engl, 2013. **52**(23): p. 5940-54.
106. Umakoshi, T., et al., *Tip-enhanced Raman spectroscopy with amplitude-controlled tapping-mode AFM.* Sci Rep, 2022. **12**(1): p. 12776.
107. Liao, M., et al., *Tip-Enhanced Raman Spectroscopic Imaging of Individual Carbon Nanotubes with Subnanometer Resolution.* Nano Lett, 2016. **16**(7): p. 4040-6.
108. He, Z., et al., *Tip-Enhanced Raman Imaging of Single-Stranded DNA with Single Base Resolution.* J Am Chem Soc, 2019. **141**(2): p. 753-757.
109. He, Z., et al., *Resolving the Sequence of RNA Strands by Tip-Enhanced Raman Spectroscopy.* ACS Photonics, 2020. **8**(2): p. 424-430.
110. Deckert-Gaudig, T., et al., *Spatially resolved spectroscopic differentiation of hydrophilic and hydrophobic domains on individual insulin amyloid fibrils.* Sci Rep, 2016. **6**: p. 33575.
111. Lipiec, E., et al., *Nanoscale Hyperspectral Imaging of Amyloid Secondary Structures in Liquid.* Angew Chem Int Ed Engl, 2021. **60**(9): p. 4545-4550.
112. Dou, T., et al., *Nanoscale Structural Characterization of Individual Viral Particles Using Atomic Force Microscopy Infrared Spectroscopy (AFM-IR) and Tip-Enhanced Raman Spectroscopy (TERS).* Anal Chem, 2020. **92**(16): p. 11297-11304.
113. Rao, V.S., et al., *Protein-protein interaction detection: methods and analysis.* Int J Proteomics, 2014. **2014**: p. 147648.
114. Büyükköroğlu, G., et al., *Techniques for Protein Analysis*, in *Omics Technologies and Bio-Engineering*. 2018. p. 317-351.
115. Edman, P., et al., *Method for Determination of the Amino Acid Sequence in Peptides.* Acta Chemica Scandinavica, 1950. **4**: p. 283-293.
116. Steen, H. and M. Mann, *The ABC's (and XYZ's) of peptide sequencing.* Nat Rev Mol Cell Biol, 2004. **5**(9): p. 699-711.
117. Alfaro, J.A., et al., *The emerging landscape of single-molecule protein sequencing technologies.* Nat Methods, 2021. **18**(6): p. 604-617.
118. Swaminathan, J., et al., *Highly parallel single-molecule identification of proteins in zeptomole-scale mixtures.* Nat Biotechnol, 2018.
119. Tyers, M. and M. Mann, *From genomics to proteomics.* Nature, 2003. **422**(6928): p. 193-7.
120. Hu, Z.L., et al., *Biological Nanopore Approach for Single-Molecule Protein Sequencing.* Angew Chem Int Ed Engl, 2021. **60**(27): p. 14738-14749.
121. Archakov, A.I., et al., *AFM fishing nanotechnology is the way to reverse the Avogadro number in proteomics.* Proteomics, 2007. **7**(1): p. 4-9.
122. Deamer, D., M. Akeson, and D. Branton, *Three decades of nanopore sequencing.* Nature Biotechnology, 2016. **34**(5): p. 518-524.
123. Afshar Bakshloo, M., et al., *Nanopore-Based Protein Identification.* J Am Chem Soc, 2022. **144**(6): p. 2716-2725.
124. Brinkerhoff, H., et al., *Multiple rereads of single proteins at single-amino acid resolution using nanopores.* Science, 2021. **374**(6574): p. 1509-1513.
125. Deckert, V., et al., *Spatial resolution in Raman spectroscopy.* Faraday Discuss, 2015. **177**: p. 9-20.
126. Liu, L., et al., *A self-assembled nanopatch with peptide-organic multilayers and mechanical properties.* Nanoscale, 2015. **7**(6): p. 2250-4.

127. Bhagavan, N.V. and C.-E. Ha, *Three-Dimensional Structure of Proteins and Disorders of Protein Misfolding*, in *Essentials of Medical Biochemistry*. 2015. p. 31-51.
128. Zhang, Y., et al., *Probing Adsorption Configurations of Small Molecules on Surfaces by Single-Molecule Tip-Enhanced Raman Spectroscopy.* Chemphyschem, 2019. **20**(1): p. 37-41.
129. Zhu, G., et al., *Raman spectra of amino acids and their aqueous solutions.* Spectrochim Acta A Mol Biomol Spectrosc, 2011. **78**(3): p. 1187-95.
130. Uzunbajakava, N., et al., *Nonresonant confocal Raman imaging of DNA and protein distribution in apoptotic cells.* Biophys J, 2003. **84**(6): p. 3968-81.
131. Deckert-Gaudig, T., E. Rauls, and V. Deckert, *Aromatic Amino Acid Monolayers Sandwiched between Gold and Silver: A Combined Tip-Enhanced Raman and Theoretical Approach.* The Journal of Physical Chemistry C, 2009. **114**(16): p. 7412-7420.
132. Jiang, S., et al., *Bicomponent supramolecular self‐assemblies studied with tip‐enhanced Raman spectroscopy.* Journal of Raman Spectroscopy, 2020. **52**(2): p. 366-374.
133. Hernandez, B., et al., *Vibrational analysis of amino acids and short peptides in hydrated media. VIII. Amino acids with aromatic side chains: L-phenylalanine, L-tyrosine, and L-tryptophan.* J Phys Chem B, 2010. **114**(46): p. 15319-30.
134. Socrates, G., *Infrared and Raman Characteristic Group Frequencies: Tables and Charts*. 2004: Wiley.
135. Darussalam, E.Y., et al., *pH-dependent disintegration of insulin amyloid fibrils monitored with atomic force microscopy and surface-enhanced Raman spectroscopy.* Spectrochim Acta A Mol Biomol Spectrosc, 2021. **256**: p. 119672.
136. Chiti, F. and C.M. Dobson, *Protein Misfolding, Amyloid Formation, and Human Disease: A Summary of Progress Over the Last Decade.* Annu Rev Biochem, 2017. **86**: p. 27-68.
137. Eisenberg, D.S. and M.R. Sawaya, *Structural Studies of Amyloid Proteins at the Molecular Level.* Annu Rev Biochem, 2017. **86**: p. 69-95.
138. Malgieri, G., et al., *Folding mechanisms steer the amyloid fibril formation propensity of highly homologous proteins.* Chem Sci, 2018. **9**(13): p. 3290-3298.
139. Owen, M.C., et al., *Effects of in vivo conditions on amyloid aggregation.* Chem Soc Rev, 2019. **48**(14): p. 3946-3996.
140. Riek, R. and D.S. Eisenberg, *The activities of amyloids from a structural perspective.* Nature, 2016. **539**(7628): p. 227-235.
141. Knowles, T.P., et al., *Role of intermolecular forces in defining material properties of protein nanofibrils.* Science, 2007. **318**(5858): p. 1900-3.
142. Makin, O.S., et al., *Molecular basis for amyloid fibril formation and stability.* Proc Natl Acad Sci U S A, 2005. **102**(2): p. 315-20.
143. Nelson, R., et al., *Structure of the cross-beta spine of amyloid-like fibrils.* Nature, 2005. **435**(7043): p. 773-8.
144. Sawaya, M.R., et al., *Atomic structures of amyloid cross-beta spines reveal varied steric zippers.* Nature, 2007. **447**(7143): p. 453-7.
145. Chiti, F. and C.M. Dobson, *Protein misfolding, functional amyloid, and human disease.* Annu Rev Biochem, 2006. **75**: p. 333-66.

146. Iadanza, M.G., et al., *A new era for understanding amyloid structures and disease.* Nat Rev Mol Cell Biol, 2018. **19**(12): p. 755-773.
147. Zapadka, K.L., et al., *Factors affecting the physical stability (aggregation) of peptide therapeutics.* Interface Focus, 2017. **7**(6): p. 20170030.
148. Bernson, D., et al., *Amyloid formation of bovine insulin is retarded in moderately acidic pH and by addition of short-chain alcohols.* Eur Biophys J, 2020. **49**(2): p. 145-153.
149. Kurouski, D., et al., *Direct observation and pH control of reversed supramolecular chirality in insulin fibrils by vibrational circular dichroism.* Chem Commun (Camb), 2010. **46**(38): p. 7154-6.
150. Malisauskas, M., et al., *Lability landscape and protease resistance of human insulin amyloid: a new insight into its molecular properties.* J Mol Biol, 2010. **396**(1): p. 60-74.
151. Noormagi, A., et al., *Insulin Fibrillization at Acidic and Physiological pH Values is Controlled by Different Molecular Mechanisms.* Protein J, 2015. **34**(6): p. 398-403.
152. Smirnova, E., et al., *pH-responsive modulation of insulin aggregation and structural transformation of the aggregates.* Biochimie, 2015. **109**: p. 49-59.
153. Sneideris, T., et al., *pH-Driven Polymorphism of Insulin Amyloid-Like Fibrils.* PLoS One, 2015. **10**(8): p. e0136602.
154. Santangelo, M.G., et al., *Back to the oligomeric state: pH-induced dissolution of concanavalin A amyloid-like fibrils into non-native oligomers.* RSC Advances, 2016. **6**(79): p. 75082-75091.
155. Shammas, S.L., et al., *Perturbation of the stability of amyloid fibrils through alteration of electrostatic interactions.* Biophys J, 2011. **100**(11): p. 2783-91.
156. Kurouski, D., et al., *Disulfide bridges remain intact while native insulin converts into amyloid fibrils.* PLoS One, 2012. **7**(6): p. e36989.
157. Domigan, L.J., et al., *Controlling the dimensions of amyloid fibrils: toward homogenous components for bionanotechnology.* Biopolymers, 2012. **97**(2): p. 123-33.
158. Foderà, V., M. van de Weert, and B. Vestergaard, *Large-scale polymorphism and auto-catalytic effect in insulin fibrillogenesis.* Soft Matter, 2010. **6**(18).
159. Jansen, R., W. Dzwolak, and R. Winter, *Amyloidogenic self-assembly of insulin aggregates probed by high resolution atomic force microscopy.* Biophys J, 2005. **88**(2): p. 1344-53.
160. Nielsen, L., et al., *Effect of environmental factors on the kinetics of insulin fibril formation: elucidation of the molecular mechanism.* Biochemistry, 2001. **40**(20): p. 6036-46.
161. Gosal, W.S., et al., *Amyloid under the atomic force microscope.* Protein Pept Lett, 2006. **13**(3): p. 261-70.
162. Hoyer, W., et al., *Rapid self-assembly of alpha-synuclein observed by in situ atomic force microscopy.* J Mol Biol, 2004. **340**(1): p. 127-39.
163. Lee, W., et al., *Advances in AFM Imaging Applications for Characterizing the Biophysical Properties of Amyloid Fibrils*, in *Exploring New Findings on Amyloidosis*. 2016.
164. Li, Y., et al., *Characterization of Inter- and Intramolecular Interactions of Amyloid Fibrils by AFM-Based Single-Molecule Force Spectroscopy.* Journal of Nanomaterials, 2016. **2016**: p. 1-18.

165. Bouchard, M., et al., *Formation of insulin amyloid fibrils followed by FTIR simultaneously with CD and electron microscopy.* Protein Sci, 2000. **9**(10): p. 1960-7.
166. Kurouski, D., R.P. Van Duyne, and I.K. Lednev, *Exploring the structure and formation mechanism of amyloid fibrils by Raman spectroscopy: a review.* Analyst, 2015. **140**(15): p. 4967-80.
167. Ma, S., et al., *Vibrational circular dichroism shows unusual sensitivity to protein fibril formation and development in solution.* J Am Chem Soc, 2007. **129**(41): p. 12364-5.
168. Ortiz, C., et al., *Analysis of insulin amyloid fibrils by Raman spectroscopy.* Biophys Chem, 2007. **128**(2-3): p. 150-5.
169. Bonhommeau, S., et al., *Tip-Enhanced Raman Spectroscopy to Distinguish Toxic Oligomers from Abeta1-42 Fibrils at the Nanometer Scale.* Angew Chem Int Ed Engl, 2017. **56**(7): p. 1771-1774.
170. Kurouski, D., et al., *Infrared and Raman chemical imaging and spectroscopy at the nanoscale.* Chem Soc Rev, 2020. **49**(11): p. 3315-3347.
171. Rizevsky, S. and D. Kurouski, *Nanoscale Structural Organization of Insulin Fibril Polymorphs Revealed by Atomic Force Microscopy-Infrared Spectroscopy (AFM-IR).* Chembiochem, 2020. **21**(4): p. 481-485.
172. Halas, N.J., et al., *Plasmons in strongly coupled metallic nanostructures.* Chem Rev, 2011. **111**(6): p. 3913-61.
173. Otto, A., et al., *Surface-enhanced Raman scattering.* Journal of Physics: Condensed Matter, 1992. **4**(5): p. 1143-1212.
174. Willets, K.A. and R.P. Van Duyne, *Localized surface plasmon resonance spectroscopy and sensing.* Annu Rev Phys Chem, 2007. **58**: p. 267-97.
175. Devitt, G., et al., *Raman Spectroscopy: An Emerging Tool in Neurodegenerative Disease Research and Diagnosis.* ACS Chem Neurosci, 2018. **9**(3): p. 404-420.
176. Sinha, S.S., et al., *Nanoarchitecture Based SERS for Biomolecular Fingerprinting and Label-Free Disease Markers Diagnosis.* Acc Chem Res, 2016. **49**(12): p. 2725-2735.
177. Leopold, N. and B. Lendl, *A New Method for Fast Preparation of Highly Surface-Enhanced Raman Scattering (SERS) Active Silver Colloids at Room Temperature by Reduction of Silver Nitrate with Hydroxylamine Hydrochloride.* The Journal of Physical Chemistry B, 2003. **107**(24): p. 5723-5727.
178. Kurouski, D., et al., *Normal and reversed supramolecular chirality of insulin fibrils probed by vibrational circular dichroism at the protofilament level of fibril structure.* Biophys J, 2012. **103**(3): p. 522-531.
179. Manno, M., et al., *Kinetics of different processes in human insulin amyloid formation.* J Mol Biol, 2007. **366**(1): p. 258-74.
180. Müller, D.J., et al., *Electrostatically Balanced Subnanometer Imaging of Biological Specimens by Atomic Force Microscope.* Biophysical Journal, 1999. **76**(2): p. 1101-1111.
181. Gołek, F., et al., *AFM image artifacts.* Applied Surface Science, 2014. **304**: p. 11-19.
182. Kurouski, D., et al., *Amide I vibrational mode suppression in surface (SERS) and tip (TERS) enhanced Raman spectra of protein specimens.* Analyst, 2013. **138**(6): p. 1665-73.

183. Diaz Fleming, G., et al., *Experimental and theoretical Raman and surface-enhanced Raman scattering study of cysteine.* Journal of Raman Spectroscopy, 2009. **40**(6): p. 632-638.
184. Bido, A.T., et al., *High-Speed Fluctuations in Surface-Enhanced Raman Scattering Intensities from Various Nanostructures.* Appl Spectrosc, 2020. **74**(11): p. 1398-1406.
185. Perez-Jimenez, A.I., et al., *Surface-enhanced Raman spectroscopy: benefits, trade-offs and future developments.* Chem Sci, 2020. **11**(18): p. 4563-4577.
186. Kurouski, D., et al., *Structure and composition of insulin fibril surfaces probed by TERS.* J Am Chem Soc, 2012. **134**(32): p. 13323-9.
187. Kurouski, D., et al., *Surface characterization of insulin protofilaments and fibril polymorphs using tip-enhanced Raman spectroscopy (TERS).* Biophys J, 2014. **106**(1): p. 263-71.
188. Podstawka, E., Y. Ozaki, and L.M. Proniewicz, *Adsorption of S-S containing proteins on a colloidal silver surface studied by surface-enhanced Raman spectroscopy.* Appl Spectrosc, 2004. **58**(10): p. 1147-56.
189. Tipping, K.W., et al., *pH-induced molecular shedding drives the formation of amyloid fibril-derived oligomers.* Proc Natl Acad Sci U S A, 2015. **112**(18): p. 5691-6.
190. Grimsley, G.R., J.M. Scholtz, and C.N. Pace, *A summary of the measured pK values of the ionizable groups in folded proteins.* Protein Sci, 2009. **18**(1): p. 247-51.
191. Bar-On, Y.M., et al., *SARS-CoV-2 (COVID-19) by the numbers.* Elife, 2020. **9**.
192. Deinhardt-Emmer, S., et al., *SARS-CoV-2 causes severe epithelial inflammation and barrier dysfunction.* J Virol, 2021.
193. Zhu, N., et al., *A Novel Coronavirus from Patients with Pneumonia in China, 2019.* N Engl J Med, 2020. **382**(8): p. 727-733.
194. Coronaviridae Study Group of the International Committee on Taxonomy of, V., *The species Severe acute respiratory syndrome-related coronavirus: classifying 2019-nCoV and naming it SARS-CoV-2.* Nat Microbiol, 2020. **5**(4): p. 536-544.
195. Lamers, M.M. and B.L. Haagmans, *SARS-CoV-2 pathogenesis.* Nat Rev Microbiol, 2022. **20**(5): p. 270-284.
196. WHO. *WHO Coronavirus Disease (COVID-19) Dashboard.* 2022; Available from: https://covid19.who.int/?mapFilter=cases.
197. Wu, F., et al., *A new coronavirus associated with human respiratory disease in China.* Nature, 2020. **579**(7798): p. 265-269.
198. Hasoksuz, M., S. Kilic, and F. Sarac, *Coronaviruses and SARS-COV-2.* Turk J Med Sci, 2020. **50**(SI-1): p. 549-556.
199. Schoeman, D. and B.C. Fielding, *Coronavirus envelope protein: current knowledge.* Virol J, 2019. **16**(1): p. 69.
200. Chen, Y., Q. Liu, and D. Guo, *Emerging coronaviruses: Genome structure, replication, and pathogenesis.* J Med Virol, 2020. **92**(4): p. 418-423.
201. Bao, Q., et al., *Detection, prevention and treatment of COVID-19 and opportunities for nanobiotechnology.* View (Beijing), 2022: p. 20200181.
202. Neuman, B.W., et al., *A structural analysis of M protein in coronavirus assembly and morphology.* J Struct Biol, 2011. **174**(1): p. 11-22.
203. Hasoksuz, M., et al., *Molecular analysis of the S1 subunit of the spike glycoprotein of respiratory and enteric bovine coronavirus isolates.* Virus Research, 2002. **84**(1-2): p. 101-109.

204. Kumar, S., et al., *Morphology, Genome Organization, Replication, and Pathogenesis of Severe Acute Respiratory Syndrome Coronavirus 2 (SARS-CoV-2)*, in *Coronavirus Disease 2019 (COVID-19)*. 2020. p. 23-31.

205. Bosch, B.J., et al., *The coronavirus spike protein is a class I virus fusion protein: structural and functional characterization of the fusion core complex.* J Virol, 2003. **77**(16): p. 8801-11.

206. Kailasa, S.K., et al., *An overview of molecular biology and nanotechnology based analytical methods for the detection of SARS-CoV-2: promising biotools for the rapid diagnosis of COVID-19.* Analyst, 2021. **146**(5): p. 1489-1513.

207. Shen, M., et al., *Recent advances and perspectives of nucleic acid detection for coronavirus.* J Pharm Anal, 2020. **10**(2): p. 97-101.

208. Sokolenko, A.P. and E.N. Imyanitov, *Molecular Diagnostics in Clinical Oncology.* Front Mol Biosci, 2018. **5**: p. 76.

209. Leigh, K.E. and Y. Modis, *Imaging and visualizing SARS-CoV-2 in a new era for structural biology.* Interface Focus, 2021. **11**(6): p. 20210019.

210. Smyth, M.S. and J.H. Martin, *x ray crystallography.* Mol Pathol, 2000. **53**(1): p. 8-14.

211. Kneller, D.W., et al., *Room-temperature X-ray crystallography reveals the oxidation and reactivity of cysteine residues in SARS-CoV-2 3CL M(pro): insights into enzyme mechanism and drug design.* IUCrJ, 2020. **7**(Pt 6).

212. Kausche, G.A., E. Pfankuch, and H. Ruska, *Die Sichtbarmachung von pflanzlichem Virus im bermikroskop.* Die Naturwissenschaften, 1939. **27**(18): p. 292-299.

213. Goldsmith, C.S. and S.E. Miller, *Modern uses of electron microscopy for detection of viruses.* Clin Microbiol Rev, 2009. **22**(4): p. 552-63.

214. Zhang, Y., et al., *Electron microscopy: essentials for viral structure, morphogenesis and rapid diagnosis.* Sci China Life Sci, 2013. **56**(5): p. 421-30.

215. NIAID. *SARS-CoV-2, Images and B-roll related to the novel coronavirus (SARS-CoV-2, also known as 2019-nCoV) that causes COVID-19.* 2020; Available from: https://www.flickr.com/photos/niaid/49534865371/in/album-72157712914621487/.

216. Lyonnais, S., et al., *Atomic force microscopy analysis of native infectious and inactivated SARS-CoV-2 virions.* Sci Rep, 2021. **11**(1): p. 11885.

217. Kuznetsov, Y.G. and A. McPherson, *Atomic force microscopy in imaging of viruses and virus-infected cells.* Microbiol Mol Biol Rev, 2011. **75**(2): p. 268-85.

218. Eberhardt, K., et al., *Advantages and limitations of Raman spectroscopy for molecular diagnostics: an update.* Expert Rev Mol Diagn, 2015. **15**(6): p. 773-87.

219. Grasselli, J.G., M.K. Snavely, and B.J. Bulkin, *Applications of Raman spectroscopy.* Physics Reports, 1980. **65**(4): p. 231-344.

220. Putlyaeva, L.V. and K.A. Lukyanov, *Studying SARS-CoV-2 with Fluorescence Microscopy.* Int J Mol Sci, 2021. **22**(12).

221. Smee, D.F., et al., *Evaluation of cell viability dyes in antiviral assays with RNA viruses that exhibit different cytopathogenic properties.* J Virol Methods, 2017. **246**: p. 51-57.

222. Kumar, R., A. Kolloli, and S. Subbian, *Inactivation and Elimination of SARS-CoV-2 in Biosamples Using Simple Fixatives and Ultrafiltration.* Methods Protoc, 2021. **4**(1).

223. Schneider, C.A., W.S. Rasband, and K.W. Eliceiri, *NIH Image to ImageJ: 25 years of image analysis.* Nat Methods, 2012. **9**(7): p. 671-5.
224. Elveborg, S., V.M. Monteil, and A. Mirazimi, *Methods of Inactivation of Highly Pathogenic Viruses for Molecular, Serology or Vaccine Development Purposes.* Pathogens, 2022. **11**(2).
225. Moller, L., et al., *Evaluation of virus inactivation by formaldehyde to enhance biosafety of diagnostic electron microscopy.* Viruses, 2015. **7**(2): p. 666-79.
226. Haddock, E., et al., *Inactivation of SARS-CoV-2 Laboratory Specimens.* Am J Trop Med Hyg, 2021. **104**(6): p. 2195-2198.
227. Kim, S.O., et al., *Mechanical properties of paraformaldehyde-treated individual cells investigated by atomic force microscopy and scanning ion conductance microscopy.* Nano Converg, 2017. **4**(1): p. 5.
228. Yao, X., *Nanoscale Investigations of Biomaterials using Atomic Force Microscopy and Enhanced Raman Spectroscopy*, in *Chemisch-Geowissenschaftlichen Fakultät*. 2021, Friedrich-Schiller-Universität Jena: Jena, Thuringia Germany. p. 129.
229. Ma, B., et al., *UV Inactivation of SARS-CoV-2 across the UVC Spectrum: KrCl* Excimer, Mercury-Vapor, and Light-Emitting-Diode (LED) Sources.* Appl Environ Microbiol, 2021. **87**(22): p. e0153221.
230. Storm, N., et al., *Rapid and complete inactivation of SARS-CoV-2 by ultraviolet-C irradiation.* Sci Rep, 2020. **10**(1): p. 22421.
231. Biasin, M., et al., *UV-C irradiation is highly effective in inactivating SARS-CoV-2 replication.* Sci Rep, 2021. **11**(1): p. 6260.
232. Colville, K., et al., *Effects of poly(L-lysine) substrates on attached Escherichia coli bacteria.* Langmuir, 2010. **26**(4): p. 2639-44.
233. Xing, G.W., et al., *Capture of cervical exfoliative cells on a glass slide coated by 3-glycidyloxypropyl trimethoxysilane and poly-L-lysine.* J Pharm Anal, 2012. **2**(3): p. 174-179.
234. Adamczyk, Z., P. Batys, and J. Barbasz, *SARS-CoV-2 virion physicochemical characteristics pertinent to abiotic substrate attachment.* Curr Opin Colloid Interface Sci, 2021. **55**: p. 101466.
235. Turonova, B., et al., *In situ structural analysis of SARS-CoV-2 spike reveals flexibility mediated by three hinges.* Science, 2020. **370**(6513): p. 203-208.
236. Chen, H., et al., *Mechanisms of quenching of Alexa fluorophores by natural amino acids.* J Am Chem Soc, 2010. **132**(21): p. 7244-5.
237. Panchuk-Voloshina, N., et al., *Alexa dyes, a series of new fluorescent dyes that yield exceptionally bright, photostable conjugates.* J Histochem Cytochem, 1999. **47**(9): p. 1179-88.
238. Huang, Y., et al., *Structural and functional properties of SARS-CoV-2 spike protein: potential antivirus drug development for COVID-19.* Acta Pharmacol Sin, 2020. **41**(9): p. 1141-1149.
239. Yang, Y. and L. Du, *SARS-CoV-2 spike protein: a key target for eliciting persistent neutralizing antibodies.* Signal Transduct Target Ther, 2021. **6**(1): p. 95.
240. Xia, S., et al., *Fusion mechanism of 2019-nCoV and fusion inhibitors targeting HR1 domain in spike protein.* Cell Mol Immunol, 2020. **17**(7): p. 765-767.
241. Duan, L., et al., *The SARS-CoV-2 Spike Glycoprotein Biosynthesis, Structure, Function, and Antigenicity: Implications for the Design of Spike-Based Vaccine Immunogens.* Front Immunol, 2020. **11**: p. 576622.

242. Howard, M.W., et al., *Aromatic amino acids in the juxtamembrane domain of severe acute respiratory syndrome coronavirus spike glycoprotein are important for receptor-dependent virus entry and cell-cell fusion.* J Virol, 2008. **82**(6): p. 2883-94.

243. Singh, J., et al., *SARS-CoV2 infectivity is potentially modulated by host redox status.* Comput Struct Biotechnol J, 2020. **18**: p. 3705-3711.

244. Puthenveetil, R., et al., *S-acylation of SARS-CoV-2 spike protein: Mechanistic dissection, in vitro reconstitution and role in viral infectivity.* J Biol Chem, 2021. **297**(4): p. 101112.

245. Pezzotti, G., et al., *Raman Molecular Fingerprints of SARS-CoV-2 British Variant and the Concept of Raman Barcode* Adv Sci (Weinh), 2022. **9**(3): p. e2103287.

246. Podstawka, E., Y. Ozaki, and L.M. Proniewicz, *Part II: surface-enhanced Raman spectroscopy investigation of methionine containing heterodipeptides adsorbed on colloidal silver.* Appl Spectrosc, 2004. **58**(5): p. 581-90.

247. Bazylewski, P., R. Divigalpitiya, and G. Fanchini, *In situ Raman spectroscopy distinguishes between reversible and irreversible thiol modifications inl-cysteine.* RSC Advances, 2017. **7**(5): p. 2964-2970.

248. Madzharova, F., et al., *Surface-Enhanced Hyper-Raman Spectra of Adenine, Guanine, Cytosine, Thymine, and Uracil.* J Phys Chem C Nanomater Interfaces, 2016. **120**(28): p. 15415-15423.

Acknowledgments

First and foremost, I would like to praise Allah the Almighty, the Most Gracious, and the Most Merciful for His blessing given to me during my study and in completing this dissertation. May Allah’s blessing go to His final Prophet Muhammad (peace be upon him), his family, and his companions.

I began my doctoral studies just prior to the onset of the COVID-19 pandemic, a time that was fraught with numerous obstacles and uncertainties. Notwithstanding, I crossed the finish line! I would like to express my appreciation to the exceptional individuals who supported and guided me throughout this transformative journey, allowing me to earn my doctorate despite the numerous unforeseen obstacles that arose.

I would like to thank my doctoral supervisors, Professor Volker Deckert and Dr. Tanja Deckert-Gaudig, for their assistance. Their consistent guidance, support, and encouragement have been indispensable throughout the entire process. From the earliest stages of refining my research project to the submission of my dissertation, their unwavering presence and wealth of knowledge have been instrumental in fostering my professional growth. I greatly appreciated our weekly meetings, which not only served as crucial academic checkpoints but also provided me with an extensive amount of encouragement. I am profoundly grateful for the immeasurable contributions they have made to my development.

In addition to my supervisors, I am grateful to my outstanding lab mates, whose encouragement has been a constant source of motivation. I am proud to say that we have not only become lab partners but also good friends. Among the most memorable moments with them were when we went to the DokDok conference in 2019 and also when we had a group BBQ. We had a great time and laughed while eating delicious food, temporarily forgetting about our experiments. Moreover, I would also like to express my gratitude to everyone who has helped and supported me in any way.

Last but not least, I would like to express my deepest appreciation for my family's confidence in my abilities and unwavering support. Your prayer and encouragement played a crucial role in my accomplishments. To my late father (Solihin Darussalam), my mother (Dedeh Jamilah), my sister (Dewi Puspitasari), my brother (Yogi Umbarawan), and my nephew (Muhammad Salman Arvansyah): thank you for everything. This dissertation is dedicated to you.

Selbständigkeitserklärung

Ich erkläre, dass ich die vorliegende Arbeit selbständig und unter Verwendung der angegebenen Hilfsmittel, persönlichen Mitteilungen und Quellen angefertigt habe.

Jena, 30.08.2023 [redacted]

Ort, Datum Unterschrift der Verfasserin/des Verfassers